Surface Plasmon Resonance as a Technology for Miniaturized Sensor Systems

Dissertation

zur Erlangung des

Doktorgrades der Naturwissenschaften

(Dr. rer. nat.)

der Fakultät Chemie und Pharmazie

der Universität Regensburg

Deutschland

vorgelegt von

Peter Hausler

aus Ratzenhofen

im Jahr 2024

Die vorgelegte Dissertation entstand in der Zeit von Dezember 2013 bis Juli 2024 am Sensorik-ApplikationsZentrum (SappZ) der OTH Regensburg sowie am Institut für Analytische Chemie, Chemo- und Biosensorik der Universität Regensburg.

Die Arbeit wurde angeleitet von Prof. Dr. Rudolf Bierl und PD Dr. Thomas Hirsch.

Promotionsgesuch eingereicht am: 10.07.2024

Kolloquiumstermin:

Prüfungsausschuss

Vorsitzender:	Prof. Dr. Oliver Tepner
Erstgutachterin:	PD Dr. Thomas Hirsch
Zweitgutachter:	Prof. Dr. Rudolf Bierl
Drittprüfer:	Prof. Dr. Joachim Wegener

Acknowledgements

Ich möchte mich zuallererst herzlichst bei Prof. Dr. Rudolf Bierl und PD Dr. Thomas Hirsch bedanken, dass sie mir die Möglichkeit gegeben haben meine Promotion, zu diesem spannenden Thema anzufertigen. Vielen Dank für die stets verfügbare Betreuung, Unterstützung und Hilfe bei Problemstellungen aller Art.

Mein herzlicher Dank gilt Prof. Dr. Joachim Wegener für die Übernahme der Aufgabe des Drittprüfers und Prof. Dr. Oliver Tepner für das Ausüben der Funktion des Prüfungsvorsitzenden sowie Prof. Dr. Antje Bäumner für die Betreuung während der Arbeit.

Der Arbeitsgruppe um Dr. Thomas Hirsch an der Universität Regensburg danke ich herzlichst für die kontinuierliche erfolgreiche Zusammenarbeit über die ganzen Jahre.

Beim gesamten SPR-Team, allen voran bei Prof. Dr. Rudolf Bierl, bedanke ich mich für die unzähligen hilfreichen wissenschaftlichen und auch nicht-wissenschaftlichen Anregungen und Diskussionen.

Ich bedanke mich bei Thomas Vitzthumecker, Carina Roth, Thomas Mühlenfeld und Jakob Wolf, die im Rahmen ihrer Abschlussarbeiten Teilprojekte in den von mir geleiteten Forschungsprojekten übernommen haben. Ich bedanke mich bei Simon Jobst für die Arbeiten an der Messsoftware und bei Johannes Fischer für die Arbeiten an der Elektronik, sowie bei allen Kollegen die einen Teil zu dieser Arbeit beigetragen haben.

Vielen, vielen lieben Dank auch an die gesamten aktuellen und ehemaligen Kollegen aus dem Sensorik-ApplikationsZentrum und an alle Kollegen und Mitarbeiter im Reinraum für die ausgezeichnete Arbeitsatmosphäre.

Ein ganz besonderer Dank geht an meine Familie für die fortwährende Unterstützung und den Beistand über die gesamte Zeit. Ich danke meinem Cousin Dr. Josef Kiermaier, der mich durch sein Studium und seine Promotion dazu inspiriert hat selbst zu studieren. Ich danke meinen Eltern Peter und Hannelore Hausler dafür, dass sie mich bei allen meine Entscheidungen stets unterstützt und gefördert haben und es mir so ermöglicht haben den Weg als Wissenschaftler zu gehen.

Inhalt

Declaration of Collaborations

Most of the experimental and theoretical work presented in this thesis was carried out solely by the author. However, some of the results were obtained together with other researchers. In accordance with § 8 Abs. 1 Satz 2 Punkt 7 of the „Ordnung zum Erwerb des akademischen Grades eines Doktors der Naturwissenschaften (Dr. rer. nat.) an der Universität Regensburg vom 18. Juni 2009“, this section gives information about these collaborations.

Chapter 3: Surface Plasmon Resonance Imaging for Detection of Drug Metabolites in Water

Surface plasmon resonance imaging for detection of drug metabolites in water. In Optical Sensors 2019 (Vol. 11028, pp. 148-158). SPIE (2019)

Conceptualization: Peter Hausler (P.H.), Lukas Wunderlich (L.W.), Thomas Hirsch (T.H.), R.B.; methodology: L.W., P.H., Christina Pfab, Simon Heckscher, T.H.; validation: L.W., P.H., Johannes Fischer (J.F.); investigation: P.H., L.W.; data curation: L.W., J.F., P.H.; writing—original draft preparation: P.H., L.W., T.H.; writing—review and editing: L.W., P.H., R.B., T.H.; supervision: R.B., T.H.; All authors have read and agreed to the published version of the manuscript.

Chapter 4: Homogeneous Light Source for Surface Plasmon Resonance Imaging

Homogeneous Light Source for Surface Plasmon Resonance Imaging. In PHOTOPTICS (pp. 163-167). SCITEPRESS (2020)

Conceptualization: P.H., R.B.; methodology: P.H., Simon Jobst (S.J.); validation: P.H., S.J., J.F.; investigation: P.H., C.R.; data curation: S.J., P.H.; writing—original draft preparation: P.H., R.B.; writing—review and editing: P.H., S.J., R.B.; supervision: R.B.; All authors have read and agreed to the published version of the manuscript.

Chapter 5: Nanoparticle Determination in Water by LED Excited Surface Plasmon Resonance Imaging

Nanoparticle Determination in Water by LED-Excited Surface Plasmon Resonance Imaging. Chemosensors 9.7: 175. MDPI (2021)

This study was conceived and designed by Thomas Hirsch, Rudolf Bierl, Lukas Wunderlich and the author and supervised by Thomas Hirsch and Rudolf Bierl. The experimental work was carried out by Lukas Wunderlich (point based and imaging SPR) and the author (imaging SPR). The imaging setup was developed and operated by the author. Nanoparticle synthesis and characterization was done by Susanne Märkl. Data curation was performed by Lukas Wunderlich and the author. The original draft was created by Lukas Wunderlich and the author, edited by Lukas Wunderlich, Thomas Hirsch and the author. Thomas Hirsch is the corresponding author.

Chapter 6: Drift correction of SPR signals by improved sensor surfaces

The AFM measurements were carried out by Dr. Hubert Maier from the Institute of Experimental and Applied Physics at the University of Regensburg. Jakob Wolf has programmed an extension to the SPR software that automatically stabilizes measurement regions with references.

Chapter 7: The pathway to a miniaturized SPR sensor

The Python script to improve the placement and distribution of each ROI was written by Simon Jobst. Simon Jobst has rendered Figure 7.6. The comparison of the developed SPR instruments with a commercial device in a bioassay format was supported by the help of Dr. Thomas Hirsch in providing the protein solutions.

Preface and Motivation

In surface plasmon resonance (SPR) sensing [1], the use of only one to a few measurement spots is a common limitation in setups. In these straightforward measurement designs, a laser beam is coupled via a prism to a thin gold film, which is subsequently modified by a receptor layer. The reflectance of the laser beam is then recorded in dependence on the angle of incidence (θ_i) or at a fixed θ_i over time. The sensor surface is brought into contact with an analyte solution via a flow cell. This method has led to the establishment of SPR devices as a standard technique for the label-free study of the binding kinetics of biological substances (Figure 1). For scientists, these devices are renowned for their exceptional sensitivity and ease of use [2]. Measurements can be conducted over a period ranging from minutes to hours, typically under laboratory conditions. This makes SPR sensing a valuable tool in the scientific community.

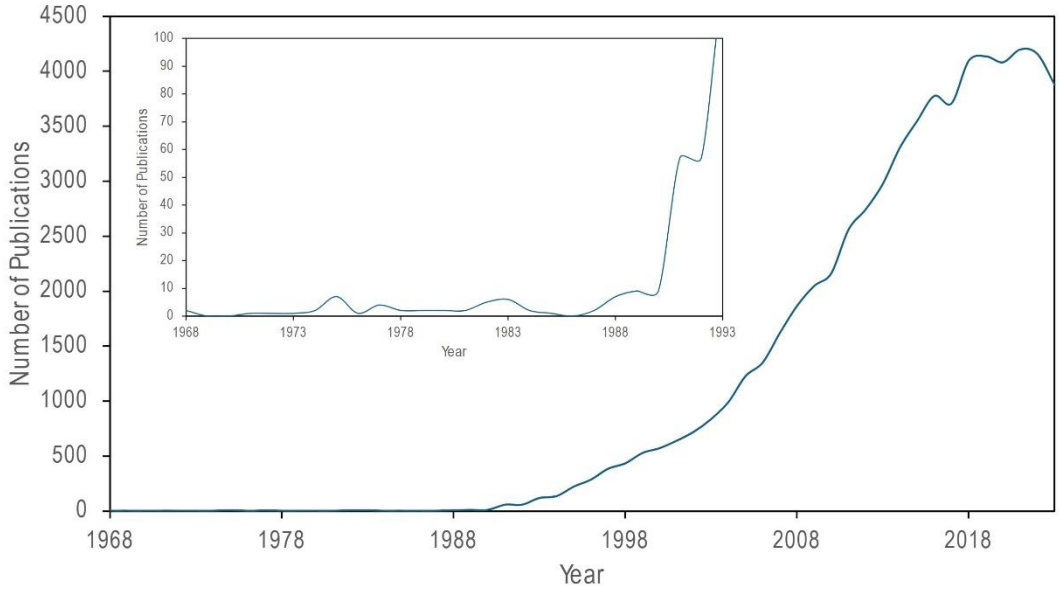

Figure 1: Number of publications per year containing "Surface Plasmon Resonance" at the topic. Data derived from https://www.webofscience.com , The data was retrieved on 15/05/2024.

Despite the advantages of this type of SPR devices, numerous drawbacks must be considered when attempting to apply this technology to a sensor capable of monitoring several analytes in a complex matrix over an extended period. Environmental sensing would greatly benefit from the high sensitivity and label-free nature of SPR sensing [3]. Illuminating the receptor at only one spot may not be able to compensate for fluctuations in parameters such as temperature or laser stability, furthermore it will become difficult to distinguish analyte binding from unspecific bindings or even degradation of the receptor layer. Multi-channel SPR turned out to overcome these challenges in some extend, but still suffer from designing complex experiments with lots of control measurements to get reliable and precise results. Additionally, the instrumental effort gets significantly increased and those devices are not suitable for in filed online measurements. A new approach to tackle this challenge is to use SPR imaging technology for compact sensor devices.

With SPR imaging, the sensor area can be divided into numerous regions of interest (ROI) of different size and shape. This makes it possible to obtain individual SPR characteristics from each region on the sensor. The size and number of regions is usually only limited by the resolution of the optical system. It is therefore possible to observe numerous, very different structures in parallel. A laser beam expanded onto the imaged area creates numerous interference patterns, which significantly reduce the resolution. Coupling a gold-coated glass slide by an index matching fluid to

the prism introduce even more problems, as inhomogeneities affect small measurement regions a lot. Furthermore, such liquid films bear the danger to disintegrate or to dry upon heating effects by the laser illumination over long measurement times as envisioned in environmental monitoring. The intensity profile of an expanded Gaussian beam of a laser is characterized by steep slopes rising across small measurement regions. Any slightest movements within the system, which must be anticipated in portable devices, will lead to huge changes in the measurement signal.

To integrate SPR in miniaturized sensing devices, research is needed to develop a compact and homogeneous light source and to improve the insensitivity to environmental influences. For miniaturization, one further needs to find a compromise on the detector side. So far, the camera, its lens, and the working distance of the lens are often larger than the desired size of the whole SPR sensor.

Therefore, this work is devoted to find practicable solutions for a miniaturized SPR sensor by thoroughly investigations of the impact of each component in a lab-based set-up for intensity-based readout with the final goal to integrate the system in a portable device.

References

[1] Homola J. Surface plasmon resonance sensors for detection of chemical and biological species. Chemical reviews. 2008 Feb 13;108(2):462-93.

[2] Rich RL, Myszka DG. Advances in surface plasmon resonance biosensor analysis. Current opinion in biotechnology. 2000 Feb 1;11(1):54-61.

[3] Masson JF. Portable and field-deployed surface plasmon resonance and plasmonic sensors. Analyst. 2020;145(11):3776-800.

1. Introduction to Surface Plasmon Resonance

1.1 Theory

Surface Plasmon Resonance (SPR) is a sophisticated and versatile technique used in analytical chemistry for the detection and quantification of a wide range of chemical and biological analytes [1-3]. At its core, SPR is a phenomenon that occurs when polarized light strikes a metal-dielectric interface (typically gold or silver) under total internal reflection conditions, leading to the excitation of electron charge density waves known as surface plasmons. To provide a framework for understanding and describing this complex optical phenomenon a combination of electromagnetism and quantum mechanics is needed. At a basic level, it can be described using classical electromagnetic theory. The key equations and principles include Maxwell's Equations (Equations 1 – 4) for understanding electromagnetic waves and their interaction with materials.

$$\nabla \cdot E = \frac{\rho}{\epsilon_0} \tag{1}$$

$$\nabla \cdot B = 0 \tag{2}$$

$$\nabla \times E = -\frac{\partial B}{\partial t} \tag{3}$$

$$\nabla \times B = \mu_0 \cdot J + \mu_0 \cdot \epsilon_0 \cdot \frac{\partial E}{\partial t} \tag{4}$$

Where E is the electric field, B the magnetic field, ρ the charge density, J the current density, ε_0 the permittivity in free space, and the time. Analysis of Maxwell's equations with appropriate boundary conditions suggests that at the interface of a semi-infinite metal with a complex permittivity and a semi-infinite dielectric layer only a single guided mode of electromagnetic field can be supported. This field is called surface plasmon [1].

Fresnel equations (Equations 5 & 6) describe the reflection and transmission of light at an interface between two media. They are critical in determining the conditions under which total internal reflection occurs and how polarized light interacts with the metal-dielectric interface. The Fresnel equations for reflection coefficients r_p and r_s for *p*-polarized and *s*-polarized light, respectively, are:

$$r_p = \frac{n_2 \cdot \cos(\theta_i) - n_1 \cdot \cos(\theta_t)}{n_2 \cdot \cos(\theta_i) + n_1 \cdot \cos(\theta_t)} \tag{5}$$

$$r_s = \frac{n_1 \cdot \cos(\theta_i) - n_2 \cdot \cos(\theta_t)}{n_1 \cdot \cos(\theta_i) + n_2 \cdot \cos(\theta_t)} \tag{6}$$

where n_1 and n_2 are the refractive indices of the two media, θ_i is the angle of incidence, and θ_t is the angle of transmission [2].

The condition for the excitation of surface plasmons at the interface can be described by a dispersion relation, which links the frequency of the plasmons to their wave vector. This relation is influenced by the properties of the metal and the dielectric. For a simple metal-dielectric interface, the dispersion relation is:

$$\beta = \frac{\omega}{c} \cdot \sqrt{\frac{\epsilon_m \cdot \epsilon_d}{\epsilon_m + \epsilon_d}} \tag{7}$$

where β is the propagation constant of the surface plasmon wave, ω is the angular frequency of the light, c is the speed of light in vacuum, ϵ_m is the dielectric function of the metal, and ϵ_d is the dielectric constant of the dielectric material [4,5].

Total internal reflection occurs when light propagating in a medium with a higher refractive index strikes an interface with a medium of lower refractive index at an angle greater than the critical angle. The critical angle θ_c is given by:

$$\theta_c = \arcsin\left(\frac{n_2}{n_1}\right) \tag{8}$$

where n_1 is the refractive index of the denser medium and n_2 is the refractive index of the less dense medium.

$$\epsilon = n^2 \tag{9}$$

Since this correlation applies to the relationship between refractive index and dielectric constant, changes in refractive index will strongly affect the coupling described. This enables to use this principle in chemical sensing as the refractive index at the interface will change upon binding events of molecules which alter the chemical composition of the interface layer [3].

The application of SPR as a transducer in chemical sensors offers several significant benefits [6]. Firstly, SPR allows for real-time, label-free detection, which often is a substantial advantage over methods that require fluorescent, radioactive, or enzymatic labels. This capability not only simplifies the assay preparation but also avoids potential interference from the labels themselves. Secondly, SPR is highly sensitive and capable of detecting low concentrations of analytes, making it suitable for applications where trace detection is essential [7]. Moreover, the technology's inherent specificity, arising from the selective binding of target molecules to the sensor surface, enables the detection of specific analytes in complex mixtures [8-10].

Miniaturization of SPR technology is a key area of research, particularly relevant to the development of portable, cost-effective, and efficient analytical tools [11]. Miniaturized SPR sensors offer the advantages of reduced sample and reagent volumes, faster analysis times, and the potential for parallelized detection [12-14]. The latter is particularly important because it enables the simultaneous analysis of multiple analytes, increasing the throughput and efficiency of the technique [15]. Parallelization in SPR can be achieved through the integration of imaging techniques. By spatially resolving the SPR signal, it is possible to monitor multiple sensing spots simultaneously. Each spot can potentially be functionalized with different capture agents for different targets. This approach not only increases the sensor's capacity but also facilitates comparative and reference measurements, enhancing the reliability of the results [16-22].

1.2 Historical Background

The development of SPR for label-free detection in analytical chemistry has undergone several key steps [9], marking its evolution from a fundamental phenomenon to a powerful analytical tool.

In the late 1950 the history of SPR based sensor started with the development of the concept and its first theoretical description. Early work focused on the fundamental understanding of plasmons, the collective oscillations of free electrons at the surface of conductive materials like metals, particularly under the influence of light [23-28].

During the 1960s, two significant milestones in the field of SPR technology were achieved by A. Otto and in the same year by E. Kretschmann and H. Raether [29-31]. In 1968, Kretschmann and Raether developed what is now known as the Kretschmann configuration for exciting surface plasmons. This configuration, which involves a thin metal film sandwiched between a prism and a dielectric medium, was a crucial advancement in the ability to observe and study surface plasmons. Shortly before, in 1968, A. Otto introduced an alternative method, known as the Otto configuration, which differs by having a gap of air or low refractive index material between the prism and the metal layer. These breakthroughs laid the foundational understanding and methodologies for the modern development of SPR technology, significantly contributing to its advancement as a sensitive tool for measuring molecular interactions in real-time.

Initial experimental observations started in the 1970s. Researchers demonstrated how light could excite surface plasmons at a metal-dielectric interface, leading to a resonance condition that was highly sensitive to changes in the refractive index at the interface [32-34].

The period from 1980s to 1990s saw the development of the first SPR sensors. Scientists started to exploit the sensitivity of SPR to changes in the refractive index for detecting molecular interactions. The SPR technique was first mentioned as a biosensing detection method in 1983 [35]. Key advancements included the integration of SPR with optical fibers and prism-based setups, which laid the foundation for modern SPR sensors [4,5,36-43]. The year 1988 marked a significant advancement in the field of surface plasmon resonance technology with the inaugural demonstration of the principle of SPR imaging by Rothenhäusler and Knoll [44].

With the improvements in computational power and data analysis techniques, advancement in sensitivity and specificity of SPR dominated the next decade (1990s - 2000s). The interpretation of SPR data became more sophisticated, allowing for more accurate and detailed analysis of molecular interactions [45-51]. In 1990 the first commercial SPR instrument for biosensing was launched by the Swedish company Biacore [52]. Ten years after SPR imaging greatly expanded the possibilities in research, another, fundamentally different plasmonic technology was used as a biosensor for the first time. Englebienne was the first to publish a biosensor with plasmonic nanostructures as a transducer [53].

From the 2000s on integration with microfluidics and miniaturization marked a significant step in its development. This combination allowed for the handling of smaller sample volumes, reduced reagent consumption, and the possibility of high-throughput screening. Miniaturization efforts aimed to make SPR devices more portable and accessible for various applications [54-59].

From the 2010s to the present the focus was shifted to label-free detection and parallelization, allowing for the direct observation of biomolecular interactions without the need for fluorescent or radioactive labels. Concurrently, there is a trend towards high-throughput capabilities, enabling the simultaneous detection of multiple analytes, which significantly increased the applicability of SPR in various fields of analytical chemistry. The latest advancements involve the integration of SPR with various imaging techniques. This development enables spatially resolved detection with richer data sets. Ongoing efforts continue in further miniaturizing SPR sensors, improving their sensitivity and stability, and making them more user-friendly and suitable for on-field applications. Each of these steps has been crucial in transforming SPR into a highly sensitive, label-free detection method in analytical chemistry, suitable for a wide range of applications from drug discovery to environmental monitoring [20,60-76].

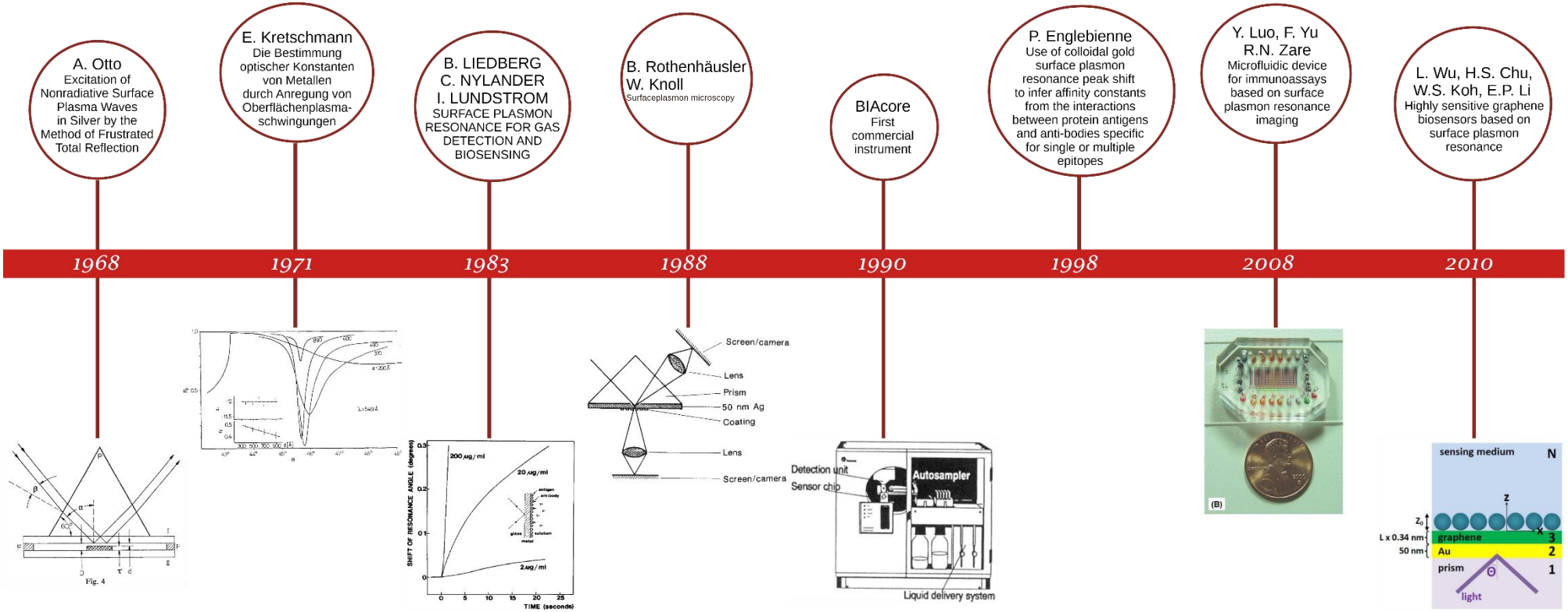

Figure 1.1: Important milestones in the development of SPR towards a label-free method for applications in analytical chemistry.

1.3 Surface Plasmon Resonance as a High-Resolution Measurement Transducer

Surface plasmons are collective oscillations of electrons that are excited at the interface between a metal and a dielectric medium, such as a gas or a liquid. These oscillations are excited by incident light when the frequency of the light matches the natural frequency of the surface plasmons [77]. This resonance condition is highly sensitive to the properties of the metal surface and the adjacent dielectric medium. At resonance, a significant amount of the incident light's energy is transferred over to surface plasmons, reducing the intensity of the reflected light at a given angle and wavelength. This decrease in reflectance is known as the SPR dip and is used as an indicator of resonance. The position of the SPR dip is very sensitive to changes in the refractive index of the material near the metal surface. This sensitivity enables SPR to detect small changes in the surface environment, such as the binding of biomolecules to the surface [9].

A prism is a geometric solid that is displaced by parallel displacement of a plane polygon along a straight line perpendicular to the base surface in space. This is a special polyhedron with the following properties: the polygon forms the base surface; the opposite surface forms the top surface; the remaining faces form the lateral face. The base and top surfaces connecting the side edges are parallel to each other, and the side edges are of equal length. The base and top surfaces are congruent and parallel. In the aforementioned application, a triangular prism with an isosceles base is employed. The lateral facets, resulting from the catheti, serve as couplings for the light, which is then reflected by the lateral facet resulting from the hypotenuse. To facilitate the assembly process, the side edge between the catheti was removed. In essence, the polyhedron is extruded from an isosceles and symmetrical trapezoid. In the following, the term "prism" is employed to designate the body described in this text.

An SPR curve (Figure 1.2) can be obtained in two ways. In the first method, the angle of incidence is varied while keeping the wavelength constant (a), and the intensity of the reflected light is recorded. The second method is to vary the wavelength while keeping the angle of incidence constant (b) and record the intensity of the reflected light.

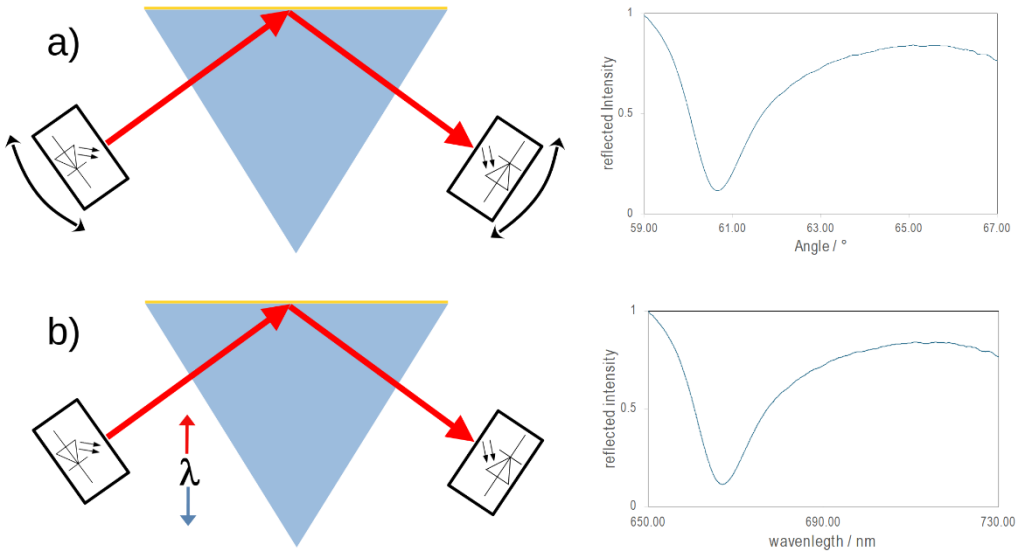

Figure 1.2: A glass prism coated with a thin metal layer, a) Monochromatic, polarized, and collimated light is reflected under total internal reflection at the coated surface of the prism. The intensity of the reflected light is recorded with a photodiode, while the angle of incidence is varied. The intensity of the reflected light is showing a dip at the angle where the resonance condition is matched. b) Similar setup as before, instead of the angle of incidence, the wavelength of the light is varied.

A change in the refractive index of the medium to be analyzed above the metal layer leads to a shift in the position of the SPR curve. This applies to both the wavelength scan and the angle scan (Figure 1.3).

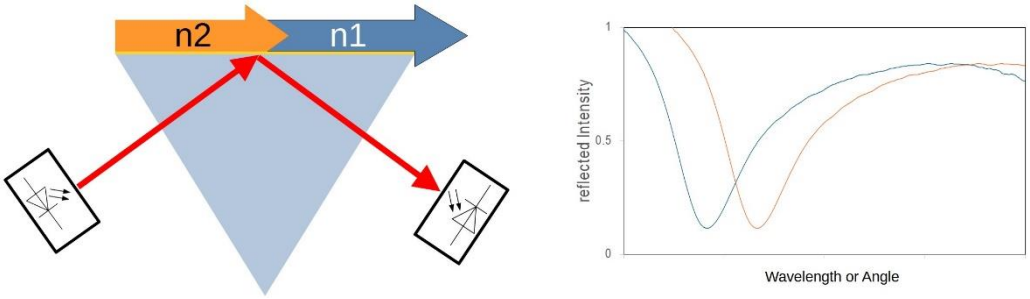

Figure 1.3: A change in the refractive index of the medium above the prism (n1 -> n2) will result in a shift of the SPR curve.

If the angle or wavelength is scanned permanently, it is possible to track a shift in the minimum of the SPR curve when the refractive index changes (Figure 1.4 a). A permanent scanning can be time-consuming and instrumentally demanding, but there is a different method that has become established in practice that is much more efficient. In analytical chemistry the intensity scan method has established as a simple straight-forward approach to monitoring biomolecular interactions and changes in the refractive index at the metal-dielectric interface [78]. Unlike the angular and wavelength scan methods, the intensity method maintains a constant angle of incidence and a constant wavelength of the incident light. It records changes in the intensity of the reflected light over time (Figure 1.4 b). Although not required, it is nevertheless advantageous to be able to ascertain the shape of the SPR curve in order to identify the optimal measurement angle [79].

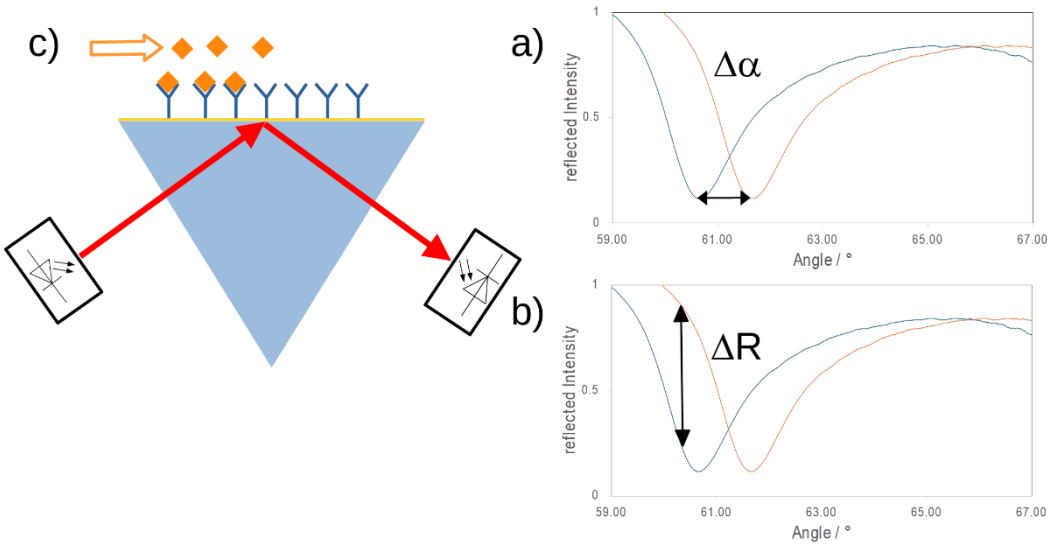

Figure 1.4: a) The shift of the SPR curve can be monitored by monitoring the position of the minimum of the SPR curve. b) The shift of the SPR curve can also be monitored by monitoring the intensity of the reflected light at a fixed angle. c) If one wishes to monitor only a certain component of the analyzed medium, the surface of the sensor can be equipped with receptors so that only the target analyte can dock to the sensor surface.

As the refractive index of the medium above the gold layer changes, the SPR curve shifts. However, since the angle of observation remains constant, the intensity of the reflected light changes. The steeper the curve, the greater the change in intensity per change in angle.

A sensor of the type depicted in Figure 1.3 would indicate a change in the refractive index. However, the refractive index itself is only of interest in the rarest of cases, as in most cases the aim is to infer a change in the refractive index from a change in the composition of the medium being analyzed. For example, winegrowers use the refractive index to determine the sugar content of grape juice. In contrast, in analytical chemistry, the task is considerably more complex in the majority of cases. The objective is typically to identify the usually very small change in the concentration of a very specific molecule. In order to facilitate this functionality, the sensor is equipped with receptors (Figure 1.4 c). These bind the target analyte for a specific period of time, simultaneously preventing the accumulation of other substances on the surface. As a result, the SPR sensor becomes selective for a specific substance.

It needs to be noted, that it is assumed that only a change in the refractive index occurs at the dielectric and that all other parameters remain constant, i.e. that in particular the shape of the curve of the angle-dependent intensities remains unchanged and that the curve only changes in the position of the resonance angle while maintaining its shape. This condition is met in most analytically relevant solutions. Nevertheless, especially for unknown real samples, one should always measure the intensity values as a function of the angle at the beginning and end of the measurements of binding events to ensure that these conditions are met.

Another approximation that is often used in this method is the fact that the curve of the angle-dependent intensity values to the left of the SPR minimum is assumed to be linear within a certain range and, by shifting the SPR curve to different angles, a linear relationship can be established between the concentration of the bound analyte molecules and the change in intensities achieved.

This simplifies the calibration, and this approximation is usually very good, especially for very small changes in concentration.

Other methods of using SPR for measurements are also available. Some examples are wavelength interrogation SPR spectroscopy, polarization contrast-based SPR or SPR microscopy. However, these methods usually require more and more complex instrumentation [80-82].

Semiconductor technology represents a pivotal factor in the quest for miniaturization, facilitating the miniaturization of a multitude of sensors. In the context of miniaturization and robustness, sensors without moving parts are advantageous because they wear less and are less susceptible to vibrations. Consequently, when contemplating the miniaturization of surface plasmon resonance (SPR) technology, it is advantageous to employ an SPR technique that inherently lacks moving parts. This approach not only facilitates miniaturization but also contributes to the robustness of the sensor.

1.4 2D Surface Plasmon Resonance Sensor - SPR-imaging (SPRi)

Up to now most SPR devices illuminate a metal surface at a single or at multiple spots with a laser diode. The reflected light is directed to a photodiode to collect the signal. Often two beams are used, and the gold surface is divided in two channels, one for each laser spot on the metal surface. Such a configuration enables to compensate in a first approximation temperature fluctuations or unspecific binding. Some devices use even more beams and therefore more channels to enable the simultaneous detection of several analytes in parallel when the sensor surface is functionalized with different receptors.

An alternative approach to spatially resolved SPR is a technique known as SPR-imaging. In this approach, a single light beam is employed to uniformly illuminate the entire gold surface (Figure 1.5). The reflected light is then projected onto the surface of a camera. Each pixel in the camera image is associated with an area on the gold surface. By analyzing the intensity changes in the reflected light at each pixel, it is possible to map out variations in surface interactions. In most cases, several pixels are aggregated to form a region of interest (ROI). The typical size of an ROI is between a few tens of micrometers and a few hundred micrometers.

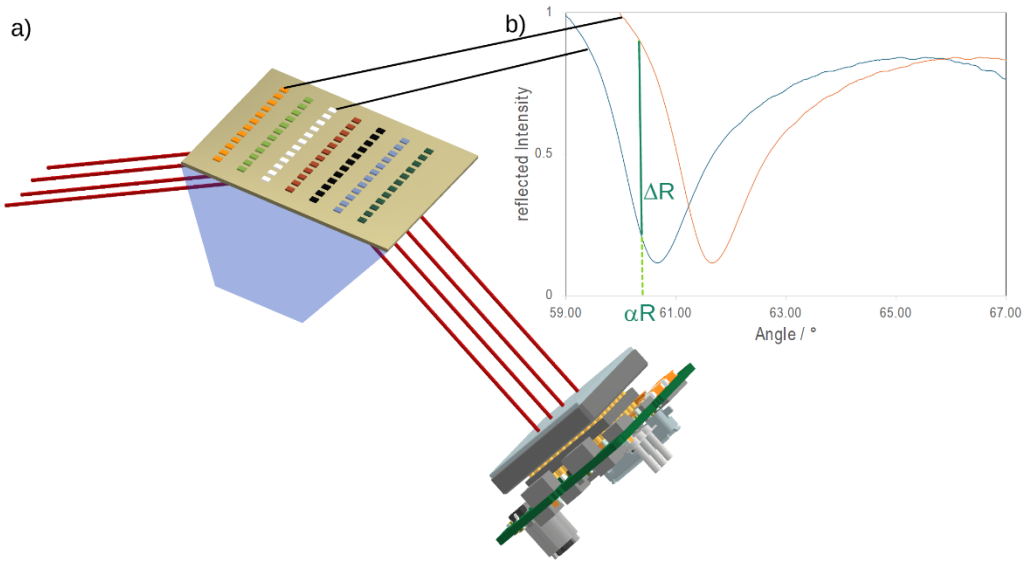

Figure 1.5: If the SPR prism is illuminated over a large area instead of only at a specific point, it is possible to utilize the entire surface of the prism as a sensor. This is achieved by conducting the readout with a camera instead of a photodiode. The lateral resolution achieved in this manner permits the placement of numerous receptors in parallel.

A spatially resolved image offers considerably more room for improvement. In contrast to a spot measurement, an imaging method allows for a more comprehensive assessment of the homogeneity of an applied layer. Furthermore, the evaluation via a two-dimensional image allows for the selection of a free-form ROI shape. This implies that the ROI does not necessarily have to be round or square but can take on any shape. This considerably enhances the utilization of the receptor areas. Additionally, defective areas can be excluded.

If one considers that the usable sensor area is on the order of a square centimeter and that the size of a region of interest (ROI) ranges from a few hundred square micrometers to square millimeters, then it becomes clear that a significant number of ROIs can be placed on one sensor. Such an extensive parallelism in ROIs is difficult to achieve with multibeam SPR. The extensive range of potential ROIs allows the user to place additional structures on the sensor, in addition to the receptors necessary for a potential binding analysis.

1.5 References

[1] Homola J. Present and future of surface plasmon resonance biosensors. Analytical and bioanalytical chemistry. 2003 Oct;377:528-39.

[2] Knoll W. Interfaces and thin films as seen by bound electromagnetic waves. Annual review of physical chemistry. 1998 Oct;49(1):569-638.

[3] Wijaya E, Lenaerts C, Maricot S, Hastanin J, Habraken S, Vilcot JP, Boukherroub R, Szunerits S. Surface plasmon resonance-based biosensors: From the development of different SPR structures to novel surface functionalization strategies. Current Opinion in Solid State and Materials Science. 2011 Oct 1;15(5):208-24.

[4] Nylander C, Liedberg B, Lind T. Gas detection by means of surface plasmon resonance. Sensors and Actuators. 1982 Jan 1;3:79-88.

[5] Liedberg B, Nylander C, Lunström I. Surface plasmon resonance for gas detection and biosensing. Sensors and actuators. 1983 Jan 1;4:299-304.

[6] Uniyal A, Srivastava G, Pal A, Taya S, Muduli A. Recent advances in optical biosensors for sensing applications: a review. Plasmonics. 2023 Apr;18(2):735-50.

[7] Mitchell J. Small molecule immunosensing using surface plasmon resonance. Sensors. 2010 Aug 4;10(8):7323-46.

[8] Sensors SP. Surface Plasmon Resonance Based Sensors. Sens. and Biosen. 2006;4.

[9] Schasfoort RB, editor. Handbook of surface plasmon resonance. Royal Society of Chemistry; 2017 May 30.

[10] Oliveira LC, Lima AM, Thirstrup C, Neff HF. Surface plasmon resonance sensors: a materials guide to design, characterization, optimization, and usage. Springer; 2019 Jun 13.

[11] Hausler P, Roth C, Vitzthumecker T, Bierl R. Miniaturized Surface Plasmon Resonance Based Sensor Systems—Opportunities and Challenges. Optics, Photonics and Laser Technology 2018. 2019:169-95.

[12] Wang DS, Fan SK. Microfluidic surface plasmon resonance sensors: From principles to point-of-care applications. Sensors. 2016 Jul 27;16(8):1175.

[13] De Leebeeck A, Kumar LS, De Lange V, Sinton D, Gordon R, Brolo AG. On-chip surface-based detection with nanohole arrays. Analytical Chemistry. 2007 Jun 1;79(11):4094-100.

[14] Wilson DM, Hoyt S, Janata J, Booksh K, Obando L. Chemical sensors for portable, handheld field instruments. IEEE Sensors Journal. 2001 Dec;1(4):256-74.

[15] Liu Y, Zhang X. Microfluidics-based plasmonic biosensing system based on patterned plasmonic nanostructure arrays. Micromachines. 2021 Jul 14;12(7):826.

[16] Piliarik M, Párová L, Homola J. High-throughput SPR sensor for food safety. Biosensors and Bioelectronics. 2009 Jan 1;24(5):1399-404.

[17] Piliarik M, Bocková M, Homola J. Surface plasmon resonance biosensor for parallelized detection of protein biomarkers in diluted blood plasma. Biosensors and Bioelectronics. 2010 Dec 15;26(4):1656-61.

[18] Neumann T, Junker HD, Schmidt K, Sekul R. SPR-based fragment screening: advantages and applications. Current topics in medicinal chemistry. 2007 Aug 1;7(16):1630-42.

[19] Damborský P, Švitel J, Katrlík J. Optical biosensors. Essays in biochemistry. 2016 Jun 30;60(1):91-100.

[20] Couture M, Zhao SS, Masson JF. Modern surface plasmon resonance for bioanalytics and biophysics. Physical Chemistry Chemical Physics. 2013;15(27):11190-216.

[21] Nguyen HH, Park J, Kang S, Kim M. Surface plasmon resonance: a versatile technique for biosensor applications. Sensors. 2015 May 5;15(5):10481-510.

[22] Nelson BP, Grimsrud TE, Liles MR, Goodman RM, Corn RM. Surface plasmon resonance imaging measurements of DNA and RNA hybridization adsorption onto DNA microarrays. Analytical chemistry. 2001 Jan 1;73(1):1-7.

[23] Bohm D, Pines D. A collective description of electron interactions. I. Magnetic interactions. Physical Review. 1951 Jun 1;82(5):625.

[24] Pines D, Bohm D. A collective description of electron interactions: II. Collective vs individual particle aspects of the interactions. Physical Review. 1952 Jan 15;85(2):338.

[25] Palmer CH. Parallel diffraction grating anomalies. JOSA. 1952 Apr 1;42(4):269-76.

[26] Bohm D, Pines D. A collective description of electron interactions: III. Coulomb interactions in a degenerate electron gas. Physical Review. 1953 Nov 1;92(3):609.

[27] Palmer CH. Diffraction grating anomalies. II. Coarse gratings. JOSA. 1956 Jan 1;46(1):50-3.

[28] Ritchie RH. Plasma losses by fast electrons in thin films. Physical review. 1957 Jun 1;106(5):874.

[29] Hessel A, Oliner AA. A new theory of Wood's anomalies on optical gratings. Applied optics. 1965 Oct 1;4(10):1275-97.

[30] Otto A. Excitation of nonradiative surface plasma waves in silver by the method of frustrated total reflection. Zeitschrift für Physik A Hadrons and nuclei. 1968 Aug;216(4):398-410.

[31] Kretschmann E, Raether H. Radiative decay of non radiative surface plasmons excited by light. Zeitschrift für Naturforschung A. 1968 Dec 1;23(12):2135-6.

[32] Kretschmann E. Die bestimmung optischer konstanten von metallen durch anregung von oberflächenplasmaschwingungen. Zeitschrift fur physik. 1971 Aug;241(4):313-24.

[33] Burstein E, Chen WP, Chen YJ, Hartstein A. Surface polaritons—propagating electromagnetic modes at interfaces. Journal of Vacuum Science and Technology. 1974 Nov 1;11(6):1004-19.

[34] Pockrand I, Swalen JD, Gordon Ii JG, Philpott MR. Surface plasmon spectroscopy of organic monolayer assemblies. Surface Science. 1978 May 2;74(1):237-44.

[35] Wijaya E, Lenaerts C, Maricot S, Hastanin J, Habraken S, Vilcot JP, Boukherroub R, Szunerits S. Surface plasmon resonance-based biosensors: From the development of different SPR structures to novel surface functionalization strategies. Current Opinion in Solid State and Materials Science. 2011 Oct 1;15(5):208-24.

[36] Nylander C, Liedberg B, Lind T. Gas detection by means of surface plasmon resonance. Sensors and Actuators. 1982 Jan 1;3:79-88.

[37] Liedberg B, Nylander C, Lunström I. Surface plasmon resonance for gas detection and biosensing. Sensors and actuators. 1983 Jan 1;4:299-304.

[38] Flanagan MT, Pantell RH. Surface plasmon resonance and immunosensors. Electronics Letters. 1984;23(20):968-70.

[39] Cullen DC, Brown RG, Lowe CR. Detection of immuno-complex formation via surface plasmon resonance on gold-coated diffraction gratings. Biosensors. 1987 Jan 1;3(4):211-25.

[40] Zhang LM, Uttamchandani D. Optical chemical sensing employing surface plasmon resonance. Electronics Letters. 1988 Nov 10;24(23):1469-70.

[41] Matsubara K, Kawata S, Minami S. Optical chemical sensor based on surface plasmon measurement. Applied optics. 1988 Mar 15;27(6):1160-3.

[42] Markatos S, Zervas MN, Giles IP. Optical fibre surface plasmon wave devices. Electronics letters. 1988 Mar 3;24(5):287-8.

[43] Villuendas F, Pelayo J. Optical fibre device for chemical seming based on surface plasmon excitridon. Sensors and Actuators A: Physical. 1990 Apr 1;23(1-3):1142-5.

[44] Rothenhäusler B, Knoll W. Surface–plasmon microscopy. Nature. 1988 Apr 14;332(6165):615-7.

[45] Löfås S, Malmqvist M, Rönnberg I, Stenberg E, Liedberg B, Lundström I. Bioanalysis with surface plasmon resonance. Sensors and Actuators B: Chemical. 1991 Aug 1;5(1-4):79-84.

[46] Myszka DG. Kinetic analysis of macromolecular interactions using surface plasmon resonance biosensors. Current opinion in biotechnology. 1997 Feb 1;8(1):50-7.

[47] Jung LS, Campbell CT, Chinowsky TM, Mar MN, Yee SS. Quantitative interpretation of the response of surface plasmon resonance sensors to adsorbed films. Langmuir. 1998 Sep 15;14(19):5636-48.

[48] Nelson RW, Krone JR. Advances in surface plasmon resonance biomolecular interaction analysis mass spectrometry (BIA/MS). Journal of Molecular Recognition. 1999 Mar;12(2):77-93.

[49] Myszka DG. Improving biosensor analysis. Journal of molecular recognition. 1999 Sep;12(5):279-84.

[50] Homola J, Yee SS, Gauglitz G. Surface plasmon resonance sensors. Sensors and actuators B: Chemical. 1999 Jan 25;54(1-2):3-15.

[51] Rich RL, Myszka DG. Advances in surface plasmon resonance biosensor analysis. Current opinion in biotechnology. 2000 Feb 1;11(1):54-61.

[52] Liedberg B, Nylander C, Lundström I. Biosensing with surface plasmon resonance—how it all started. Biosensors and Bioelectronics. 1995 Jan 1;10(8):i-x.

[53] Englebienne P. Use of colloidal gold surface plasmon resonance peak shift to infer affinity constants from the interactions between protein antigens and antibodies specific for single or multiple epitopes. Analyst. 1998 Jan 1;123(7):1599-603.

[54] Naimushin AN, Soelberg SD, Bartholomew DU, Elkind JL, Furlong CE. A portable surface plasmon resonance (SPR) sensor system with temperature regulation. Sensors and Actuators B: Chemical. 2003 Nov 15;96(1-2):253-60.

[55] Mauriz E, Calle A, Lechuga LM, Quintana J, Montoya A, Manclus JJ. Real-time detection of chlorpyrifos at part per trillion levels in ground, surface and drinking water samples by a portable surface plasmon resonance immunosensor. Analytica Chimica Acta. 2006 Mar 2;561(1-2):40-7.

[56] Kurita R, Yokota Y, Sato Y, Mizutani F, Niwa O. On-chip enzyme immunoassay of a cardiac marker using a microfluidic device combined with a portable surface plasmon resonance system. Analytical chemistry. 2006 Aug 1;78(15):5525-31.

[57] Luo Y, Yu F, Zare RN. Microfluidic device for immunoassays based on surface plasmon resonance imaging. Lab on a Chip. 2008;8(5):694-700.

[58] Ouellet E, Lausted C, Lin T, Yang CW, Hood L, Lagally ET. Parallel microfluidic surface plasmon resonance imaging arrays. Lab on a Chip. 2010;10(5):581-8.

[59] Fernández F, Hegnerová K, Piliarik M, Sanchez-Baeza F, Homola J, Marco MP. A label-free and portable multichannel surface plasmon resonance immunosensor for on site analysis of antibiotics in milk samples. Biosensors and Bioelectronics. 2010 Dec 15;26(4):1231-8.

[60] Novo C, Funston AM, Mulvaney P. Direct observation of chemical reactions on single gold nanocrystals using surface plasmon spectroscopy. Nature nanotechnology. 2008 Oct;3(10):598-602.

[61] Xiao Q, Zhou B, Huang S, Tian F, Guan H, Ge Y, Liu X, He Z, Liu Y. Direct observation of the binding process between protein and quantum dots by in situ surface plasmon resonance measurements. Nanotechnology. 2009 Jul 21;20(32):325101.

[62] Lange U, Hirsch T, Mirsky VM, Wolfbeis OS. Hydrogen sensor based on a graphene–palladium nanocomposite. Electrochimica Acta. 2011 Apr 1;56(10):3707-12.

[63] Lang, T., Hirsch, T., Fenzl, C., Brandl, F. and Wolfbeis, O.S., 2012. Surface plasmon resonance sensor for dissolved and gaseous carbon dioxide. Analytical chemistry, 84(21), pp.9085-9088.

[64] Soler M, Estevez MC, Alvarez M, Otte MA, Sepulveda B, Lechuga LM. Direct detection of protein biomarkers in human fluids using site-specific antibody immobilization strategies. Sensors. 2014 Jan 29;14(2):2239-58.

[65] Losoya-Leal A, Estevez MC, Martínez-Chapa SO, Lechuga LM. Design of a surface plasmon resonance immunoassay for therapeutic drug monitoring of amikacin. Talanta. 2015 Aug 15;141:253-8.

[66] Carrascosa LG, Huertas CS, Lechuga LM. Prospects of optical biosensors for emerging label-free RNA analysis. Trac Trends in Analytical Chemistry. 2016 Jun 1;80:177-89.

[67] Genslein C, Hausler P, Kirchner EM, Bierl R, Baeumner AJ, Hirsch T. Graphene-enhanced plasmonic nanohole arrays for environmental sensing in aqueous samples. Beilstein Journal of Nanotechnology. 2016 Nov 1;7(1):1564-73.

[68] Carrascosa LG, Huertas CS, Lechuga LM. Prospects of optical biosensors for emerging label-free RNA analysis. Trac Trends in Analytical Chemistry. 2016 Jun 1;80:177-89.

[69] Soler M, Estevez MC, de Lourdes Moreno M, Cebolla A, Lechuga LM. Label-free SPR detection of gluten peptides in urine for non-invasive celiac disease follow-up. Biosensors and Bioelectronics. 2016 May 15;79:158-64.

[70] Masson JF. Surface plasmon resonance clinical biosensors for medical diagnostics. ACS sensors. 2017 Jan 27;2(1):16-30.

[71] Huertas CS, Bonnal S, Soler M, Escuela AM, Valcárcel J, Lechuga LM. Site-specific mRNA cleavage for selective and quantitative profiling of alternative splicing with label-free optical biosensors. Analytical chemistry. 2019 Nov 5;91(23):15138-46.

[72] Masson JF. Portable and field-deployed surface plasmon resonance and plasmonic sensors. Analyst. 2020;145(11):3776-800.

[73] Wunderlich L, Hausler P, Märkl S, Bierl R, Hirsch T. Nanoparticle determination in water by LED-excited surface plasmon resonance imaging. Chemosensors. 2021 Jul 11;9(7):175.

[74] Écija-Arenas Á, Kirchner EM, Hirsch T, Fernández-Romero JM. Development of an aptamer-based SPR-biosensor for the determination of kanamycin residues in foods. Analytica Chimica Acta. 2021 Jul 18;1169:338631.

[75] Soler M, Lechuga LM. Biochemistry strategies for label-free optical sensor biofunctionalization: Advances towards real applicability. Analytical and bioanalytical chemistry. 2022 Jul;414(18):5071-85.

[76] Jobst S, Recum P, Écija-Arenas Á, Moser E, Bierl R, Hirsch T. Semi-selective array for the classification of purines with surface plasmon resonance imaging and deep learning data analysis. ACS sensors. 2023 Jul 28;8(9):3530-7.

[77] Pitarke JM, Silkin VM, Chulkov EV, Echenique PM. Theory of surface plasmons and surface-plasmon polaritons. Reports on progress in physics. 2006 Dec 7;70(1):1.

[78] Olaru A, Bala C, Jaffrezic-Renault N, Aboul-Enein HY. Surface plasmon resonance (SPR) biosensors in pharmaceutical analysis. Critical reviews in analytical chemistry. 2015 Apr 3;45(2):97-105.

[79] Zybin A, Boecker D, Mirsky VM, Niemax K. Enhancement of the detection power of surface plasmon resonance measurements by optimization of the reflection angle. Analytical chemistry. 2007 Jun 1;79(11):4233-6.

[80] Wong CL, Olivo M. Surface plasmon resonance imaging sensors: a review. Plasmonics. 2014 Aug;9:809-24.

[81] Wang D, Loo JF, Chen J, Yam Y, Chen SC, He H, Kong SK, Ho HP. Recent advances in surface plasmon resonance imaging sensors. Sensors. 2019 Mar 13;19(6):1266.

[82] Singh P. SPR biosensors: historical perspectives and current challenges. Sensors and actuators B: Chemical. 2016 Jun 28;229:110-30.

2. Development of SPR-Imaging Set-ups: Methods and Materials

2.1 Instruments

A CinCam CMOS-1.001-Nano is a compact and high-resolution **beam profiler** was used. It features a large sensor area and high pixel count for detailed beam analysis. The device is compatible with CINOGY's RayCi software for data acquisition and beam analysis. This model is tailored for different beam sizes and wavelength ranges in the UV-NIR spectrum. The substantial active area of the laser beam profiler offers a multitude of advantages. It permits the direct measurement of larger beam diameters, thereby simplifying the setup. When aligning an optical setup with an alignment laser beam, the large active area is capable of measuring beam wander or drifts over a larger field of view, which is crucial for monitoring beam stability. The active area of the beam profiler is 11.3 mm x 11.3 mm. The pixel size is 5.5 µm x 5.5 µm, resulting in a resolution of 2048 x 2048 pixels. The sensor has a wavelength range of 400 nm to 1150 nm. The dynamic range is 60 dB, the frame rate is up to 20 Hz, and the exposure time can be set between 100 µs and 100 ms. The housing of the beam profiler, with dimensions of 29mm x 29mm x 24mm, was incompatible with the 30 mm optical cage system of the SPR set-up. The housing was subsequently modified in consultation with the manufacturer at the time of the order. The manufacturer removed the corners and replaced them with radii with a diameter of 6 mm, ensuring precise mounting of the beam profiler in a 30 mm optical bench system. The beam profiler was used to develop the light source described in Chapter 4. It was also used to adjust the components in the SPR measuring station before implementing a beam profiler function in the measuring software.

The development of an optical system requires the performance to be checked at many points in time. A **power mete**r was applied for this task. This is initially necessary for safety reasons, whereby the systems must be classified in accordance with DIN EN 60825-1. The respective classification determines the protective measures to be taken. The standard prescribes the use of detectors with a measuring aperture of 7 mm in diameter, which corresponds to the average light entry area of the human eye. It should be noted that the OPM150UVS detector head used (Artifex 30.070.00004) has an aperture of 9 mm. However, this can be reduced using an aperture. The detector head has a sensitive wavelength range from 190 nm to 1100 nm. The power range is 1 nW to 5.5 mW at a wavelength of 532 nm. To extend the measuring range, an OD2 filter (Artifex 30.070.00015) was used if required. The detector head is connected to a computer using an OPM150 data acquisition unit (Artifex 30.070.00002). There, the power curve can be recorded using the software supplied. In addition to eye safety, the power meter was used for numerous other purposes, such as checking filters, installing beam splitters, checking power stability and cross-checking camera data.

SPR technology is highly dependent on the wavelength, which is why it is necessary to determine the wavelength and its distribution at numerous points. For LEDs, it is crucial to know their Central Wavelength (CWL) and Full Width at Half Maximum (FWHM) as both parameters can vary depending on the operating current. Lenses can have different AR coatings. Furthermore, the targeted tilting of a filter can be used to match the CWL of the LED and filter. A Qmini (formerly RGB laser systems, now Broadcom) **spectrometer** was used for the visible range. The wavelength range extends from 370 nm to 750 nm with a resolution of 0.3 nm. A Qmini (Broadcom) was used

for the NIR range. The wavelength range extends from 730 nm to 1080 nm with a resolution of 0.7 nm. Both spectrometers are equipped with an optical SMA-905 connection. This is a standardized connector interface defined by the IEC 61754-22 standard for fiber optic connectors. SMA stands for "Sub-Miniature version A". SMA connectors were originally developed for coaxial cable applications but were later adapted for use with optical fibers as well. The "905" in SMA905 indicates that the ferrule has an outer diameter of 905 micrometers, which is a standard size for single-mode fiber optic connectors.

The refractive index of solutions to test the SPR-set-up and to calibrate the sensitivity of all SPR set-ups to refractive index units was measured using a Krüss DR6300-T digital **refractometer**. This instrument has a measuring range of n_D = 1.32000 - 1.70000. The instrument has an accuracy of ±0.00002 nD and a resolution of 0.00001 nD. The measuring prism is made of sapphire. The measurement is performed at a wavelength of 589 nm. The device has an internal Peltier temperature control with a temperature control range of 10°C to 80°C and a temperature control accuracy of 0.1°C.

A Filmetrics F2T 3D **optical profiler** was used to measure the thickness of thin films by analyzing their optical transmission properties. The transmission-based measurement utilizes spectroscopic transmission.

A Dektak XT **profilometer** at the cleanroom of the physics department of the University of Regensburg was used. It employs a Low Inertia Sensor (LIS 3) with a variable stylus force ranging from 0.03 to 15 mg. The stylus has a 12.5 µm tip radius. The maximum scan length is 55 mm, with a capability of up to 120,000 data points per scan. The Dektak XT has a vertical range of 1 mm and a vertical resolution of 1Å (angstrom) at a 6.55 µm range. The step height repeatability is 4Å on steps $\leq$1 µm. It can accommodate samples up to 200 x 200 x 50 mm³ in size. Sample viewing is enabled by a digital magnification system with a vertical field of view ranging from 0.275 to 2.2 mm.

The Veeco (now Bruker) Dimension Icon **atomic force microscope** (AFM) was used to characterize the roughness of the glass prism. Samples with a size of up to 240 mm can be placed on the sample plate. The maximum scan size is 100µm x 100µm. The system achieves noise in the sub-Angstrom range in the Z-axis and Angstrom range in XY. The system has been used with TESPA-V2 tips. The tips have a nominal radius of 7 nm and a height of 10 µm to 15 µm. The front angle is 25°, the back angle is 17.5° and the side angle is 20°.

A Keyence VHX2000 high-performance **digital microscope** was additionally used for advanced surface analysis and characterization of surface topography, including contour measurements, area ratio calculations, and defect detection. The microscope was used to take the pictures presented in Chapter 6.3.

Samples heating was performed with in a Linn High Therm LM-412-Sonder **furnace**. The furnace is designed for a maximum temperature of 1060 °C. To prevent oxidation of the samples, the furnace has a connection for a protective gas. Argon or nitrogen can flow through the heating chamber of the furnace via this connection. Argon 4.6 (Westfalen Schutzgas ISO 14175-I1-Ar) was used for the experiments. To prevent damage or contamination of the prisms, they were placed in a glass jar (WECK RR60, 10013561) before being placed in the furnace. The oven chamber was heated up at a heating rate of 1°C/s. Before heating, the furnace chamber was flushed at a flow rate of 30 Nl/min. The flow rate was then reduced to 10 Nl/min. The oven was used to heat the samples used for the work described in chapter 6.3.

To optimize the 3D printing parameters, a **force gauge** was used in combination with a tensile specimen based on DIN EN ISO 527-2. The size of the tensile specimen was changed so that it could be torn with the force gauge. Once the sample size had been determined, the pressure parameters were varied to achieve the maximum possible stability. A PCE Instruments (PCE-FM 200) force gauge was used for the tensile tests. The device has a measuring range of up to 200 N with a measuring accuracy of +/-0.5%. The device was used to optimize the 3D printing processes mentioned in Chapter 2.11.

To fabricate mechanical components for the SPR set-up a Wabeco F1200 (Wabeco 11200) is a precision **milling machine** designed for accurate and efficient material removal was used throughout this work. It features a dovetail guide system and a lateral drive for the Z-axis with, ensuring smooth and precise movement along the vertical axis. The F1200 is equipped with an automatic feed system for the X-axis and Y-axis. The automatic feed mechanism allows the milling machine to advance the workpiece at a controlled rate during the cutting process, without the need for manual intervention by the operator. the automatic feed system ensures that the cutting tool removes material at a consistent depth, leading to a more uniform surface finish and improved dimensional accuracy of the workpiece. The machine was operated with the tool set offered by the manufacturer (Wabeco 11999). Among other things, it contains a machine vice, a titanium milling cutter set, collet chuck MK2 (Morsekegel) and collets. Parallel supports (Paulimot 14007) were used for clamping the workpieces. A dial gauge was used to align the machine vice (Holex, Ar.No. 4334101/58), the dial gauge was attached using a measuring stand with magnetic base and central clamping (PauliMot 21009). The cooling lubricant (Jokisch Monos Miko S3G) was applied using a "VERTEX" coolant spray system. The parts were cleaned after machining with an intensive cleaner (ROT-WEISS 9305).

A Flott Turbodrill **high-speed bench drill** designed for precision drilling of small holes was also used for the fabrication of mechanical components. It allows for a wide range of spindle speeds from 100 to 10,000 rpm. High speed and true running accuracy is critical when drilling small holes. Runout can cause the drill bit to cut an elliptical or out-of-round hole shape, rather than a perfect circle. Excessive runout puts additional stress on the drill bit, which can lead to premature failure, especially when drilling small holes that require high spindle speeds. A bad running accuracy can cause even an immediate failure of the drilling bit. Small holes were drilled with Bungard Hartmetall Bohrer (e.g. 81003 for 0,3 mm and 81900-02 for 0,2mm) larger diameter holes were drilld with Holex TYP N, DIN338 HSS (11 5050_1-6). Taps were drilled with Ruko TYP N, DIN338 HSS drill bits and TYPE B, DIN371/376 HSS Tap Drill bits. Cutting and drilling oil (PRESSOL 10571) or grease (BOC BP-40) was used for lubrication.

Rapid prototyping, a process primarily involving the production of parts through additive manufacturing (3D printing), offers significant advantages over traditional manufacturing methods. While simple parts can be fabricated within a week using subtractive techniques such as CNC machining or turning, 3D printed parts consistently reduce lead times across a broader range of materials and geometries. The inherent nature of 3D printing, which directly translates data from a 3D CAD model into a physical part without or with only minor additional machine setup time, enables the production of nearly all given designs within hours.

Many 3D printing technologies are more cost-effective than traditional prototyping methods like CNC machining. Rapid prototyping facilitates the testing of intricate designs that would otherwise be costly and time-intensive to produce using conventional methods. Additionally, 3D printing

allows to produce items with complex geometries that cannot be easily achieved with CNC machining or sheet metal fabrication without specialized tooling.

PolyJet 3D printing is a technology that uses liquid photopolymers, UV light and inkjet heads to create precise parts. This process enables the creation of models with high precision. Photopolymer droplets are sprayed onto the build platform in layers. These droplets form digital materials. The layers are then cured with UV lamps and rolled and bonded together. The result is smooth, precise parts, prototypes and tools. Within this work a Stratasys Objet 500 with VeroClear RGD810 was used. After 3D printing, the support material still needs to be removed from most models. The material is dissolved in lye and then removed with a water jet device (Krumm RKTOP 5 XL VA). Polyjet 3D printing was used to produce the bubble separators.

Fused Layer Modelling (FLM) is a manufacturing process within the realm of additive manufacturing. In this process, a workpiece is constructed layer by layer using a meltable material, typically a thermoplastic polymer. An alternative term for this method is "Fused Filament Fabrication" (FFF) or "Fused Deposition Modeling" (FDM). In this process, a filament-shaped material (commonly referred to as "filament") is guided through a heated nozzle, where the material is melted and deposited onto a build platform or a previously printed layer. The deposited material solidifies, and the cooling process is typically supported by a fan. This results in the gradual construction of a three-dimensional object with a characteristic linear structure aligned with the chosen layer thickness. To ensure reliable stability and prevent part displacement during printing, it is essential that the initial layer applied by the print head forms a strong bond with the build platform. Various methods are employed to achieve this, including the heating of the build platform, which can enhance the adhesion.

For applications demanding enhanced mechanical strength, fiber-reinforced materials are frequently utilized in 3D printing. These materials necessitate the use of larger nozzle diameters to accommodate their extrusion, as they tend to clog smaller nozzles due to their composition. Additionally, fiber-reinforced filaments exhibit abrasive properties, which can rapidly erode standard brass nozzles. Consequently, the use of hardened nozzles (V6 Nozzle X - 1.75 mm, 0.60 mm) with a larger diameter was used to mitigate premature wear and ensure consistent print quality. Considering this boundary conditions, it is not a drawback if a printer is slow. Therefore, the Prusa MK3 was used for processing fiber reinforced materials for parts that need extraordinary strength.

Many FLM 3D printers are capable of processing materials up to a printing temperature of 250°C. This limitation is primarily due to the presence of a polytetrafluoroethylene (PTFE) tubing within the heatbreak assembly. The heatbreak is a metal tubing that separates the heating block from the cooling block, featuring a PTFE liner inside. The metal tube provides a robust connection between the heat and cooling blocks, while the PTFE liner insulates the filament from the heatbreak, preventing premature melting within the assembly. Unfortunately, one end of the PTFE tubing is in close proximity to the heating block, where temperatures can exceed 250°C, leading to degradation of the PTFE material. To overcome this limitation, the standard heatbreak has been replaced with a bimetal heatbreak (BROZZL V6 Bi-Metal Heatbreak). This innovative solution consists of an extremely thin titanium tube with a copper thread at the cold end and a titanium thread at the hot end. The copper thread at the cooling block side facilitates rapid cooling of the heatbreak, while the titanium thread at the heating block slows down the heat transfer into the heatbreak. Titanium's low thermal conductivity and the small dimensions of the tubing eliminate the need for

a PTFE liner, enabling higher printing temperatures without material degradation. The enhanced Prusa MK3S+ printer was used to print the base of the central joint of the central joint.

A smoother and more precise motor movement, enabling higher print speeds while maintaining excellent print quality was included in a newer version of the Prusa printer by improving the Klipper control software. This helps to reduce extruder oozing and improve print quality, particularly in corners and detailed areas. Input shaping is another feature that helps to cancel out resonant frequencies in the printer's mechanical system, reducing ringing artifacts and enabling higher print speeds without sacrificing quality. This updated Prusa MK4 printer was used to produce the prototypes of the central joint, the corner joints and the prism mount.

Smaller nozzle diameters allow for printing finer details and higher resolution along the X and Y axes. A nozzle size like 0.25mm can produce extremely precise and intricate prints with sharp corners. This makes small nozzles ideal for printing objects requiring high levels of detail. Smaller nozzles paired with thinner layer heights can minimize the visible "stair-stepping" effect on sloping and curved surfaces, resulting in smoother and more functional prints. The layered structure of 3D prints is less apparent, leading to an improved surface finish. The main trade-off of using a small nozzle diameter is significantly longer print times, as the nozzle has to deposit smaller amounts of material. Additionally, smaller nozzles are more prone to clogging, especially with abrasive or particle-filled filaments. A stock Prusa mini printer has a single gear extruder, which can be a disadvantage in some cases. Dual drive extruders utilize two geared hobbed pulleys that grip the filament from opposite sides. This provides significantly more traction and grip on the filament compared to a single gear. Dual drive extruders distribute the gripping force evenly on both sides of the filament, minimizing filament deformation and grinding. Tribology filaments like igus iglidur 150 are notoriously difficult to print with single gear extruders due to their tendency to grip poorly. This drawback of a single gear extruder becomes even more prominent if the filament has to be pressed through a nozzle with a small diameter. The increased traction provided by dual drive extruders allows for reliable extrusion of these tribo-materials. Additionally, the improved grip and extrusion force of dual drive extruders enable higher print speeds without sacrificing print quality or risking under-extrusion issues. To overcome these challenges the Prusa mini was equipped with a Bondtech dual drive gear extruder and a low friction Plated copper 0.25 mm Nozzle from Brozzl. This Setup enables extremely fine prints. Different filament materials require different print bed surfaces due to their varying properties and adhesion characteristics. A textured surface provides mechanical grip, allowing the molten plastic to adhere during printing. For example, polyamide and polycarbonate filaments have different adhesion requirements. These materials tend to stick too well to textured surfaces, making part removal difficult. For these filaments, a smooth PEI sheet is recommended. The smooth surface allows the printed part to release more easily once cooled. Tribo-filaments who are made to not stick to others surfaces need a special print bed. Therefore, a standard Prusa mini print bed was equipped with an adhesive film for print beds (igus PF-01-0203-0203). The Prusa mini was used to print prototypes of the Flow Cells, the sliding bearings and the camera adapter of the miniaturized SPR-Sensor.

Different **filaments** offer varying mechanical properties, such as strength, flexibility, and temperature resistance, which are crucial for specific applications. For example, ABS and PETG are strong and impact-resistant, making them suitable for functional prototypes and durable parts. TPU is flexible and ideal for applications requiring elasticity, like gaskets or protective coatings. Nylon is strong and wear-resistant, suitable for gears, bearings, and other functional parts subjected to high stress. All these filaments have different temperature requirements and different printing speeds,

for optimal printing. Matching the filament to the printer's capabilities and environmental conditions (e.g., enclosure) is essential for successful printing and part quality.

Bavafil ReproPLA. By utilizing recycled PLA as the raw material, Bavafil ReproPLA helps reduce the demand for new plastic production, which is energy-intensive and contributes to greenhouse gas emissions. The recycling process for Bavafil ReproPLA likely requires less energy and generates fewer emissions compared to manufacturing virgin PLA from scratch. This results in a lower overall carbon footprint for the filament. Bavafil ReproPLA is also more cost-effective than virgin PLA filaments, as it utilizes waste materials as the primary input. As a locally recycled filament, Bavafil ReproPLA supports regional sustainability efforts and reduces the environmental impact associated with long-distance transportation of materials. Bavafil ReproPLA filament was used for all initial designs and prototypes. It is an inexpensive and environmentally friendly material that can be used to test initial properties and fits.

Extrudr GreenTEC Pro offers several advantages over standard PLA filament. It exhibits outstanding mechanical and thermal resistance compared to regular PLA. It has high rigidity, flexural strength, and can withstand temperatures up to 160°C without deforming. This makes it suitable for technical high-performance applications requiring durability and heat resistance, which PLA lacks. GreenTEC Pro exhibits minimal warping (less than 0.5%) during printing, which can be a common issue with PLA, especially for larger prints. This results in better dimensional accuracy and reduced need for brims or rafts. Unlike some temperature stable filaments like ABS, GreenTEC Pro is odor-free during printing, making it more save to use. This filament was employed to print components with intricate details. In contrast to fiber-reinforced materials, it can also be processed with small nozzle diameters due to its favorable flow properties. The holder for the camera within the miniaturized SPR sensor was printed from GreenTEC Pro.

The incorporation of carbon fiber reinforcement in **GreenTEC PRO Carbon** offers several advantages over GreenTEC PRO. The incorporation of carbon fibers significantly enhances the mechanical strength and rigidity of the material. It exhibits a slightly higher heat resistance, with a VICAT softening temperature of 165°C. The incorporation of fiber reinforcement results in a lighter and more wear-resistant material. In terms of opto-mechanical components, the most notable advancement is the enhanced stiffness, which is accompanied by a matt surface finish that reduces reflection. The legs of the central joint and the mounting plates of the corner posts were printed from GREENTEC PRO Carbon.

The **add:North PC Blend HT LCF** filament is a polycarbonate (PC) composite reinforced with long carbon fibers (LCF). The incorporation of these fibers significantly enhances the stiffness and rigidity of the filament compared to unreinforced PC. Carbon fibers have an exceptionally high tensile modulus, resulting in improved dimensional stability and resistance to deformation in printed parts. The PC Blend HT LCF filament exhibits excellent heat resistance, with a maximum operating temperature of 185°C. Like conventional PC, PC Blend HT LCF exhibits outstanding chemical resistance, rendering it suitable for applications involving exposure to various chemicals and solvents. Printed objects made with PC Blend HT LCF exhibit a distinctive matte surface finish with visible carbon fiber strands. The base of the central joint is made of PC Blend HT LCF.

iglidur® i150 is a high-performance 3D printing filament. It exhibits outstanding abrasion resistance and low friction, making it suitable for applications involving sliding or wear-intensive environments. The filament boasts a relatively high mechanical strength and stiffness, providing exceptional rigidity and load-bearing capacity. iglidur® i150 is certified as food-safe according to EU 10/2011 regulations, which is suggesting that this material will not contaminate the analyte matrix

when put in contact with it. The bearings of the central joint and the corner joints were made from iglidur i150.

Proto-pasta conductive PLA exhibits electrical conductivity due to the presence of conductive additives. The conductivity of printed parts is anisotropic, meaning that the resistance varies depending on the direction of measurement. The volume resistivity along the print layers (x/y) is lower (30 Ω cm) compared to the resistivity against the layers (z) (115 Ω cm). While the conductive additives enhance the electrical properties of the filament, most characteristics of PLA are retained. Customized housings for electronic components were printed from Proto-pasta conductive PLA.

Filament dryer. Most common 3D printing filaments, including PLA, ABS, PETG, and nylon, are hygroscopic to varying degrees. When hygroscopic filaments are exposed to ambient air, they can absorb and retain water molecules within their polymer structure. This absorbed moisture can have detrimental effects on the 3D printing process and the quality of the printed parts. During the extrusion process, the absorbed water vaporizes due to the high temperatures involved, leading to several issues. For example, the rapid vaporization of water trapped within the filament can cause bubbling and foaming in the molten plastic, resulting in a porous and weakened printed part. Moisture can affect the viscosity and flow properties of the molten plastic, leading to excessive stringing, oozing, and poor dimensional accuracy. Furthermore, the presence of moisture can lead to hydrolytic degradation of the polymer chains, reducing the overall strength, ductility, and impact resistance of the printed parts.

To mitigate these issues, it is crucial to dry the filaments before printing, especially for materials with high hygroscopicity. The drying process involves exposing the filament to elevated temperatures, typically between 60°C and 90°C, for an extended period, allowing the trapped moisture to evaporate. Fiber-reinforced filaments, such as GreenTEC Pro Carbon, have an even greater need for drying due to their composite nature. The reinforcing fibers can act as pathways for moisture to penetrate deeper into the filament, exacerbating the issues mentioned above. Additionally, the presence of moisture can adversely affect the fiber-matrix interface, leading to poor adhesion and reduced mechanical properties of the printed parts.

A Graef DA506 dehydrator (DA506EU) was used to dry the filaments. The temperature can be set between 30°C and 70°C. The drying time can be set to up to 40 hours. The filaments were dried with the parameters shown in Table 2.1.

Table 2.1: Filament drying times and temperatures.

Filament	Drying Temperature	Drying Time
PLA	45°C	3 h
GreenTEC Pro Carbon	60°C	5 h
PETG	65°C	3 h
PA	65°C	5h
ABS	70°C	3h
ASA	70°C	3h
PC	70°C	5h

One should note that it is essential to consult the filament manufacturer's guidelines for specific drying recommendations, as the optimal temperature and time may vary depending on the brand and composition of the material. Proper drying practices, while staying below the material's glass transition temperature, are crucial for maintaining the quality and performance of 3D printed parts.

Postprocessing SLM 3D printed parts. The first layer of an SLM 3D print often shows a slight thickening of the structures in the first layer, in technical jargon this effect is often referred to as elephant feet. In some cases, this is unavoidable as the first layer has to be pressed more firmly against the print bed to ensure adequate adhesion. If this slight thickening interferes because an exact fit is required on the structure adhering to the base, this thickening must be removed. Some 3D models only have a very small contact surface on the print bed, which can lead to adhesion problems. In this case, a very wide but single-layer rim is often printed around the component. This edge must then be removed after printing. A precision triangular spoon scraper (Rennsteig 9R 4661500) was used to remove these structures. A deburrer (Exact SCR-8) was used for structures with overhangs or in curves. The deburrer has different, interchangeable blade geometries so that the blade can be adapted to the component to be processed.

In some cases, simply removing excess material for reworking is not enough. This may be the case, for example, if a surface is not smooth but should not be sanded. Also, if a structure does not fit exactly but should not be drilled due to the low wall thickness. Sometimes cracks occur in a component that need to be closed again. In these cases, post-processing is carried out with a 3D printing finishing tool (Modifi3D, M3D-PRO).

Resin 3D printing offers several advantages over other 3D printing technologies, particularly in terms of print quality, resolution, and surface finish. Resin 3D printers, such as digital light processing (DLP) technologies, can achieve extremely high resolutions, with layer heights as low as 25 micrometers and below. This allows to produce parts with intricate details, fine features, and tight tolerances that are difficult to achieve with other 3D printing methods like fused layer modeling (FLM). Parts printed with resin exhibit exceptional surface quality, with minimal visible layer lines or stair-stepping effects, which is an advantage if it comes to microfluidic components. Resin-printed parts tend to have isotropic material properties, meaning their mechanical properties are consistent in all directions. This is due to the uniform curing process, which results in a homogeneous material structure. Resin 3D printing offers a diverse range of photopolymer resins with varying properties, including rigid, flexible, castable, biocompatible, and high-temperature resins. This versatility allows to produce parts with tailored mechanical, thermal, and chemical properties for specific applications. Flexible materials are very difficult to process in FLM 3D printing. The processing of soft materials in FLM printing is particularly challenging when it comes to the creation of more complex structures.

The Anycubic Photon D2 employs a Texas Instruments DLP projector with a resolution of 2560 x 1440 pixels at a printing area of 130.56 mm x 73.44 mm. This results in a printed-pixel size of approximately 51 micrometers. This high resolution enables the production of intricate details, fine features, and tight tolerances that are challenging to achieve with other 3D printing technologies. One of the primary advantages of DLP technology over masked stereolithography (MSLA) is reduced light bleed, which is a common issue in MSLA printers.

3DJake ecoResin is an inexpensive and budget-friendly resin, making it an economical choice for various applications, especially prototypes. The resin has a low odor compared to many other resins, and it uses BPO instead of the otherwise typical TPO. BPO is presumed to have a lower toxicity than TPO. The resin exhibits low shrinkage during curing, resulting in precise and accurate 3D printed models with minimal dimensional inaccuracies. 3DJAKE ecoResin was used for first prototypes of printed resin parts.

Liqcreate Bio-Med Clear is a biocompatible 3D printing resin designed for use with DLP and laser-based 3D printers operating in the 385-420nm wavelength range. Bio-Med Clear employs a Type I

photoinitiator system based on benzoyl peroxide (BPO) in place of the more commonly used Type II photoinitiators, such as camphorquinone (CQ). Benzoyl peroxide (BPO) undergoes photodissociation under ultraviolet and visible light to generate free radicals that initiate polymerization. This photoinitiator system contributes to the resin's biocompatibility by avoiding the potential for harmful components found in some Type II photoinitiators. Upon completion of the requisite post-processing, 3D-printed components manufactured using Bio-Med Clear successfully pass the following biocompatibility tests: cytotoxicity (ISO 10993-5:2009), sensitization (ISO 10993-10:2021) and irritation (ISO 10993-23:2021). This renders them suitable for applications requiring biocompatibility. In order to achieve biocompatibility, a specific post-processing protocol must be followed. The parts must be washed in isopropyl alcohol or ethanol for a minimum of two minutes in an ultrasonic cleaner (EMAG Technologies, Emmi-40HC), and then washed again with fresh solvent. Afterwards, the parts must be dried under ambient conditions for a minimum of 60 minutes. Then the parts must be cured with UV light at 60 degrees Celsius. Printed parts from Bio-Med Clear can be disinfected with commonly used disinfectants and sterilized by steam sterilization at 121°C (250°F) or 134°C (273°F) without significantly altering their properties. Liqcreate Bio-Med Resin was used for fabrication of flow cells.

Postprocessing resin 3D printed parts. After the printing process, the components remain in the 3D printer for a few minutes so that the uncured resin can drip off the component. The exact time depends on the viscosity of the resin. The component is then removed from the build platform and roughly cleaned by immersing it several times in a pre-wash container filled with isopropanol (Höfer Chemie, 10020013). It is then transferred to a washing station (Elegoo, Mercury Plus). In the washing station there is a container with a basket into which the components are placed. Under the basket is a rotor that alternately flushes the cleaning fluid (3DJake, AOE-RCL-5000) through the component in both directions. The component is then washed again with isopropanol in the same station, but in a different tank. After cleaning, the components are blown dry with compressed air and then dried for a day at room temperature. Once the components are completely dry, they are cured according to the resin manufacturer's instructions. A curing station (Elegoo, Mercury Plus) is used for this purpose. In contrast to most commercially available curing stations, which only expose at 405 nm, this station exposes at both 405 nm and 385 nm.

As most of the curing stations available on the market do not offer the option of heating the components during UV curing, a separate curing station was produced for the post-treatment of BioMed components. An aluminum box (Alutec, Basic 80) serves as the housing. An LED lamp (Natpow UV, 100 W, 395 nm) was embedded in one side and in the lid. A solar-powered turntable (Sovol, XZBDS) is located in the box to ensure that the components are exposed evenly. The curing station is heated with a fan heater (supplement). The cut-out edges for the spotlights and the cable feedthroughs were fitted with edge protection to prevent injury or damage (HellermannTyton, SM1-PVC-BK-75M).

The **selective laser melting** (SLM) process is an additive manufacturing technique used for producing three-dimensional metal parts directly from metal powder. At the SLM process, a thin layer of metal powder is spread evenly over a build platform using a recoating mechanism. A high-powered laser beam selectively melts and fuses the powder particles together in the desired areas, following the geometry defined by a 3D computer-aided design (CAD) model sliced into layers. The build platform is lowered by one layer thickness, and a new layer of powder is spread over the previously melted layer. This process is repeated layer-by-layer until the entire 3D part is built up from the melted and solidified metal powder. After printing, any unmelted powder is removed, leaving the final metal part attached to the build platform. The SLM process is conducted in an inert

gas atmosphere (typically argon or nitrogen) to prevent oxidation and degradation of the metal powder during melting. Here an EOS M100 3D-printer was used. Its build volume is 100 mm in diameter and 95 mm in height. The layer thickness is 20 µm, available materials are aluminum, stainless steel and titanium.

After printing, the build platform must be removed from the printer. This requires a FFP3 respirator (UVEX silv-Air 2310). A protective suit (Wodes DEKOSAVE PLUS) should also be worn. The metal dust remaining in the construction platform is extracted with a special hoover (Ruwac Industriesauger NA 35-D1 type III). The vacuum cleaner has a residual dust filter of dust class H and a cartridge filter of dust class M. As fine metal dusts are not only harmful to health but also highly flammable, the cleaner also has an ATEX EX II 3D classification. The vacuum cleaner also has a liquid separator. The metal dust is thus separated in an oil bath to prevent it from coming into contact with the air and starting to burn.

When taken from the printer, the component must be removed from the building platform. A saw with an HSS-Co Bihart Cobalt handsaw blade (RUKO 312130024R) was used for this purpose. The HSS bi-metal handsaw blade consists of two different steels. The cutting edges of the saw blade are made of hard HSS molybdenum steel, while the saw blade body is made of alloyed heat-treated steel. The combination of these two steels results in an extremely wear-resistant saw blade with good cutting properties.

The parts have a rough surface after the printing process, which has a negative effect on their dimensional accuracy. Therefore, post-processing is necessary in most cases. Two methods were used to remove the roughness. The processing methods used were sandblasting and barrel polishing. Sandblasting was performed in a sandblasting cabin (Leering Hengelo BV, type DI-12). The cabin has a maximum working pressure of 8 bar, which can be adjusted by the user. To minimize material removal and instead achieve material compaction, ceramic beads with a diameter of 150 µm to 250 µm were used instead of an abrasive medium such as walnut shells.

Drum polishing was carried out in a rubber drum (Horbach GmbH, Schleif- und Poliermaschine, type TRM-1A/2A). In contrast to sandblasting, this is an abrasive process due to the polishing media contained in the drums. As the abrasive particles are larger than the ceramic beads, very small openings cannot be polished. In contrast to sandblasting, however, cavities with correspondingly large openings can also be polished.

2.2 Mechanical Platform

In the quest of developing an advanced Surface Plasmon Resonance imaging system tailored to meet the specific requirements of sensor applications, it became essential to construct a versatile laboratory instrument. This apparatus, referred to as open SPR laboratory set-up, was designed with the primary objective of facilitating rapid interchangeability of all critical components. This design philosophy enables researchers to systematically evaluate the impact and potential enhancements achieved through modifications to the setup or the integration of novel components. The open architecture of this instrument allows for comprehensive assessment and optimization of various elements within the SPR imaging system. By providing a flexible platform for experimentation, researchers can efficiently test and refine different configurations, thereby accelerating the development process and enabling iterative improvements in SPR sensor technology. This approach is particularly valuable in the context of academic and industrial research, where the ability to quickly adapt and refine experimental setups is crucial for advancing the field of SPR-based sensing and imaging (Figure 2.1).

Figure 2.1: Open SPR laboratory system. The open ends of the V-shaped rods are mounted rotatable and with bush bearings. The center of the V is mounted on a linear stage. If the linear stage is moving, the angle of the V is altered symmetric. This enables to change the SPR angle over a wide range. The left branch contains the light source while the right branch contains the detector. The prism is mounted at the hinge at the center of the system. The light source and the prism are equipped with an active temperature regulation. The smallest angle step size of the system depends on its configuration. The one used within this work is around 0.01°. The structure of the branches is made of a standard optical cage system. This allows the user to modify the system easily.

The open SPR laboratory system is mounted on a base plate consisting of an OPTA breadboard of type BS 33. The board is 33 mm thick and has a 3 mm thick magnetic cover plate. The flatness of the board is ± 0.1 mm. It has encapsulated M6 threads with a grid dimension of 25 mm for fastening components. The edge distance is 37.5 mm. The individually encapsulated nuts are particularly important with regard to liquid leaks during the tests. These prevent leaked liquid from spreading over the entire breadboard. Thanks to the magnetic cover plate, posts and components can also be mounted outside the 25 mm grid for special tasks.

The placement of posts on an optical table without guidance can result in user errors. One example of this is the asymmetrical positioning of the posts. Additionally, the optical table, with its steel plates and honeycomb base construction, is a heavy and immobile object. To enhance user-friendliness, reduce costs, and facilitate transportability, a base plate was developed that is specifically tailored to the device (Figure 2.2).

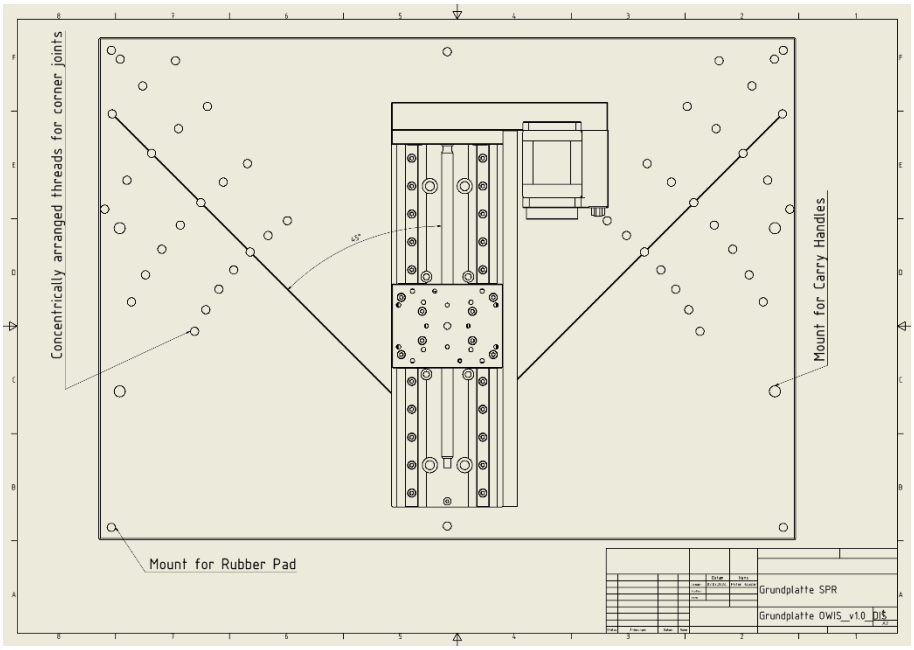

Figure 2.2: The linear stage and corner joints are mounted on the base plate. The linear table is fixed in the center of the base plate. The corner supports can be mounted concentrically at various distances around the end position of the linear table slide. A line marks the 45° mark. If this mark is not exceeded, the two branches cannot collide.

The position of the corner posts is decisive for the angular resolution. However, the relative position of the corner posts to the linear stage also determines the angular range that the stage can cover. The distance of the posts perpendicular to the axis of the linear stage also determines the length of the installation space that can be utilized within the optical bench. Standard breadboards that are available for optical setups have a rectangular pattern with a spacing of 25 mm. When using such a breadboard, there is a risk of misplacing the components, as it can be difficult to determine the correct column and row. For a portable version the specially designed base plate was made of 15 mm thick and black anodized aluminum. The black anodization prevents distracting or dangerous reflections on the plate. To enable the base plate to be levelled, it has been equipped with screw feet at the corners. The feet were designed as rubber-metal buffers to decouple the system from any disruptive vibrations.

The central joint is the part where the prism is fixed (Figure 2.3). The hexagon socket drive offers approximately ten times more force transmission than a comparable cross recess. The hexagon socket drive of the screw also reduces the risk of the tightening tool slipping, in contrast to a Philips or Posidrive cross recess. If the tool were to slip, there is a high probability that the drive would be damaged. As the screws are almost even with the contact surface of the prism, this would also result in damage to the prism. L-shaped angle wrenches are also available for the hexagon socket drive; these allow the screw to be tightened with sufficient force even in the confined spaces of the support frame. The support frame for the prism is attached to a 20 mm thick bolt made of polished stainless steel. There are flattened areas at the ends of the bolt. These make it possible to hold the bolt with an open-end wrench of size 17 according to DIN 3113. There is an M6 thread to ISO 965-

1 on each end face of the bolt. The hole containing the thread is chamfered to ensure that the support frame fits evenly on the bolt.

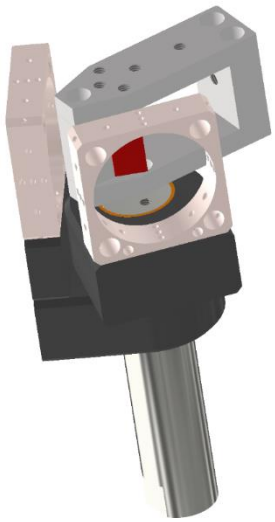

Figure 2.3: The central joint is equipped with a polished stainless-steel bolt that is mounted in a base on the slide of the linear table. This allows for rotation and adjustment in height, as well as fixation for measurements. The optical branches are attached to the bolt via wings that are mounted on a plain bearing, enabling rotation and adjustment in height. The holder for the prisms can be mounted on the bolt using either an M6 thread or two M4 threads.

The detector and the light source are each mounted in a standardized optical bench such as those available from standard distributors (e.g., Linos). To ensure that these branches move symmetrically around the prism, they are attached to the base bolt with rotating legs. To allow the position of the branches to be adapted to the size of the optical SPR element (e.g. prism), the legs can be moved up and down on the rod. To ensure that the arms remain movable along the axis of the base bolt, plastic plain bearings were used instead of pressed radial ball bearings. The plastic plain bearings also require considerably less installation space, which made it possible to design the legs much narrower. To connect the optical bench, the flanges have two 4.1 mm holes with a hole spacing of 20 mm. The holes have additional countersinks with a diameter of 8 mm and a depth of 6 mm in order to be able to countersink a DIN 912 screw head. These boreholes make it possible to attach a mounting plate. A Linos G061047000 plate was used here, as it already has two threads at a distance of 20 mm. However, these threads are M2.3 in size and must be adapted accordingly before use. A Flott Turbodrill drill press with thread cutting function was used to insert the new threads. The 3.3 mm core holes were drilled using an HSS drill according to DIN 338 type N. The threads were tapped with a DIN 371 type B machine tap. Ethanol was used as a cooling lubricant to prevent the aluminum alloy from sticking to the cutting tools.

Figure 2.4 illustrate the optical branches. The branches require a certain distance from the central joint so that they can be rotated around it. Since the aim of this work is to miniaturize the SPR system, an attempt was made to keep the distance between the central joint and the optic branches as small as possible. As the angle-adjustable SPR system is a research and development system, it should offer as much flexibility as possible. With regard to the SPR angle, this means an angle range of 45° to 90° for SPR imaging. Looking at the systems structure it is obvious that the width of the prism mount also determines the length of the rotatable legs of the central joint. To ensure the aforementioned flexibility, attention was paid to possible interoperability with commercial optomechanical components. Optomechanical cage systems are available in rod spacings of 16 mm,

30 mm, 40 mm and 60 mm. The 30 mm system has been implemented as standard, as components in this size are available on the market from most major suppliers. However, the other system sizes can be mounted using adapters or branch-mounting-legs in other sizes.

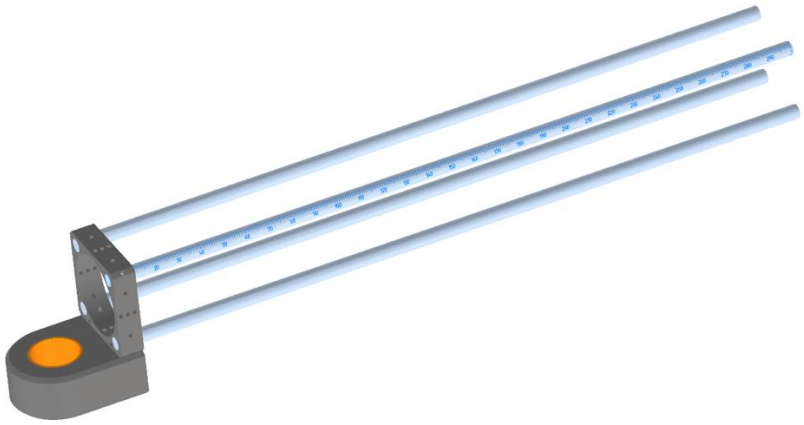

Figure 2.4: Optic branch with mounting wing from the central joint.

A rod with a length scale (LINOS G061241000) was used in each arm to better control the placement of the components. During the development phase, when components are frequently replaced, magnetic mounts (G061034000) or mounting plates that can be removed (G061031000) have proven to be advantageous. However, this assumes that the rods used are ferromagnetic. Some suppliers of optomechanical components, however, sell rods made of stainless steel, which are unsuitable for this purpose. The standard systems with 6 mm rods are sufficient for systems with a rod spacing of 60 mm and a length of up to 400 mm. With longer systems, however, the 6 mm rods become unstable, which reduces reproducibility. Thicker rods are therefore required for longer systems. The PCO Edge 4.2 camera is too large for a 60 mm optical bench system and either too long for 400 mm rods or the adjustable angle range is very small. A 100 mm optical bench system with 8 mm thick rods was therefore developed for the PCO Edge 4.2 camera.

The corner posts have been optimized for two different application scenarios. Scenario 1 is the highest possible accuracy. Scenario 2 is to maximize operational reliability. Similar to posts from the major optomechanics suppliers, the corner posts consist of a base into which a rod is inserted. Components can be mounted on the rod. As with Linos components, the diameter of the rod is 14 mm. It has a 10 mm deep M4 thread on one end and a M6 thread on the other end. To ensure that the components mounted on the post lie flat, the edges of the post are slightly chamfered in addition to the threads. A major disadvantage of standard posts from optomechanics suppliers is the large amount of play between the post and its base. If the rod is not screwed into the base, it will wobble around. To overcome this problem, a special base has been designed and manufactured. Slide bearings are pressed into the bore of the corner post base. The polished bar is then inserted into the prepared base. This creates a backlash free radial bearing of the rod in the base. When the SPR angle is adjusted, these joints are rotating. The height of the mounted branch can be adjusted in two ways, the first one is to inserts between the rod and the base some spacer slides, the second one is to insert a screw into the bottom thread of the rod. Figure 2.5 shows the half section of an assembled corner joint.

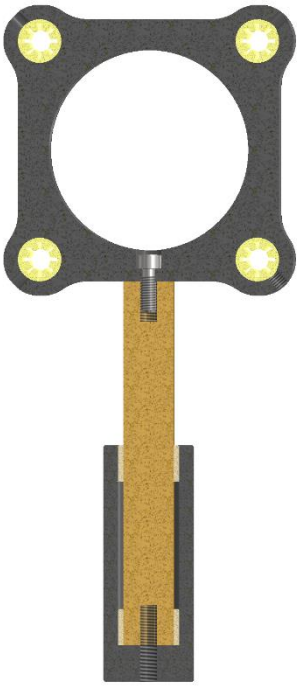

Figure 2.5: Corner Joint. The base of the corner joint can be attached to the base plate provided for the SPR measuring device using an M6 thread in the base and a grub screw to DIN 914. Two plain bearings are pressed into the base. These enable the joint post to be mounted without play and with low friction. The base is made of black anodized aluminum to minimize reflections. The post, on the other hand, is made of polished brass to achieve the best possible gliding properties. A mounting plate suitable for the respective cage system is mounted on the post using a burnished M4 screw to DIN 912. Plain bearings (igus RJMP-01) are pressed into the mounting plate. These enable the optical bench systems to slide through the mounting plate when the angle is adjusted.

Figure 2.6 illustrates the fundamental principle underlying the adjustment of the angle in a symmetrical manner. The linear stage, which serves as the foundation for the central joint, is situated in the center. The base of the central joint houses a bolt that serves as the axis of rotation for the wings bearing the light source and detector. The SPR-sensitive element is mounted on the bolt of the central joint. As the slide of the linear stage, on which the base joint is mounted, moves, the optical branches rotate around the joint. Simultaneously, the corner joints, on which the wings are mounted, rotate. However, the distance between the central joint and the corner joint changes when the central joint is moved, which is why the wings are mounted in linear plain bearings in the corner joints.

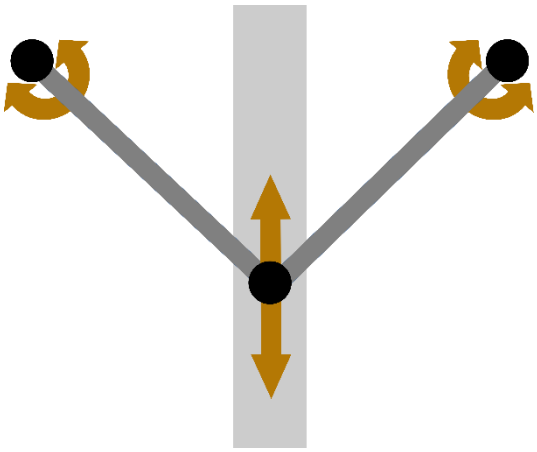

Figure 2.6: SPR-Linear Stage, the central joint is mounted on top of the linear stage slide, the wings are fixed to the legs of the central joint and inserted into the corner joints. If the slide of the linear stage is moving, the corner joints are rotating, and the SPR-angle is adjusted.

The OWIS LTM80 linear stage utilized in this study has a travel distance of 195 mm. It is driven by a 2-phase stepper motor and has a load capacity of 150 N, with a positioning force of 60 N. The bidirectional repeatability error is less than 15 µm, and the positioning error per 100 mm is less than 25 µm. The spindle of the linear stage has a lead of 1 mm per revolution, and the stepper motor has 200 steps per revolution. Given the system configuration, this data can be used to calculate the maximum possible angular resolution. As angular distortion may occur with distance increments, it is recommended to perform adjustments in angular increments.

2.3 Optical Coupling System and Fluidic Components

The selection of suitable refractive index couplers for SPR sensors is a complex process, influenced by numerous factors. The most evident factor is the refractive index, followed by the geometry. The refractive index is a function of the material selected and the wavelength employed. The materials in question exhibit specific absorption and transmission characteristics, which are a priori dependent on the wavelength. **Glasses** also exhibit a temperature-dependent refractive index, whereby the temperature dependence of the refractive index in turn depends on the wavelength [1].

In data sheets for technical glasses, refractive indices are usually only given for very prominent wavelengths such as the d-line at 587,6 nm. The refractive indices for the wavelengths 660 nm and 730 nm used in this work were not specified in the data sheets. As a result, the Sellmeier equation was used to calculate the refractive indices. The Sellmeier Equation is ideal for describing the progression of refractive index from UV to IR. It allows for accurate calculation of intermediate values using a single set of data to describe the entire transmission region [2].

$$n^2 = 1 + \frac{B_1\lambda^2}{\lambda^2 - C_1} + \frac{B_2\lambda^2}{\lambda^2 - C_2} + \frac{B_3\lambda^2}{\lambda^2 - C_3}$$

The Sellmeier equation is a functional description of the dependence of the refractive index (n) of a medium on the wavelength (λ) of the light. It is determined empirically and includes material constants B_n and C_n.

For a light source of 730 nm the refractive index of N-SF6 is 1.7892 and for 660 nm the refractive index is 1.7957. The pure transmittance of N-SF6 (10mm) varies in the VIS range between 0.820 at 400 nm and 0.993 at 700 nm [3].

For 730 nm the refractive index of F2 is 1.6112 and for 660 nm the refractive index is 1.6148. The pure transmittance of F2 (10mm) varies in the VIS range between 0.994 at 400 nm and 0.999 at 700 nm [3].

The three most commonly employed forms of refractive index couplers for surface plasmon resonance measuring devices are hemispheres or half cylinders, prisms, and truncated prisms (Figure 2.7). In the case of a single measurement point, the hemispherical shape offers the advantage that the light beam always strikes the surface of the body perpendicularly. However, this shape is not optimal for SPR imaging systems, as the spherical surface acts as a lens in this context. The prism shape depicted in the center is suited for SPR imaging. The angle of the prism can be selected to align with the SPR angle. One disadvantage of this approach is that a separate prism is then required for each angle. The angle of the prism can be selected so that the light beam strikes the entrance and exit surface perpendicularly, where reflections are minimized. However, the prisms angle can also be selected so that any reflections at the boundary surfaces are removed from the light path. The prism stub shown on the right facilitates handling of the prism but limits the usable angular range.

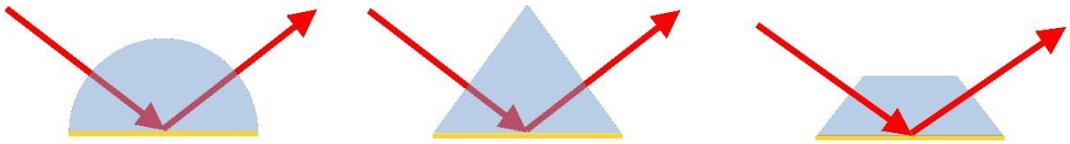

Figure 2.7: The three most common forms of refractive index couplers for SPR instruments are hemisphere, prism and truncated prism.

The research involved the use of different wavelengths. Additionally, the **prisms** were treated in various ways, including exposure to high temperatures, cleaning processes, recycling, and the application of references. Consequently, an anti-reflective coating was not applied to the entry and exit surfaces. Experiments done with water or water-based matrices were performed with prisms made of Schott F2 glass. Experiments done with oil-based matrices were performed with prisms made of Schott N-SF6 glass.

To operate the system as a sensor an easy exchange of the prism is mandatory. Therefore, a **prism mount** was developed which presses a flow cell onto the prism. The carrier frame also places the components in the center of the SPR instrument. The carrier frame is made from a fiber-reinforced, temperature-resistant PLA-based material using the Fused Layer Modelling (FLM) process. The material has a softening temperature of 115°C according to HDT/B and should therefore be sufficiently resistant for the application. The color is RAL 9017 Traffic Black with a matt finish to minimize reflections. The tensile strength of 65 MPa ensures that the geometry does not deform significantly during clamping. The material was printed on a Prusa MK4 printer at a temperature of 245°C. Component cooling was reduced to 50%. The print bed was heated to 60°C. To improve adhesion to the print bed, a thin layer of Magigoo 3D Print adhesive in the standard version was applied to the print bed. To prevent damage to the printer from the abrasive material, the standard nozzle was replaced with a hardened 0.4mm diameter NozzleX in E3D V6 format. Printed plastics tend to warp during cooling [4]. This can have serious effects on the component geometry if it occurs during the printing process or if there is a local wind draft during printing. To prevent this, the printer was enclosed. Fiber-reinforced plastics tend to absorb moisture during storage.

Excessive moisture in the material can cause issues during the printing process, such as the evaporation of water during extrusion and the formation of bubbles in the extruded material. To prevent this, the material was conditioned in an oven at 50°C for seven hours prior to printing. In addition, the air in the printing and storage chamber is kept as low as possible with a dehumidifier (UHU airmax UH52155). The extrusion width was set to 0.6 mm to ensure that the individual perimeters were better pressed into each other. Eight layers were set for the bottom and top. Four perimeters were chosen for the outer skin. The infill was made in a cubic pattern with a fill level of 50%. To enhance thread stability, brass press-in nuts were used instead of directly making threads in the plastic. To reduce potential sources of error, an aluminum version was manufactured for long-term measurements as plastic parts may creep under high pressure applied over extended periods. The components were anodized black to minimize reflections. All components have a specific tolerance. These tolerances can cancel each other out or add up, which may ultimately lead to a misplacement of the prism in terms of its positioning. For most applications, this misplacement should be insignificant. To ensure precise positioning of the prism, in case it is needed, the frame fixing it contains adjustment options (Figure 2.8).

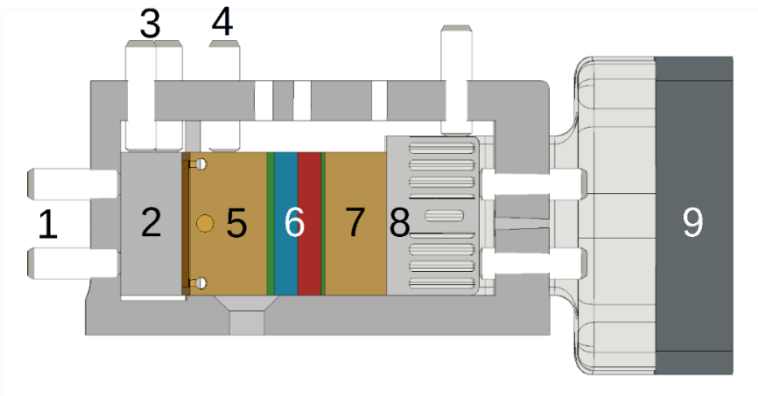

Figure 2.8: A cross section of a prism mount. Here the prism mount is equipped with one possible configuration, to show its options. The screws at the left side (1) can be used to adjust the tilt of the prism (2) along the light path and to place the gold surface at the center of the hinge. The three screws at the left side of the top (3) can be used to adjust the tilt of the prism and to fix the prism in its place. The screws at the middle of the top (4) are to fix the fluid cell (5). There are some more threads which can be used to fix optional components. The screws at the right side are used to couple components like a Peltier Element (6), a spacer (7) and a heat sink (8), which is equipped with a fan (9).

The screws at position 1 can be used to push the gold surface of the prism over the center of the axis of rotation. The two screws can also be used to tilt the prism. This allows it to be aligned exactly at right angles to the base. The screws at no. 3 can be used to fix the prism in place. However, they can also be used to tilt the prism in the direction of the legs. Tilting via the screws is made possible by a flexible base under the prism. For the tests with aqueous media, a 1 mm thick base made of styrene-butadiene rubber with a hardness of 65 Shore A was used. For the work with mineral oils, a silicone base with a hardness of 60 Shore A was used, as this is more resistant to the oils. This pad also serves as thermal insulation against the metal frame. Ball pressure screws without heads with flattened polyoxymethylene balls were used to fix the prism. The pressure balls of the screws can tilt by up to 9° and thus enable distortion-free clamping of the prisms. The flow cell described above is pressed against the prism from behind using a knurled screw of size M4 to DIN 464. If required, a Peltier element with heat sink can also be inserted between the knurled screw and the flow cell to control the temperature of the flow cell. The two screw types mentioned are made of burnished steel to minimize reflections.

The **flow cells**, optimized for homogeneous flow (Figure 2.9), were designed using Autodesk Inventor and manufactured from aluminum using Selective Laser Melting (SLM) on an EOS M100 3D printer.

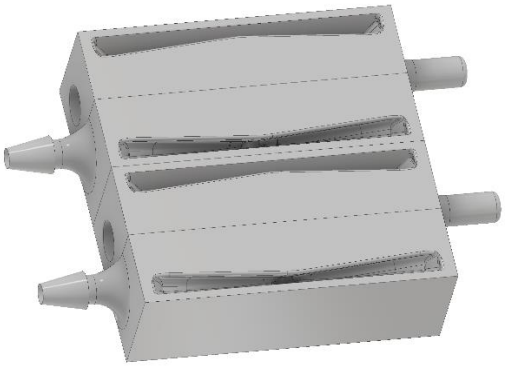

Figure 2.9: Two chamber flow cell, optimized for homogeneous flow.

The standard flow cells, which had no homogeneity optimization, were machined from a solid block of brass. Connections were made using threaded sockets with an M3 external thread. To distribute the analyte, a hole was drilled through the block for the inlet and outlet. For the supply line to the sensor surface, a series of holes were drilled from the surface to the inlet and outlet. Both types of flow cell have one or two cavities on their side for the insertion of a temperature sensor. The temperature was measured using a Honeywell PT1000. Both flow cells were sealed with a Wacker Semicosil gasket. The sealing was applied using a Dispenser (Musashi, Shotmini 200 Sx).

Sealing. A connection must be established between the SPR prism and the flow cell. As the flow cell or prism needs to be replaced at regular intervals, a detachable connection is advantageous. Consequently, silicone seals were applied either directly to the prism or to the flow cell, depending on the application. The seals were made from Silicon (Wacker, Semicosil). The seals were applied using a dispenser (Musashi Shotmini 200Sx) and an air pulse system (Musashi ML-805GX). A syringe barrel (Vieweg 801003) with a stopper plug (Techcon Systems 783-7100007), and a dosing needle (Vieweg F560087-1/4) were utilized in the dispenser. The syringe barrel is connected to the air pulse system with an adapter (Vieweg 560042A-SB-AL).

Tygon **tubes** were used to measure aqueous media. The LMT-55 model has a smooth, polished inner wall, which reduces the likelihood of matrix components adhering to the tube wall and distorting the measurement. The tube is transparent, allowing for quick and easy recognition of air bubbles. The material is resistant to most non-organic chemicals. It has low gas permeability, which prevents gas accumulation in the matrix. Tygon is a PVC-based material with a plasticizer that is free from phthalates. Its operating temperature range is from -5°C to 74°C. The material has a water absorption rate of 0.24% according to ASTM D570-98 [5].

For the measurements in aqueous samples, a Tygon LMT-55 tube (VWR VERN070534-11L-ND) with an inner diameter of 1.02 mm and an outer diameter of 2.72 mm was used. The small tube diameter and associated small sample volume are advantageous as the analytes used in this area are often very expensive. However, LMT-55 Tygon tubes should not be used for an oil-based matrix as they become hard after a short time. Instead, transparent polyurethane tubes from Sang-A were used. The hoses have a 2 mm inner diameter and a 3 mm outer diameter. A larger hose diameter offers the advantage of having more fluidic accessories available.

Silicone tubes turned out not to be suitable for aqueous or oil-based matrices. For aqueous samples, gas diffuses from the outside into the tubing and then into the liquid. For oils, the oil diffuses through the tubing to the outside and collects on the outer wall.

Accessories for fluidics with an internal diameter of 1 mm are very limited. To address this challenge, tubing olives with an M3 thread were fabricated. Each analyte was pumped using a separate micropump (Bartels MP6 piezoelectric double diaphragm pump), as no tap banks for 1 mm inner diameter tubing were available. To prevent liquid from being pumped into the wrong direction, a non-return valve (Bartels mp-cv) was installed after each pump.

Products from the medical technology sector were used for the hoses with an internal diameter of 2 mm. The connection between accessories and tubing was realized using full metal dosing needles (Vieweg 561345-13MM) with Luer-Lock connection. To switch between different analytes, a BraunB Discofix C 5-way valve bank (16608C) was used. BraunB COMBIFIX adaptors (5206642) were used to connect similar Luer-Lock connectors.

To store the samples during the measurements, a Carl Roth (AYC8.2) 250 mL wide-mouth amber glass jar with a GL55 (DIN 168) lid was used. A hole of 3.2 mm was drilled in the lid for the oil hose. The tube was inserted into the glass through the hole. The hose fits tightly with the lid, so the cap must be opened slightly to avoid negative pressure in the jar during pumping.

Due to the high viscosity of the oils used, the micropumps had problems transporting the media. If air bubbles got into the pump chamber, the micropumps often failed completely. The oils were therefore pumped using an Ismatec™ IPC peristaltic pump.

Bubble traps were designed for the project. Figure 2.10 a) illustrates a bubble separator manufactured via the polyjet 3D printing process. During the development process, the bubble trap was manufactured from VeroClear RGD810 material on a Stratasys Objet 500. As the printed plastic hose olives were found to be insufficiently robust, brass hose olives were screwed in. Furthermore, the olives were additionally sealed with a tube sealant (LiquiMoly 3808).

As soon as the development process was finished, the bubble separators were manufactured from metal in an EOS M100 printer. The increased stability made it possible to print the tube olives. A gas-permeable membrane (Infiltec 100297) (Figure 2.10 b) was inserted into the base (1) from above. The membrane with integrated sealing ring (2) is pressed downwards and to the side by a conical sieve (Infiltec 100386) (3), creating a tight seal in the seat. The sieve is in turn pressed downwards by an M12 grub screw to DIN 913 (4). A hole has been drilled in the screw to allow the gas to escape upwards through the screw. There is a baffle (5) plate in the chamber of the bubble separator to ensure that bubbles are not forced through the chamber at high pump speeds.

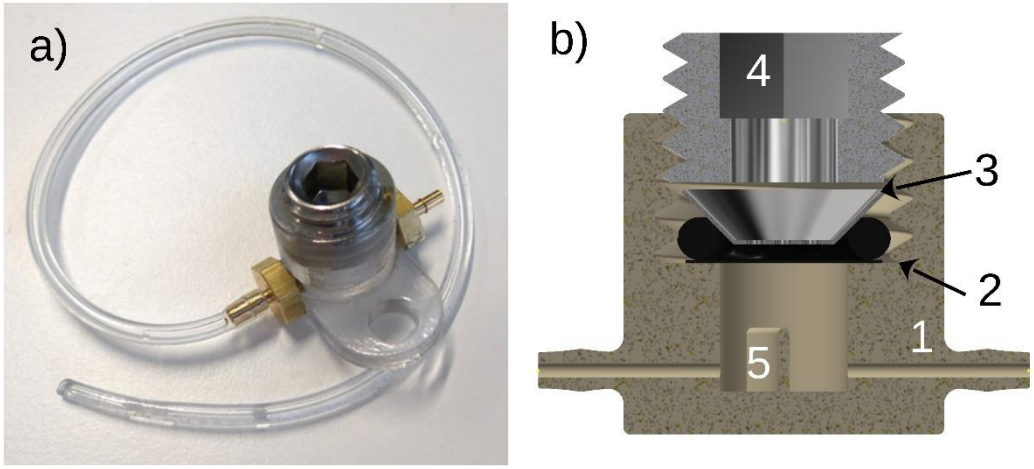

Figure 2.10: Home-made Bubble Trap, a) transparent, 3D-printed model of the home-made bubble trap, the transparent body allows for observation of bubbles inside the trap. b) half section sketch of the home-made bubble trap. It consists of a base (1), a membrane with sealing ring (2), a sieve (3), a modified grub screw (4) and a baffle plate (5).

The Bartels mp6 is an ultra-compact and lightweight **piezoelectric micropump** designed for microfluidic applications. It combines two piezo actuators in a miniaturized double diaphragm pump configuration, resulting in an ingeniously simple yet highly versatile design. When voltage is applied, the piezo ceramics deform, displacing the membranes and creating a pumping action that moves the fluid through the pump chamber and passive check valves.

The flow rate of the mp6 micropumps exhibits a linear dependency on the back pressure. At zero back pressure, the maximum flow rate is achieved, while at the maximum rated back pressure, the flow rate drops to zero. The mp6 micropumps are remarkably compact, measuring only 30 x 15 x 3.8 mm and weighing a mere 2 grams. They are constructed almost entirely from plastic, with polyphenylsulfone (PPSU) as the wetted material, providing good chemical compatibility. These micropumps are designed for low power consumption, typically around 50 mW, and can be operated from a battery source. They offer good operation temperature 0-70°C and can be sterilized by various methods, including autoclave, EtO, radiation, and alcohol.

Peristaltic pump. The Ismatec IPC 4 uses a planetary gear system to rotate a pump head containing 8 rollers. These rollers sequentially compress a flexible tube against a circular pump bed, creating a peristaltic pumping action. As one roller compresses the tubing, the preceding roller allows the tubing to re-expand, creating a continuous flow of fluid without exposing it to components other than the tubing material. The pump has 4 channels for simultaneous fluid flow. It can deliver flow rates from 0.0004 to 11 mL/min per channel, depending on the tubing size used. It can handle pressures up to 1.5 bar. The pump uses 2-stop tubing, which requires the purchase of tubing with pre-installed stoppers. These 2-stop tubings are expensive and limit the variety of tubing materials.

The Behr Labor-Technik PLP33 is a compact laboratory peristaltic pump. It features a continuously adjustable flow rate from 7 to 33 ml/min with its pre-installed tubing. The flow rate can be varied by using other tubing with different internal diameters. The pump design incorporates a rotor mechanism with two pressure rollers and four guide rollers. One of the key advantages of the PLP33 is its user-friendly design, which allows for easy maintenance and customization. Users can install their own tubing without the need for pre-installed stoppers, providing flexibility in adapting the pump to specific experimental requirements. The ability to use custom tubing is especially beneficial for oil-based analytes where standard Tygon tubing quickly becomes stiff.

Syringe pump. The new ERA Pump Systems Type-300 is a precision syringe pump designed for precise fluid delivery in laboratory and research settings. It uses a stepper motor-driven linear actuator to precisely control the movement of a syringe plunger, enabling highly accurate and reproducible fluid dispensing. The pump is capable of accepting a wide range of syringe sizes, typically from 1 mL to 60 mL, such as the BraunB 60ml syringe (PZN: 00570051) with a Luer connector. The Type 300 pump offers a wide range of flow rates, typically from microliters per hour to milliliters per minute, depending on the syringe size used. Syringe pumps such as the New ERA Type-300 offer several advantages over peristaltic pumps in certain applications. One key advantage is their superior accuracy and precision in fluid delivery, especially at very low flow rates. Another advantage of syringe pumps is their ability to deliver fluids without the pulsation inherent in peristaltic pumps due to their roller mechanism.

2.4 Light Source and Optical Components

LED Light Sources. When selecting a suitable LED, there are factors to consider in addition to the wavelength. Different LEDs have different efficiencies, which means that they convert different amounts of the consumed electrical energy into light. A lower efficiency consequently leads to a higher heat loss of the LED. The nominal value at which an LED is offered often deviates from the actual central wavelength (CWL) at the typical operating current. Furthermore, the CWL usually shifts with the operating current and temperature. In addition, in the vast majority of cases LEDs are fitted with a lens, resulting in different beam geometry characteristics depending on the LED and lens. A wide beam range usually has a larger area in the middle in which it emits with relatively homogeneous intensity. These LEDs therefore illuminate a certain area more homogeneously than LEDs with a very narrow beam angle. However, if a large distance between the LED and the collimating lens is necessary due to design requirements, a large proportion of the light of an LED with a broad beam, may be lost. In this case, an LED with a small beam angle would lead to higher system efficiency.

Various wavelengths were tested for use in a light source. A wide range of requirements have to be weighed up against each other. Figure 2.11 shows a simulation for Schott F2 glass with different wavelengths. The simulation illustrates how the SPR angle depends on the wavelength. However, it should also be noted that the wavelength is not the only parameter for the position of the reflection minimum. The minimum is also influenced by the refractive index of the glass used. When selecting the measurement angle, it is important to note that angles smaller than 45° are not practical for SPR imaging. In addition, the distortion of the image increases as the angle increases. Figure 2.11 therefore suggests that a long-wave light source would be preferable. However, this is limited by other factors. CMOS cameras have a wavelength-dependent quantum efficiency (QE). Unfortunately, the QE drops sharply in the near infrared range (NIR). Furthermore, it is very advantageous during development work if the light beam is visible. This makes design work easier and reduces the risk of injury.

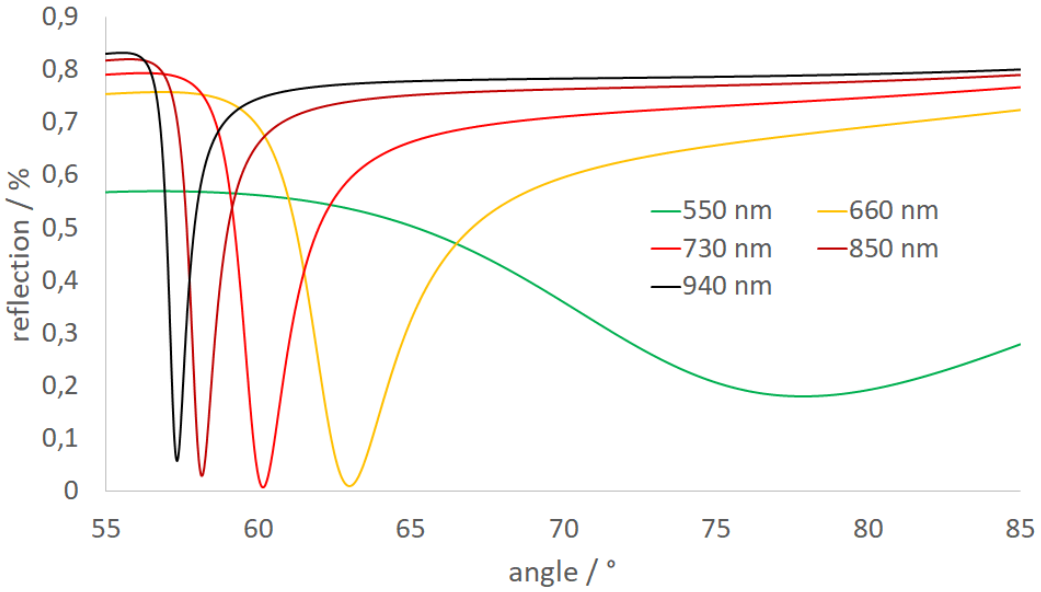

Figure 2.11: Simulated SPR-curve for Schott F2 glass, coated with a 1 nm chromium adhesive layer and a 50 nm gold layer. The analyte is water. Simulation was done with WinSpall software.

In addition to the factors that directly affect the SPR process, there are also other factors that influence manufacturability and cost. LEDs are not available immediately and inexpensively in every wavelength. It should also be noted that, in addition to the CWL, the Full Width at Half Maximum (FWHM) is also a decisive criterion for selection. There are LEDs that emit a very broad spectrum. In the visible spectrum (VIS), FWHMs with low two-digit values or over 100 nm are possible. In the infrared range, the Full Width at Half Maximum can be even greater. In contrast, UV LEDs with a FWHM of just 10 nm are available. From Figure 2.11 it becomes clear that a suitable LED should have the narrowest possible emission spectrum to optimize the SPR effect. As normal LEDs in the VIS spectrum is not available with a FWHM of 3 nm or less, it is obvious that the LED must be combined with a filter. One selection criterion is therefore the availability or at least the manufacturability of filters for the wavelength of the LED. Another filter to consider is the polarization filter. These can be produced in a wide variety of ways. The production method in turn affects the price, durability and robustness of the filter. The availability of polarizers for a specific wavelength must therefore also be taken into consideration.

Consequently, two wavelengths were defined for the experiments. The first wavelength, 660 nm, was chosen as it is readily available as a semiconductor laser and has been used frequently in the literature for SPR experiments. The second wavelength, 730 nm, was chosen as it is available as a high-power LED and is inexpensive. According to the simulation, 730 nm should offer better sensitivity than 660 nm. Moreover, the wavelength is visible to the human eye and CMOS cameras offer sufficient quantum efficiency at this wavelength. There are also strong absorption bands from water in the NIR and IR. As water is also present in the atmosphere and large parts of the beam path pass through the atmosphere, this can cause problems, particularly in the case of the reference instrument.

730 nm LED with 80° angle of radiation. The light sources used at the reference SPR-Imaging instrument were constructed with a 730 nm OSRAM Oslon SSL 80 GF CS8PM1.24-3S4S-1 LED. At its typical operating current of 350 mA and a Temperature of 25°C, the LED has a central wavelength (CWL) of 727 nm and an output power of 270 mw, with a typical luminous efficacy of 42%. The FWHM of the LED is 30 nm and the viewing angle is 80°.

730 nm LED with 150° angle of radiation. The light sources used at the miniaturized SPRi sensor were constructed with a 730 nm OSRAM Oslon SSL 150 GF CSHPM2.24 LED. At its typical operating current of 350 mA and a Temperature of 25°C, the LED has a central wavelength (CWL) of 727 nm and an output power of 270 mW, with a typical luminous efficacy of 42%. The FWHM of the LED is 30 nm and the viewing angle is 150°.

660 nm LED with 80° angle of radiation. The 660 nm light sources used at the reference SPR-Imaging instrument were constructed with an OSRAM Oslon SSL 80 LH CP7P-3T4T-1 LED. At its typical operating current of 350 mA and a Temperature of 25°C, the LED has a central wavelength (CWL) of 657 nm and an output power of 400 mW, with a typical luminous efficacy of 42%. The FWHM of the LED is 25 nm and the viewing angle is 80°.

Light source module. Setting up a dedicated, integrated light source for each new change to the light source setup would take an enormous amount of time and resources. It was therefore necessary to develop a modular system in which the individual components of the light source can be exchanged, adjusted and tested. A microbench system (30 mm optical Bench) turned out to be an ideal interface that enables simple exchange in both systems. Figure 2.12 shows an example of an SPR light source. The system consists of three 6 mm rods (LINOS G061211000) and one rod (LINOS G061241000), where the fourth rod has a scale for better positioning of the components within the system. In addition, the system has a rotary mount for rotating the polarization filter (LINOS G065058000) (11), a mounting plate for the wavelength filter (Thorlabs CP33/M) (10), an XY translating lens mount (Thorlabs CXY1) (9) for the collimating lens, and a centering mounting plate (LINOS G061025000) (5) for the light emitting diode. The light source system is built according to the instructions of Chapter 4.

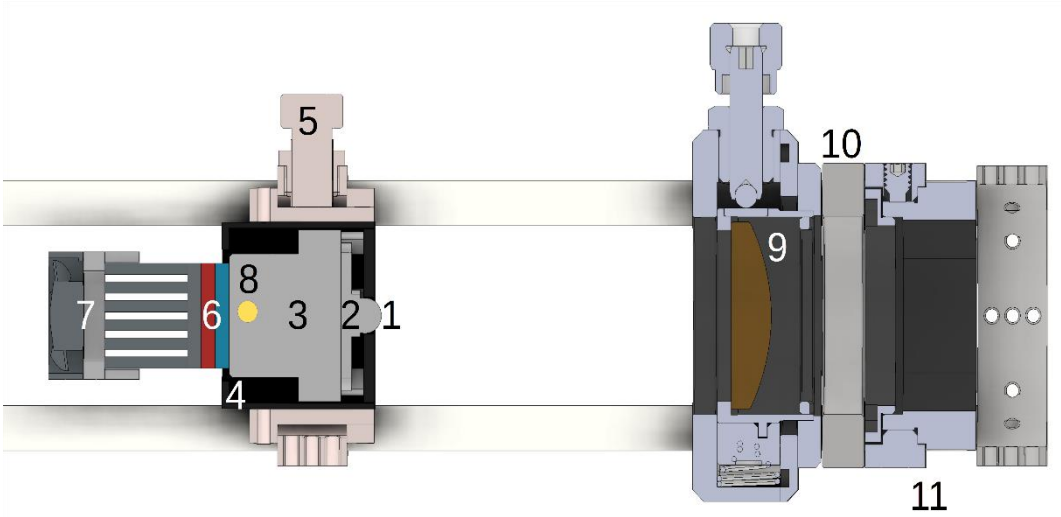

Figure 2.12: SPR-light-source. At the left side, there is a LED (1), soldered on a metal core PCB (2) that is glued to a heat sink (3). The heatsink is encapsulated at 25 mm diameter housing (4). The housing is mounted at a standard 30 mm x,y-translation stage from LINOS (5). The back of the heat sink is equipped with a Peltier element (6) that is cooled by a heat sink with a fan (7). The temperature of the heat sink (3) is measured by a PT1000 (8). At the right side are a lens at a standard 30 mm x-y translation mount (9), a wavelength filter mounted at a fixed cage plate (10) and a polarization filter mounted at a rotation mount (11), all from Thorlabs.

Integrated light source module. An integrated system can further improve the robustness and manageability of the light source. The technology readiness level was achieved with the development status shown in Chapter 4. Consequently, an integrated light source was developed (Figure 2.13).

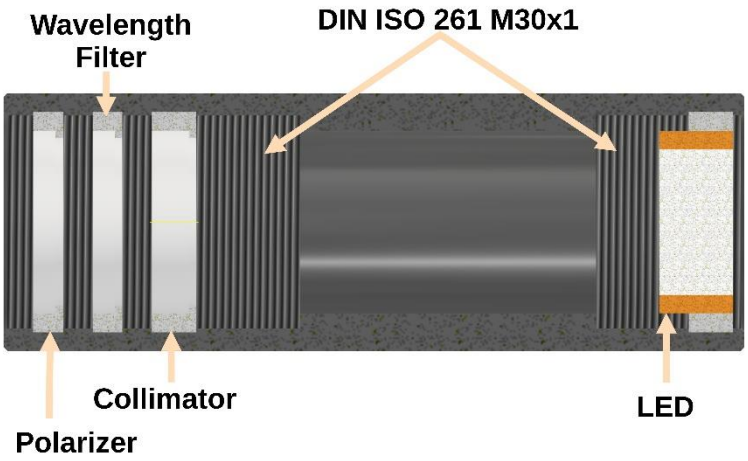

Figure 2.13: A black anodized aluminum tube with fine threads is used to position the components of the light source. Placing the components in a housing makes the light source less sensitive to environmental influences.

The maximum possible size for a mounting plate within the optical cage system is 35 mm. Consequently, the integrated light source was realized in a tube with an outer diameter of 35 mm. The components can be placed inside the tube using a fine thread with M30x1 according to DIN ISO 261. The pitch of one millimeter makes it easy to convert revolutions into distance. The tube acts as protection against dust and other contaminants. The tube is anodized black to minimize reflections. If required, a further reduction in reflections can be achieved by inserting a tube with an inwardly open diamond pattern between the collimating lens and the LED. The light source can be designed with active and passive cooling. Figure 2.13 shows a version with passive cooling. The LED is mounted on an aluminum cylinder, which in turn is thermally coupled to the tube via the thread. At low wattages, the LED can thus be operated with a corresponding warm-up phase without active cooling. The light source design presented in this chapter was utilized in chapter 7. For high resolution measurements it was combined with a temperature-controlled LED. For developing the miniaturized sensor, it was used with the passive cooled LED.

Temperature control unit for LED regulation. Temperature is a crucial factor, as it affects the output power of a LED at a specific driving current. It is therefore imperative that both sufficient heat dissipation and a stable temperature are ensured in terms of SPR sensing. Two types of heat transfer are of relevance for LEDs: conduction and convection. Conduction is the transfer of energy between atoms through direct contact of particles of matter. Convection is the motion of molecules in air or fluids. In LED systems, the heat sink is the most commonly utilized thermal management device. In the majority of cases, heat sinks for LEDs are constructed with metal fins to ensure effective heat flow. Additionally, thermal paste or tape is frequently applied between the heat sink and the LED housing to prevent the formation of air gaps and to ensure optimal thermal coupling and heat flow. In conjunction with an appropriate surface, the high thermal conductivity of the metal enables the transfer of heat from the semiconductor to the heat sink, which is then cooled by the ambient air. The capacity of a heat sink to transfer heat is contingent upon its material, geometry, and the overall heat transfer coefficient of the surface. Aluminum is typically employed because it is comparatively inexpensive in comparison to copper, has a lower weight, and is more readily molded into diverse geometries.

The two light sources previously described permit the LED to be replaced with minimal effort and in a relatively short time. In Figure 2.13, the holder for the LED module is constructed from aluminum. In the context of low operating currents, which are typical of SPR technology, passive heat sinks are capable of providing sufficient cooling for the LED. In this scenario, the temperature

of the LED exhibits a lag relative to the ambient temperature. This is an appropriate solution for measurements in the medium to low resolution range and for very short measurements. However, if the objective is to perform measurements at a very high resolution or over extended periods of time, it is necessary to stabilize the temperature of the LED. Figure 2.14 shows a cooled, integrated version of an LED-based light source module. It can be screwed into the light source shown in Figure 2.14 instead of the passively cooled LED.

In principle, there are two possible methods for printing fine threads. The highest resolution can be achieved using resin 3D printing, but the materials available there are either very brittle or relatively soft and have low temperature stability. As a result, there is a possibility that the thread will break during screwing. Stresses could also lead to breakage when inserting the cooling cylinder of the LED.

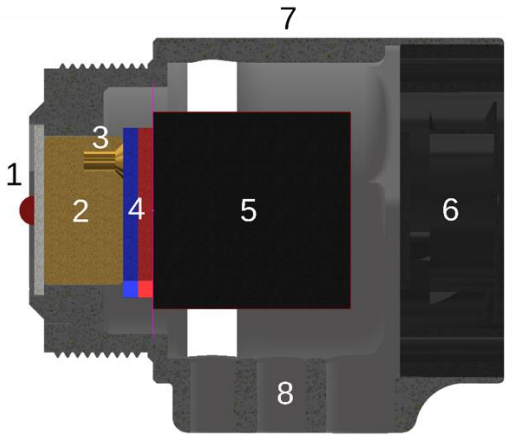

Figure 2.14: The light source XXX can be equipped with a temperature-controlled LED. The temperature-controlled LED module consists of an LED (1), a brass cylinder (2), a temperature sensor (3), a Peltier element (4), a heat sink (5), a fan (6), the housing (7) and the holders for the electrical supply cables (8).

The LED mounted on a starboard (2) was glued to a brass cylinder (3) with a diameter of 15 mm. An Arctic Silver thermally conductive adhesive was used for bonding. The thermally conductive adhesive has a thermal conductivity coefficient of around 7.5 W/mK and therefore bonds the LED excellently to the brass cylinder. The brass cylinder was connected with thermally conductive adhesive to a Peltier element (4). A Peltier element (QuickCool QC-17-1.0-3.9M) was used here. A heat sink (5) was glued to the back for heat dissipation. To optimize the assembly, an axial fan (6) (Sunon, MF25101V21000UA99) was inserted into the housing from behind. The integrated temperature control unit presented in this chapter was utilized in chapter 7.

Optical lenses can experience various types of errors that affect performance and image quality. The most common errors are spherical and chromatic aberration. However, since only monochromatic light sources are used here, chromatic aberration is not a concern. Aspherical lenses were used for the light source to minimize the disturbing effects caused by spherical aberration. Aspheric lenses have a unique geometric feature where the radius of curvature changes with distance from the optical axis, unlike a sphere which has a constant radius. This shape allows for improved optical performance compared to standard spherical surfaces. Anti-reflection (AR) coating vastly improves the efficiency of lenses by increasing transmission, enhancing contrast, and eliminating ghost images. Anti reflection coatings only work within a specified wavelength range. While the coating can significantly improve the performance of an optical system, using the coating at wavelengths outside the design wavelength range could potentially decrease the performance

of the system. Especially low-light systems incorporate coated optics to allow for efficient use of light. Within this work different lenses from Edmund Optics were used for experiments. At the beginning of the work lenses without AR coating were used, since there was no final specification for the wavelength. Later, the wavelengths 660 nm and 730 nm were specified. From then on, the BBAR (600-1000 nm) coating offered by Edmund Optics was used, which has a minimum reflectance of only 0.1% at 660 nm.

The light source used for the reference measuring instrument employed an aspherical NIR AR coated Edmund Optics #66-024 lens with a diameter of 25 mm and a focal length of 40 mm. The lenses have a numerical aperture of NA 0.31 and a free aperture of 21.5mm. The center thickness of the lens is 4.8mm and the edge thickness is 1mm. The effective focal length of the lens is 40mm and the back focal length is 37.09mm, both at a wavelength of 587.6nm. The material of the lens is Zeonex E48R.

For the measurements described in chapters 3 to 6, PMMA **polarizing filters** from Edmund Optics were utilized. These filters are coated with a polarizing film and have an extinction ratio of 9000:1 within the application range of 400 nm to 700 nm. The #85-919 filters from Edmund Optics also work well at 730 nm, although the extinction ratio is slightly worse at this wavelength. A benefit of these filters is that they are relatively insensitive to handling. For measurements described in chapter 7, only a few changes were made to the light sources. The performance was optimized and the #20-234 wire-grid polarizers from Edmund Optics were used. Within the specified wavelength range of 400 nm to 1200 nm an extinction ratio of 1415:1 is achieved by these filters. Additionally, these filters can also be used for experiments at higher wavelengths. One significant drawback of these polarizers is their high sensitivity to touch, which makes them prone to damage if not handled with care.

During the work, standard optical filters with half-widths greater than 10nm were the only ones available. Therefore, a **low pass** and a **high pass filter** were combined. Here a long pass filter with a blocking range of 200 nm to 705 nm and a transmission range of 735 nm to 1650 nm (Edmund Optics #86-068) and a short pass filter with a blocking range of 740 nm to 1090 nm and a transmission range of 400 nm to 710 nm (Edmund Optics #86-103) were combined. Both Filters have a cutoff wavelength of 725 nm. Theoretically the combination should work, however the filters have a tolerance of ± 1 nm. That means the combination could lead to a filter that is blocking everything or to a filter with a high FWHM. Although this combination worked well, a customized filter was ordered with a CWL of 728.5 nm, a maximum transmission of 50%, a half-width of 2.8 nm, and a blocking of OD7. The custom-made filter has a large AOI range of 0° to 7°. Another custom-made filter was obtained from RGB-Photonics for the wavelength of 660 nm.

A Liquid Crystal Tunable Filter (Thorlabs KURIOS-WB1/M) was tested for its suitability for a wavelength scan SPR device. However, it was found that the filter is not stable at several points in the spectrum and its CWL dithers. This approach was therefore discontinued. For experiments described in Chapter 3 and 4 the custom made 660 nm filter was used. The setup used for the measurements described in Chapter 5 and 6 used a combination of a short and long pass filter and for the work described in Chapter 7 the custom made 728,5 nm filter was used.

The **laser light source** was an RGB Lasersystems miniLas semiconductor laser, with a nominal wavelength of 660 nm and a maximum output power of 75 mW. The laser was supplied with an optional adapter for the 16 mm LINOS nanobench. To align the laser centrally and parallel to the microbench, a Kinematic mount (Thorlabs KC1-S/M) was used. The connection between the 16 mm nanobench and the kinematic mount was established utilizing a Thorlabs SP02 cage plate, which

features a 16 mm nanobench mount and an internal SM05 thread. The laser was connected to the SP02 cage plate via four rods (LINOS G050-211-000). An SM1A6 adapter was inserted into the kinematic mount, which has an external SM1 thread and an internal SM05 thread. The connection between the SM1A6 adapter and the SP02 adapter is made with an SM05T2 coupler.

Semiconductor lasers typically emit a narrow and collimated beam. For SPR-Imaging, it is therefore necessary to widen the beam. A **beam expander** is an appropriate device for this purpose. Beam expanders are frequently employed in interferometry, remote sensing, laser processing of materials and laser scanning. They permit the entry of collimated light into the system and emit a collimated light beam with a larger diameter. There are numerous prefabricated beam expanders available for purchase. However, the requirement for this system was that it should fit into a 30 mm optical bench and be as short as possible. Therefore, a special beam expander was constructed for the experiment. There are two possible variants for constructing a beam expander: one according to Keppler and the other according to Galilei. The Galilei version was chosen to keep the overall length as short as possible. The use of lenses with a flat surface (e.g., plano-convex or plano-concave lenses) instead of lenses curved on both sides results in a superior wavefront quality. In a Galilean design with lenses that are flat on one side, the wavefront quality improves when the curved surface is aligned in the direction of the incident beam, as the spherical aberration is compensated. However, it should be noted that reflections from the lense surface can damage semiconductor lasers. Therefore, it is advisable to use a lens with an anti-reflective coating.

The entrance lens is a mounted plano-concave lens manufactured from N-BK7 glass from LINOS (G052-301-322). The lens has a focal length of -3 mm, an optical diameter of 3 mm, and a free aperture of 2.5 mm. The center thickness is 0.5 mm, while the edge thickness is 1.6 mm. The outer diameter of the mount is 16 mm, rendering it suitable for mounting in the LINOS Nanobench. An adapter (G050-309-000) was employed to install the lens within the Microbench system. To minimize the reflection of light from the lens back into the laser, the lens is provided with a broadband anti-reflection coating ARB 2 VIS. The exit lens is a mounted plano-convex lens manufactured from N-BK7 glass from LINOS (G063-045-00). The lens has a focal length of 60 mm and an optical diameter of 22.4 mm. The lens has a free aperture of 21.4 mm. The center thickness is 4 mm, while the edge thickness is 2 mm. The outer diameter of the mount is 25 mm, rendering it suitable for mounting in the LINOS Microbench. The lenses were centered in the microbench using Centering Mounting Plates (LINOS G061-025-000). The position along the optical axis was adjusted by moving the centering mounting plates. The beam diameter of the beam expander was adjusted using an alignment plate (LINOS G061680000). The alignment plate was placed 30 mm and 3000 mm behind the beam expander. A twenty-fold magnification for the beam expander by an optical length of 57 mm could be achieved. This is sufficient to illuminate the area of the SPR sensor.

2.5 Signal Acquisition

Objectives. Imaging lenses play a crucial role in capturing high-quality images and their complexity can make decision-making challenging. When choosing an imaging lens, one must encounter trade-offs between different parameters. Fixed focal length lenses, are commonly used in machine vision applications. These lenses have a single focal length, which remains constant. The aperture size influences the amount of light that reaches the camera sensor. Another important value is the working distance, which is the distance from the front end of a lens system to the object under

inspection. As the lenses are used within a 30 mm or 40 mm optical bench system, their diameter is also important.

Three types of **lenses** were primarily used for the measuring instruments in this work. The Edmund Optics 16mm C VIS-NIR Series lens (#67-714) and the 25mm C VIS-NIR Series lens (#67-715), which were specially developed for the infrared range were used for the cameras with a sensor diagonal smaller than 1" while an Edmund Optics #86572 with a focal length of 25 mm was used for cameras with a sensor of 1" and larger.

To be able to analyze the beam of a light source without the influence of an optical system, a camera sensor without a housing and without a lens was developed. This is crucial, as housed cameras in most cases contain an additional cover glass in front of the sensor chip. When lasers are used, this cover glass can cause both reflections and interference. The free structure of the board level camera also makes it possible to place the sensor chip in close vincinity to the SPR element. The sensor used here was a camera from XIMEA with a CMOSIS CMV4000 chip. This sensor chip is also used in commercially available beam profilers such as the Cinogy CinCam CMOS Nano.

Another decisive factor for use in the SPR system was that the board level sensor can be mounted within a 30 mm cage system. The square design of the sensor also enables symmetrical beam analysis. The mount for the board level camera sensor was milled from aluminum. On the camera side, the mount has four spacers that keep the electronics at a safe distance from the conductive mounting plate. The spacers also ensure that the sensor chip can be mounted parallel to the mounting plate. A thermal pad is installed between the camera and the mounting plate to cool the sensor. The TP-3 thermal pad from Arctic used here has a hardness of 55 Shore OO (DIN ISO 7619-1) and a volume resistance of $2.69*10^{12}$ Ω/cm. The camera is connected via a USB3-Vision interface. The mount for the board level version of the XIMEA CMV4000 camera was used for recording the pictures without objective lens to achieve the results as discussed in Chapter 3 and 4.

Figure 2.15 illustrates an exemplar of the 3D-printed camera adapter for a Flir Blackfly camera. The camera adapters for the other cameras were similarly designed and manufactured. The adapter depicted here enables the camera to be mounted in a 40 mm optical bench system. Components for an optical bench system with this size are available from Newport. The adapter was printed with a Prusa MK4. The material utilized is Extrudr GreenTEC PRO Carbon. Press-in nuts (Ruthex GE-M4Sx04-1) are embedded in the sides to secure the mount to the bars of the optical bench system. These are installed using a soldering iron and a melting aid (Ruthex LOE-SET-011).

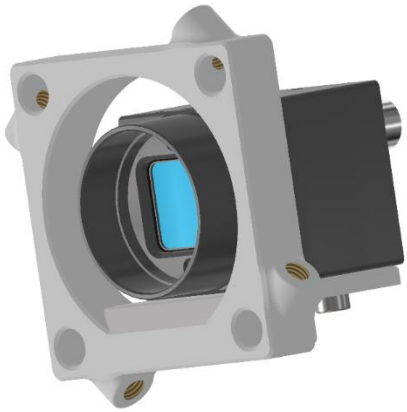

Figure 2.15: Flir BlackFly Camera with a 3D printed 40mm optical bench adapter.

The design shown here can be adapted for other optics bench sizes and camera interfaces. Within the scope of the doctoral thesis, 60 mm and 100 mm optical bench systems were also used.

Camera Interface. There are many different camera interfaces on the market, which all have advantages and disadvantages. For small smart sensor devices like an integrated SPR-sensor an interface that requires a large capture board will not be suitable. Nevertheless, one can take advantage of a high data transfer rate and a small and common interface as *e.g.* known from the USB3 interface. USB3 interfaces are presently even in the smallest stick personal computers available which makes them attractive for integrated devices. Moreover, USB3 Vision cameras can easily be integrated into LabVIEW software because of the NI-IMAQdx driver and GenICam, which is a standardized interface. It is also very easy to switch between different USB3 Vision cameras from different manufacturers since they all do support the same software interface.

The **camera** with which the project started was a CMOSIS CMV4000 camera. The camera was chosen because it is available as a board level camera and has a relatively large chip measuring 11.27 mm x 11.27 mm. The board level version of the camera has a board that is only 26 mm x 26 mm in size and can therefore be easily placed in a 30 mm optics bench. The camera has a frame rate of 90 fps and a resolution of 4.2 megapixels. The resulting data rate was critical at the start of the project, as computers with a correspondingly fast USB 3 port were not widely available. The camera needed its own PCI-USB card to ensure that the USB port was fast enough. The readout noise of the camera is 13 e^-. The exposure time can be varied between 26 µs and 1 s. The signal to noise ratio is 41 dB. Due to its square design, the camera could also be used as an excellent beam profiler. The camera's 10 bits enable an intensity resolution of 1024 levels.

Point Grey Cameleon3 - CM3-U3-28S4M-CS, CCD camera. A CCD camera was tested for comparison purposes. Unfortunately, the camera chip was somewhat smaller, making it less suitable for use as a beam profiler. The advantages of the camera chosen here were a higher bit resolution of 12 bit. It also had a lower noise level of only 10.48 e^- and a higher dynamic range of 59.96 dB. The Sony ICX818 built into the camera has a resolution of 2.8 megapixels and a frame rate of 13 fps. The exposure time can be varied between 64 µs and 31.9 s. The camera's 12 bits enable an intensity resolution of 4096 levels. This represents an improvement by a factor of four compared to the previously mentioned 10-bit version.

XIMEA MU9PM-MH, subminiature CMOS camera. To achieve the goal of miniaturization, the particularly small MU9PM-MH camera from Ximea with a size of 15 mm x 15 mm was tested. The camera has a resolution of 5 megapixels and a bit depth of 12-bits. The signal-to-noise ratio of the camera is 38 dB and the dynamic range is 59 dB. The camera delivers 5 fps and has a particularly low power consumption of just 0.76 W. The image sensor has an area of 5.70 mm x 4.28 mm. The board level version of the camera is even smaller and measures just 13 mm x 13 mm. The board level version is therefore small enough to be mounted in a 16 mm nanobench system from Linos. The image sensor has an area of 5.70 mm x 4.28 mm.

Imaging Solution Group Allegro LW-AL-IMX178M-USB-C. The Imaging Solution Group Allegro camera with a BI-CMOS chip from Sony (IMX178) is a significant improvement in the field of low-cost industrial cameras. It was the first compact industrial camera with a 14-bit sensor. The sensor has 6.3 megapixels and a sensor area of 7.37 mm x 4.92 mm. The camera supports USB3 Vision. In order to be able to use the camera in a 30 mm optical bench system, the housing was removed, and the circuit boards mounted in a holder. After the acquisition of Imaging Solution Group by JADAK, the camera is no longer available.

Flir BFS-U3-63S4M-C, BI-CMOS Camera. The Flir Blackfly S camera with a BI-CMOS chip from Sony (IMX178) is a low-cost industrial camera. It is the only compact industrial camera with a 14-bit ADC output which was available at this time. There are other cameras with a Sony IMX178, however currently the only offer a 12-bit output. The sensor has 6.3 megapixels and a sensor area of 7.37 mm x 4.92 mm. The frame rate is 59 fps and the exposure time can be varied between 8 µs and 30 seconds. The camera interface is USB 3.1 and the power consumption is 3 watts. The camera supports USB3 Vision. The dark noise is 3.2 e^-, the signal-to-noise ratio is 41.52 dB and the dynamic range is 73.33 dB. The quantum efficiency at 730 nm is around 40%. A board level version of the camera was announced but was not available during the work due to the acquisition of Flir by Teledyne. To allow the camera to be used in an integrated compact sensor without a lens, the housing was removed, and the circuit boards mounted in an open holder.

The **pco.edge 4.2 camera** has an internal temperature control that constantly regulates the temperature of the camera to 0°C. The resolution of the camera is 4.2 megapixels. The frame rate is 40 fps. The bit depth of the camera is 16-bit. The quantum efficiency at 730 nm is around 60%. The size of the sensor is 13.31 mm x 13.31 mm. Particularly outstanding is the low dark current of the camera, which is less than 0.3e^-. However, the edge 4.2 is not an industrial camera but a scientific camera. Accordingly, its price is significantly higher. The installation space of the camera is also larger, and it does not support USB3 Vision. Due to its size of 76 mm x 60 mm, it cannot be mounted in a commercially available optical bench. Therefore, a custom 100 mm optics bench based on 8 mm thick rods was designed for this camera. The camera's 16 bits enable an intensity resolution of 65536 levels. This represents an improvement by a factor of four compared to the previously mentioned 14-bit version.

The XIMEA CMV400 was used for the work in chapters 3 and 4. The XIMEA MU9PM-MH was used for the work in chapter 7, but it showed no benefit over the Flir Camera. ISG Allegro was used for the work in chapters 4. The Flir Black Fly was used for the work in chapters 3 and 7. PCO Edge 4.2 was used for the work in chapters 4, 5, 6 and 7.

Table 2.2: Selection of cameras tested in this work.

Manufacturer	Type	Sensor Size in mm	bit	Resolution	Pixel size	Frame rate	QE	Dynamic range (dB)
XIMEA	CMV 4000	11.27x11.27	10	2048 × 2048	5.5 µm	90 fps	50% @550 nm	60
Point Grey	Cameleon3 CM3-U3-28S4M-CS	7.11x5.34	12	1928 x 1448	3.69 µm	13 fps	76% @525 nm	59.96
XIMEA	MU9PM-MH	5.70x4.28	12	2592 x 1944	2.2 µm	5 fps	-	60
Imaging Solution Group	Allegro LW-AL IMX178M-USB-C	7.37x4.92	14	3072 x 2048	2.4 µm	60 fps	81% ~530 nm	41.6
Flir	Black Fly, BFS-U3-63S4M-C	7.37x4.92	14	3072 x 2048	2.4 µm	60 fps	81% ~530 nm	41.6
PCO	pco.edge 4.2	13.31x13.31	16	2048 x 2048	6.5 µm	40 fps	82% ~590 nm	91.5

2.6 Electronics

Temperature control. To be able to regulate the temperature of the flow cell and the LED, both components were fitted with a Peltier element. The regulation was carried out using a Quick-Cool QC-PC-CO-CH1 Peltier controller. The controller detects the temperature via an NTC 10KΩ sensor. To be able to set the controller more precisely, the QC-PC-DCH1 display was used instead of the supplied potentiometer. The driver has a maximum output current of 20A. QuickCool QC-17-1.0-3.9M Peltier elements were used to control the temperature of the LEDs. The single stage elements have a compact design of 12 mm x 12 mm x 3.6 mm. Their maximum heat output is 4.9 W. The maximum operating current is 3.9 A, and the rated voltage is 1.9 V. The maximum temperature difference that can be produced by the Peltier effect is 71 K. As the Peltier is only used to keep the operating temperature of the LED constant, the power draw during operation is much lower than the potential power. However, the size of the Peltier has been chosen to ensure a stable adhesive bond between the LED, the Peltier and the heat sink. Arctic Silver's two-component thermally conductive adhesive was utilized to connect the components in the cooling line of the light source. The adhesive has a good thermal conductivity of 7.5 W/mK. QuickCool QC-31-1.4-8.5AS Peltier elements were used to control the temperature of the flow cell. The single stage elements have a size of 20 mm x 20 mm x 3.4 mm. Their maximum heat output is 17.8 W. The maximum operating current is 8.7 A, and the rated voltage is 3.5 V. The maximum temperature difference that can be produced by the Peltier effect is 71 K. As the Peltier is only used to keep the operating temperature of the flow cell constant, the power draw during operation is much lower than the potential power. In certain experiments, the temperature of the flow cell was deliberately modified. The flow cell could be cooled by a maximum of 10K below room temperature. The limiting factor in this case was the heat sink of the Peltier element. However, this was not enlarged as there was no need for major temperature adjustments. Furthermore, lower temperatures would eventually result in temperatures below the dew point.

As the holder for the SPR sensor element is constrained by the rotation of the optical wings around the central joint, resulting in a limited installation space. Consequently, it is not possible to fit a large standard heat sink with a fan in this location. Therefore, a separate heat sink was developed for the Peltier element (Figure 2.16).

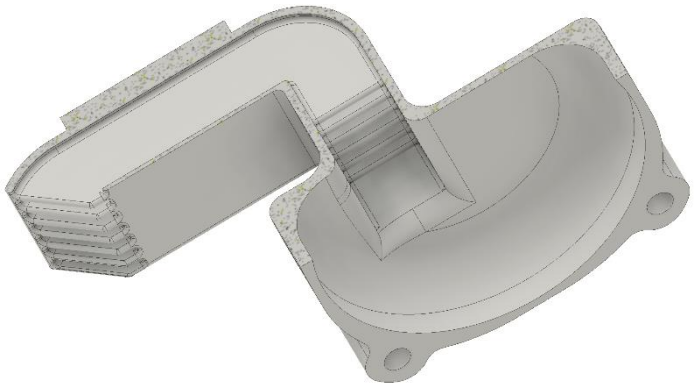

Figure 2.16: Half section of the SPR flow cell heat sink. The aluminum heat sink is manufactured using SLM 3D printing. In contrast to classic heat sinks, this heat sink integrates an air conduction system and a mount for a fan.

In a classic heat sink, the air between the cooling fins is heated and then rises, creating natural convection. In the event of an increased cooling requirement, a fan is installed on the heat sink fins to force the air through the fins of the heat sink. This results in the phenomenon of forced convection, which significantly increases the cooling capacity of the heat sink. Due to the limited installation space in the prism mount, only a small heat sink can be installed, which precludes the use of natural convection to sufficiently cool the Peltier element. The flow cell is pressed against the prism from behind, preventing the installation of a fan between the heat sink and the pressure screw. The heat sink is too small for direct side mounting of a fan, and there is also insufficient space next to the heat sink for a fan to be installed. Moreover, it is essential that the supply or exhaust air of the fan does not affect the SPR prism. In contrast to a conventional heat sink, which features open fins on three sides, the newly developed version exhibits a distinct configuration, with only two sides of the fins remaining open. This results in the formation of a flow channel that is only slightly extended on one side. However, the short extension has been slightly angled so that the airflow points away from the prism. On the opposite side, the flow channel has been extended to such an extent that it reaches behind the prism mount, where a fan is then mounted. The heat sink was printed with a metal 3D-printer. The support surface for the Peltier element was smoothed using a milling machine. The threads were cut using a bench drill.

USB connection. Selecting the appropriate cable is crucial when dealing with USB cameras that require high data throughput. USB 3.0 (SuperSpeed) provides a much higher data rate than its predecessor, USB 2.0, with a maximum bandwidth of up to 4 Gbit/s. This allows for the transfer of image data with higher resolutions, frame rates, and color depths. It is recommended to use a certified cable to ensure reliable and stable data transfer at high speeds. The higher speed of the cable can facilitate the capture of high-resolution images and videos in real-time, which is crucial for sensory applications. It is important to note that an inferior cable may lead to unexpected disconnections between the camera and the host computer, and one that does not meet the required specifications may reduce the maximum data transfer rate. At the beginning of this work, sufficiently fast USB3 connections were so rare that the XIMEA cameras used at the time were offered with USB3 PCI-e interface cards. Accordingly, no sufficiently fast infrastructure components were available at the time. The camera was therefore always connected directly to the computer in order to avoid connection interruptions. With the expansion of the USB3 standard, significantly faster components became available. Stable operation of the USB3 Vision cameras at full data rate was only made by the USB3.2 Gen2 standard on a HUB. This achieves twice the speed, meaning that there is still sufficient bandwidth for the camera even though other devices are being operated on the USB hub. While the standard USB3.0 connection can only provide 0.9 A, the maximum current with standard USB3.2 is already 3 A. Instead of 4.5 watts, the devices on a USB3.2 Gen2 hub can therefore consume 15 watts. If more power was required on a USB3.0 hub, an external power supply unit was needed. This can lead to potential differences and therefore to interference. Especially when connecting and disconnecting, this can lead to sparking and thus to connection interruptions. Selecting the appropriate cross-section for a USB cable is critical as it directly affects the cable's performance and efficiency. A cross-section that is sufficiently large ensures that there is enough power to operate the connected device. Choosing a cable that is too thin can result in insufficient power delivery. A thin cross-section can also result in higher voltage loss, which is caused by the electrical resistance generated by the wire. This can negatively impact the performance of the connected device by reducing the voltage level that reaches the end of the cable. Additionally, a thin cross-section can increase damping, which is a measure of the loss of signal strength along the length of the cable. The cross-section of the USB cable wires is usually specified in AWG. The abbreviation AWG stands for "American Wire Gauge", a coding system for

wire diameters that is mainly used in North America. This coding has gradually become established worldwide.

LED current source. The measured variable of an intensity-based SPR system is the intensity of the light reflected by the prism. How much light an LED emits depends on the operating current. If an LED was connected directly to a voltage source, it would heat up during operation and become increasingly conductive over time. This would increase the operating current and therefore also the temperature. This would ultimately result in the LED burning out or at least in a constantly changing emission. For this reason, LEDs are operated from a current source instead of a voltage source. All normal plug-in power supplies are designed as switching power supplies. Switching power supplies cause noise because they switch the voltage on and off in rapid succession. This clocking ultimately generates the noise of these power supply units. If the LED supply is noisy, the luminous flux emitted by the LED will also be noisy. To avoid such noise, a Keithley SMU 2636B was used to supply the LED. With an output current of 10 mA, the device has a peak-peak noise of 200 nA. The noise is therefore 1/50000 of the output current. A camera with a 14-bit sensor chip can only resolve 16384 intensity levels. The noise of the light source driver is therefore lower than the noise of the detector. In addition, the high-precision display of the output voltage makes it possible to assess the operating status of the LED. The user can therefore wait until the LED has stabilized and then start his measurements.

2.7 Data Processing

Although the USB3Vision standard enables a high data transfer rate, it can act as a limiting factor in some situations. The limitation can vary depending on the camera. For example, some cameras do not achieve the highest possible specified frame rate at full bit depth and full resolution. A reduction of the bit depth is excluded in SPR technology, as this is the factor that determines the ROI resolution. A reduction of the lateral resolution is possible in some cases, but not desirable in all cases. An alternative approach to reducing the data rate while maintaining the same resolution and bit depth is to select a specific area of the camera image. This procedure is referred to as Region of Interest (ROI) or Area of Interest (AOI). To avoid confusion with the selection of regions of interest in the SPR software, it is referred to here as AOI.

The GeniCam standard enables the user to select an image area and only transfer this to the camera. In some camera-lens combinations, the field of view (FoV) does not match the sensor area or is significantly larger than the sensor area. In these cases, all areas outside the sensor area generate unnecessary ballast that reduces the frame rate. In other constellations, the sensor area may correspond to the field of view (FoV) or be smaller, but the region of interest (ROI) may be in a significantly smaller area. In such cases, it can be beneficial to define an area of interest (AOI) on the camera in order to maintain the required data rate as low as possible, thus achieving the highest possible frame rate. A high frame rate has the advantage that more images can be generated in a shorter period of time.

If a large number of images were taken within a certain period of time, it is possible to combine several images into an average value. This can be useful for certain noise sources or if a certain response time is required. In these cases, it may be advisable to increase the exposure time of the camera and reduce the intensity of the light source in return. In the case of a large number of images with a high memory requirement, memory problems may also occur in the data processing system at a later stage. In this case, reducing the AOI can also help.

In chapter five, the AOI of the camera was limited to the most sensitive area of the sensor to determine the maximum RIU resolution.

The data was recorded using home-made software. The software was designed and created in cooperation with various students and employees of the Sensorik-ApplikationsZentrum of the OTH Regensburg. The functions and the function sequence, as well as the GUI functionality were drafted by the author. The LabVIEW code and the LabVIEW code structure were primarily developed by Carina Roth. The linear stage is initialized at the start of a measurement. To do this, the COM port to which the linear table is connected is selected. Then select "Connect Linear Table" and "Motor On". The table can now be calibrated with "Calibrate Start". The movement of the linear table is displayed in a yellow bar at the bottom of the screen. The display can be switched between angle and position in mm. After calibration, the table can be moved either in relative steps in degrees or mm. Alternatively, the table can also be moved directly to absolute positions, each in degrees or mm (Figure 2.17).

The conversion from mm to degrees depends on the position of the corner posts. The position can be entered under the settings menu item. This only needs to be done if the post position is changed.

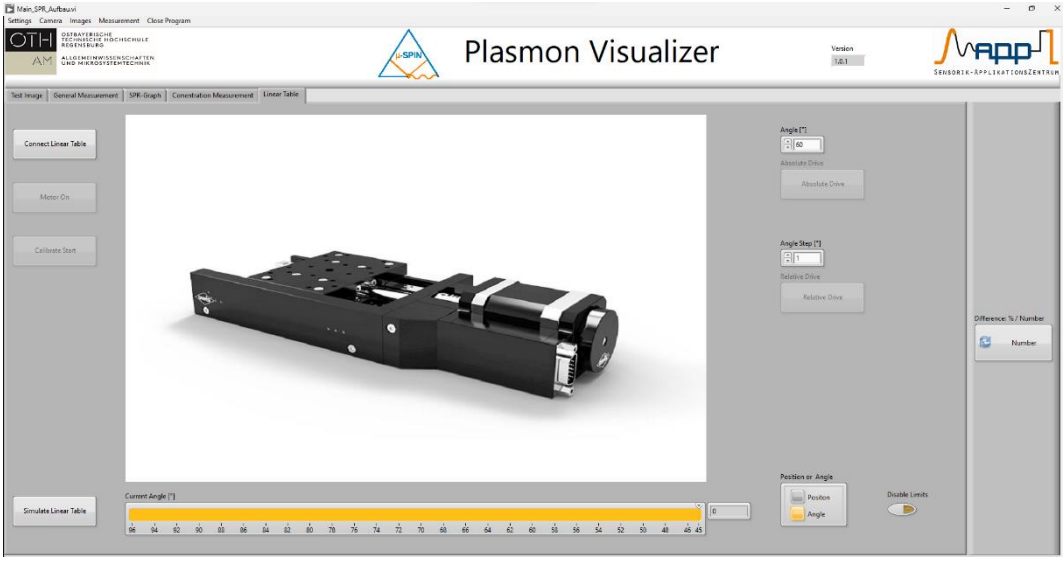

Figure 2.17: Screenshot of the SPR-measurement software.

Calibration of the table can also be skipped. In this case, however, a warning message appears before each movement or movement sequence, indicating that the table is not calibrated. The camera image can be displayed under the "Test Image" tab. The image is displayed on the left-hand side of the screen in the format transmitted by the camera. Alternatively, a false color display can also be selected. This makes it easier to recognize differences in brightness, as with a beam profiler. A cross-section of the image is also displayed on the right-hand side of the screen, as with a beam profiler. The location is shown on the x-axis and the intensity on the y-axis.

The software distinguishes between two measurement modes, mode one is the creation of an SPR curve, mode two is the continuous measurement of the reflectivity. Usually, an SPR curve is always recorded first to characterize the system and to determine the optimum angle for a measurement. The recorded SPR curves are displayed in the "SPR graph" tab. The values of the continuous measurement are displayed in the "Concentration Measurement" tab. The current measurement is also always displayed in the "General Measurement" tab. This tab also shows the image captured by the camera and a false color image that shows either the difference between the current image

and the first image or the previous image. This view makes it easier to identify regions in which changes occur.

The software contains numerous measurement options that can be helpful in various measurement applications and tasks. As the list of all options and their possible application scenarios is very exhaustive, it is not included here. Instead, the procedure of a standard measurement, as it was frequently carried out in the work, is presented.

At the beginning of a measurement, one of the cameras connected to the system and an exposure time are selected for initialization. Next, an angle is selected at which the exposure time is to be fine-tuned. The table now moves to this position and the user adjusts the exposure time in iterative steps. When recording an SPR curve, an angle is usually selected at which total reflection occurs without an SPR effect and the exposure time is set so that it is just below the possible maximum. Once the exposure time has been set, one can check it at other angles or jump directly to the next menu item. The recording mode is selected in this menu. The user can choose between automatically generated patterns or manual placement of ROI. The manual placement of ROI is described below. The user can also decide at which intervals measured values should be recorded. The possible intervals range from seconds to hours. Averaging over several images can also be selected. Finally, a decision must be made as to what is to be recorded. The most economical way to save data is to only record the average values from the ROIs, which will be selected in the next step. Alternatively, all image data created in the ROI or the entire image data of the camera or combinations of the options can be saved. In the next step, the ROIs are placed in the camera image. A histogram is displayed next to the camera image, which shows the brightness distribution of the pixels in the camera image. If the pixels are normally distributed, there is a high probability that a homogeneous ROI has been selected. If the intensity distribution deviates significantly from a normal distribution, there are structures or defects in the ROI. The user must decide whether this is desirable for the respective ROI or not. Below the histogram is a camera image in which all pixels outside of 3sigma are marked in red. The measurement begins immediately after the ROI has been selected and confirmed.

2.8 Simulation

The freely available software Winspall from Res-Tec GmbH employs the Fresnel equations, which describe the behavior of light at the interface between two media with different refractive indices. These equations describe the reflection and refraction of light at the interface, taking into account the polarization state of the incident light. Winspall allows the modeling of multilayer systems, which is crucial for simulating SPR experiments. In SPR, the system typically consists of a prism, a thin metal film (e.g., gold), and the sample medium. Each layer is characterized by its thickness and the complex refractive index (Table 2.3). The simulation model employed in the Winspall study is comprised of four distinct layers. The model comprises an infinitely thick glass layer of the prism, a 5 nm thick chromium layer, a 50 nm thick gold layer, and an infinitely thick analyte layer. The refractive indices for the metal layers were obtained from refractiveindex.info. The refractive indices of the glasses were obtained from the data sheets. The k-value of the refractive index of transformer oil was taken from biodiesel. The n-value was determined using a refractometer. As the measurement is carried out at the wavelength of the refractometer, only three decimal places are shown.

Table 2.3: Refractive index of the materials used for the simulation in Winspall.

Wavelength	730 nm		660 nm	
Index	n	k	n	k
Schott N-SF6	1.7892	-	1.7957	-
Schott F2	1.6112	-	1.6148	-
Chromium [6]	3.0650	3.4050	3.0891	3.3411
Gold [7]	0.15278	4.5597	0.16885	3.8758
Water [8]	1.3300	1.4960e-7	1.3310	1.8760e-8
Oil	1,478	6.8240e-8 [9]	1,478	5.5010e-8 [9]

The refractiveindex.info database is a compilation of data from publicly available sources, such as scientific journal articles and material datasheets published by manufacturers. It lists optical constants, including refractive index (n), extinction coefficient (k), and nonlinear refractive index (n2), for a wide range of materials. The refractiveindex.info database is made freely available under the CC0 1.0 Universal Public Domain.

2.9 Protocols

Prism cleaning. The glass prisms are cleaned for 10 minutes at 30°C in an ultrasonic bath (Bandelin, Sonorex Digitec) with acetone (CarlRoth, 5025.6). After this first step, the prisms are placed in a beaker with isopropanol (CarlRoth, 0080.3) and then blown off with oil-free compressed air. This cleaning step removes polish residues that can get stuck in small cavities. The dried prisms are now gripped at the end faces with plastic tweezers (Knipex, 926984.HI). The prism is turned so that the future sensor surface is facing upwards. A cleaning cloth (Thorlabs, MC-5) is placed on this surface. A drop of DI water is then applied to the paper using a safety spray bottle (Kautex, 2000770024). The drop should only be large enough to ensure that the paper adheres completely to the prism. If more water is applied to the paper, the water will run down the prism and form dry spots. Once the paper is moistened, it is slowly pulled off the prism along the long side of the paper. For the first half of this path, it is only moved slowly so that the film of water remains on the prism. In the

second half, the movement is accelerated so that the film of water bound in the cloth slowly moves away from the prism. This step is now repeated with acetone, isopropanol, and ethanol. The prism is then sufficiently cleaned for coating.

Prism metallization. A mount was developed for the prisms that enables the arrangement of several prisms in a 100 mm wafer mount (Figure 2.18).

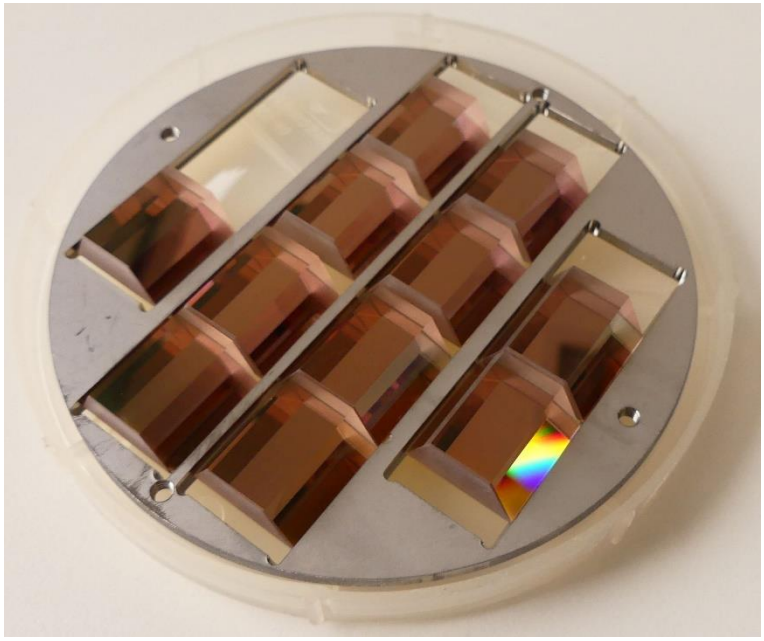

Figure 2.18: Adapter for metal vapor deposition of prisms. The adapter enables the SPR prisms to be processed in a PVD system designed for 100 mm wafers. The prisms rest on the edge of a narrow rail. Once the adapter is fully loaded, the prisms are fixed from above with a cover.

Each holder can accommodate 12 prisms, with four holders able to be integrated into the vapor deposition system (Leybold, UNIVEX 450). This configuration enables the production of 48 identical coated prisms in a single coating process. The holder is constructed from a 100 mm steel wafer, which has been milled to accommodate prism retainers. Each prism is positioned on a narrow rail on the left and right. The wafer features four threads on the edge, which facilitate the attachment of a second wafer from behind. This prevents the prisms from falling out during handling. The coating is applied via electron beam evaporation in a Leybold UNIVEX 450 evaporation system. The electron beam evaporator (FerroTec, Genius) is equipped with a turret containing five material crucibles. This process allows for the sequential evaporation of multiple materials without the need to open the chamber between each step. The evaporation rate is determined by a quartz oscillator Deposition Monitor (Inficon, XTM/2). To prevent the deposition of material on the prisms during the process parameter setting procedure, a shutter is positioned between the prisms and the material crucible. Before the material is deposited, the chamber is evacuated to $1*10^{-5}$ mbar. To accelerate the evacuation process, a thin layer of titanium is deposited in the system at $8*10^{-5}$ mbar. This acts as an additional getter material on the walls of the chamber. Once the chamber has reached its process pressure, chromium is first deposited as an adhesive layer. The gold layer is then deposited. As the PVD system is used by numerous working groups, it is necessary to determine the tooling factor of the oscillating quartz before each deposition. To determine the tooling factor, a glass plate with a mask is first placed in the system before the prisms are coated. The coating process is then carried out in the same way as it will later be carried out for the prisms. The coating thickness is then checked in a profilometer. The tooling factor is then corrected in the

system and checked again. This process is carried out until the value displayed by the oscillating quartz matches the set value. The homogeneity of the prisms is checked after coating with a Filmetrics F2-T measuring device.

Gold mirrors. The mirror references are produced using a coating process similar to the metallization of the prism. However, a gold layer at least 100 nm thick is applied here. The mirrors are structured using an adhesive mask. In semiconductor technology, either resist masks or shadow masks are traditionally used. The disadvantage of photolithographically produced resist masks is that their production is very time-consuming and expensive. Shadow masks are often used for coarser structures. However, the disadvantage of simpler shadow masks is that there is no sharp transition due to the gap between the mask and the substrate. Consequently, the vapor-deposited layer gradually becomes thicker. To address this issue, an adhesive mask process was developed. The mask is a thin film of the type typically employed as a screen protector. The film adheres independently to the surface of the substrate, without the need for an adhesive bond. After vapor deposition, the mask can be removed from the prism manually. This newly developed process bridges the gap between resist and shadow masks, enabling the production of simple structures in a straightforward and expedient manner. The films utilized in this process (Ecultor GmbH) have a thickness of 100 µm, with an additional silicone adhesive layer of 20 µm.

Solid refractive index references. The production of adhesive references is significantly affected by the process conditions of the adhesive. In this project, adhesives with refractive indices ranging from 1.3 to 1.5 were investigated, details on the materials are listed in Table 2.4.

Table 2.4: Refractive index references.

Manufacturer	Trade name	Hardening process	Viscosity	Refractive index
Norland	NOA 1315	UV	15 CPS	1.315
Norland	NOA 132	UV	15 CPS	1.32
Norland	NOA 1327	UV	4700 CPS	1.327
Norland	NOA 133	UV	15 CPS	1.33
Norland	NOA 1348	UV	160 CPS	1.348
Norland	NOA 13685	UV	15-25 CPS	1.3685
Norland	NOA 142	UV	20-40 CPS	1.42
Norland	NOA 144	UV	45-60 CPS	1.44
Norland	NOA 146H	UV / Heat	40 CPS	1.46
Norland	NOA 84	UV/VIS	40-75 CPS	1.46
Norland	NOA 85	UV/VIS	200 CPS	1.46
Norland	NOA 65	UV	1200 CPS	1.524
Norland	NOA 78	UV/VIS	8000-11000 CPS	1.50
Norland	NBA 107	UV	350 CPS	1.51
EGO	CONLOC UV 680	UV	800 mPas	1.47
EGO	CONLOC UV 651	UV	5500 mPas	1.5
Ber-Fix	UV-Kleber	UV	2500 – 5000 mPas	1.48
Ramsauer	635	Ambient / heat / moisture	Highly viscous	-
DYMAX	6-6300-T	UV/ VIS/ heat	6000cP	1.50
Cyberbond	U3150	UV	100-300 mPas	-
Cyberbond	U3200	UV	650-900 mPas	-

Table 2.4 shows that some references can be cured using heat, while others can be cured using light. Additionally, adhesives can have varying viscosities, which determine the application process. The viscosity is typically specified at a temperature close to room temperature. An adhesive with high viscosity that can be cured with UV light can be applied to the prism and cured with light. However, if the adhesive has low viscosity, precautions must be taken to prevent it from spreading over the entire prism before curing. If an adhesive with high viscosity is cured by increasing the temperature, its viscosity may decrease as the temperature rises. Therefore, it is important to take precautions to prevent the unintended distribution of the adhesive. Some adhesives have volatile components. This means that some of their components evaporate at room temperature and their refractive index is changed as a result. There is also the possibility that the adhesive may be poisoned by components in the room air and therefore no longer cure completely or change its refractive index. Such circumstances make the application of the references particularly difficult. An example of such an adhesive is Norland NOA133. However, a high viscosity can also make it challenging to apply a reference, as shown in Figure 2.19.

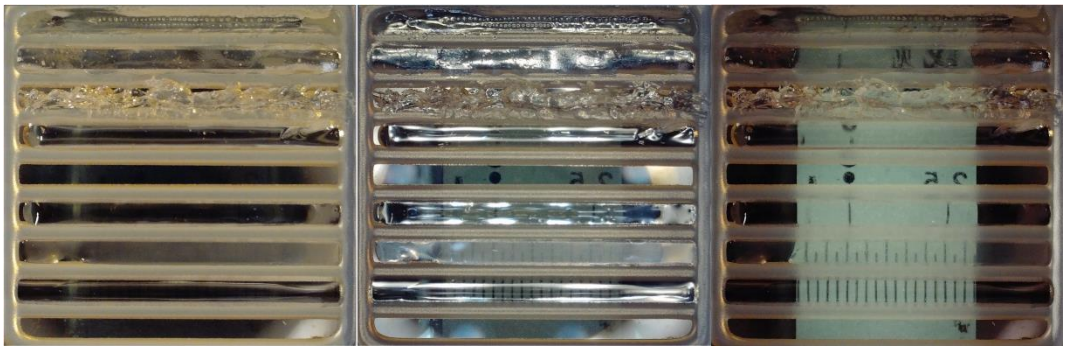

Figure 2.19: A prism was equipped with a silicone grid. Various adhesives were applied to this grid. On the left with reflected light, in the middle with reflected light and transmitted light, on the right with transmitted light.

To prevent the applied adhesives from flowing into each other, a silicone grid was added to the prism. The adhesives were then applied to the grid one after the other. Figure 2.19 displays the prism under different lighting conditions: incident light on the left, incident and transmitted light in the middle, and transmitted light on the right. It is evident that the individual adhesives have different appearances depending on the illumination. The middle chamber was not filled with adhesive, but with oil for referencing during the SPR measurement.

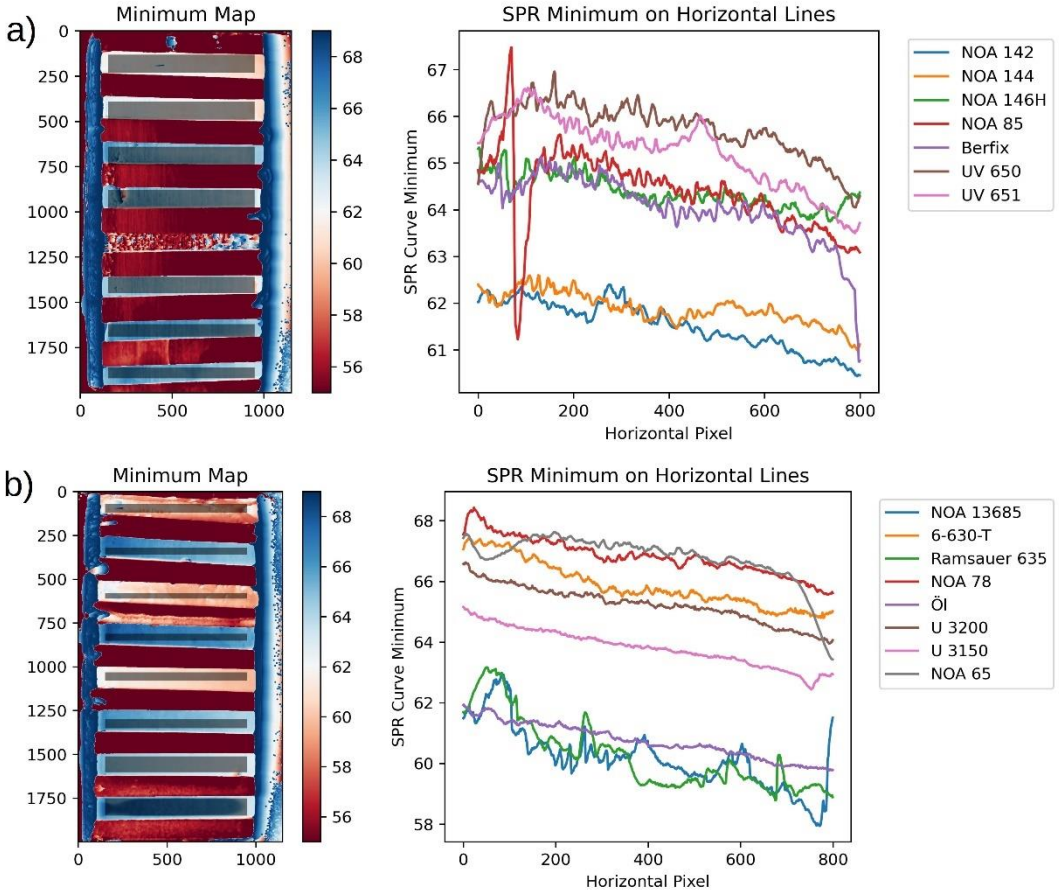

Figure 2.20: Two prisms (a&b) were coated with refractive index references and compared. Left: false color representation of the SPR minimum. Right: Position of the SPR minimum as a function of the lateral position on the prism.

Figure 2.20 displays a range of adhesives that were evaluated as potential candidates for referencing insulating oil. Two different prisms, a) and b), were used for comparison measurements. One of the prisms had a free line that was filled with insulating oil. An image of the prism surface is presented on the left, with the color of the image corresponding to the position of the SPR minimum. The silicone grid, in which the adhesives were filled, is clearly visible in red. The gray-transparent bars above the adhesive references show the areas from which the data for the graphs on the right were created. On the right, the position of the SPR minimum was plotted against its positions on the camera (horizontal pixels). This allows a better comparison with the reference made of insulating oil.

The references described above, which have a refractive index suitable for an oil matrix, are available with both high and low viscosity. In contrast, there is currently no possibility of using an easy-to-process reference with a refractive index of n = 1.33 for references for water. The Norland NOA 133 adhesive is the only one with an exact refractive index match. However, it has an extremely low viscosity, has a very low vapor point, and can only cure completely in the absence of oxygen. The adhesive's properties make it extremely difficult to process. To overcome this challenge, a process chamber for curing was developed (Figure 2.21).

Figure 2.21: An exposure system for the application of refractive index references based on UV-curing polymers has been developed. The system comprises two boxes: the upper box, which can be evacuated, is equipped with a UV lamp, and the second box contains the control electronics. These control electronics switch off the light source when the exposure time is reached or when the maximum permissible temperature is reached. The system is designed to cure polymers in a protective atmosphere and at a defined maximum temperature.

The chamber shown in Figure 2.21 can be evacuated and pressurized up to 3 bar. Taps have been fitted to the gas connections so that positive and negative pressure can be maintained independently of the vacuum pump or the gas system. The box is made of aluminum to ensure the best possible heat conduction. In the lid, 55 Watt UV lamp (EUROLITE, LED IP FL-50 SMD UV) with a nominal wavelength of 375 nm was integrated. The inside is provided with a mirror foil to reflect the emission of the UV lamp. A temperature sensor has been integrated into the box so that adhesives with low vapor pressure can also be processed. This measures the temperature in the box and can switch off the lamp if the operating temperature in the box is too high. Both the temperature and the exposure time can be regulated via a control unit. The box is placed in a freezer compartment for cooling.

Before the adhesive is applied, the process chamber is prepared by evacuating it, filling it with nitrogen and then cooling it in the freezer compartment. When the process chamber is sufficiently cooled, it is removed again and placed next to the prism on the work surface. The chamber is now opened, and the prism is placed in the chamber. A drop of the adhesive is then placed on the prism and immediately covered with a small piece of glass. The process chamber is now closed again and flushed with nitrogen. It is then placed in the freezer and the exposure process is started. NOA 133 can be cured with a wavelength of 320 nm to 450 nm. The energy required for this is 6 J/cm^2. To prevent the ingredients of the adhesive from evaporating prematurely, it must be cured at a maximum of 9°C. Due to the low viscosity, the adhesive would spread over the entire prism. However, covering the adhesive with a small piece of glass ensures that the adhesive is absorbed between the two glass surfaces and thus remains bonded in one place.

Liquid refractive index references. Solid references are often preferred due to their stable composition and resistance to fouling. However, their temperature behavior may differ significantly from that of the analyte. Therefore, it may also be beneficial to incorporate liquid references on the sensor. Figure 2.22 illustrates a sensor surface equipped with both mirror and liquid references.

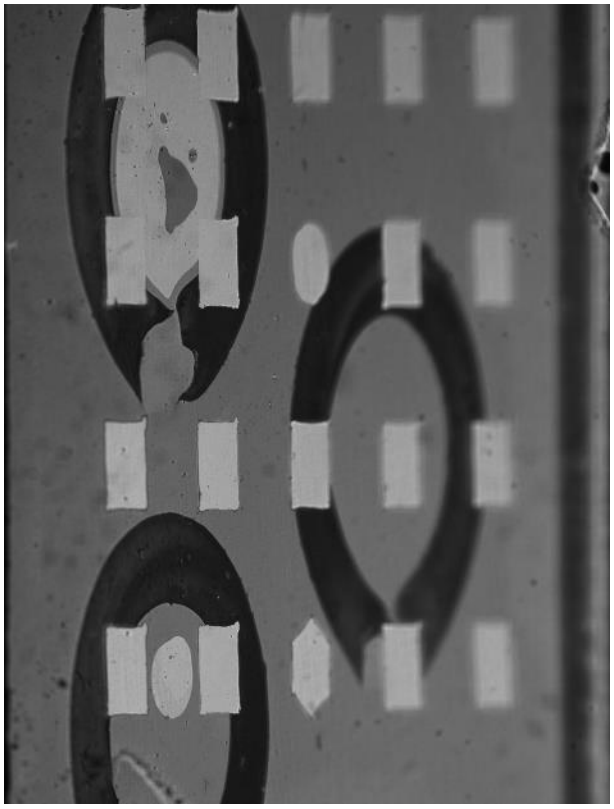

Figure 2.22: Liquid refractive index references and mirrors on a SPR prism. The (distorted) squares, the hexagon and the circle are mirror references. The black circles are the capsules in which the liquid references are enclosed.

The references can be applied in two ways. The first method involves using a standard flow cell. In this method, silicone circles are applied to the prism. It is important that these circles have the same height as the prism seal. Before the measurement, the circles are filled with the reference and sealed with the flow cell. This method offers the advantage of having a reference that is isolated from the environment and the ability to use any flow cell. However, a disadvantage is the installation process of the prism filled with reference liquid, which can be somewhat more complex.

The second method applies both the flow cell seal and the refractive index reference seal to the flow cell. This version includes a separate connection for the fluidics chamber of the liquid reference. This method allows for dry installation of the flow cell and prism. However, the reference is only filled in afterwards, creating a connection to the outside world and the possibility for the reference to be changed. Furthermore, the attachment of fluidic ports to the flow cell for the references is limiting their number. An advantage of this method is that the references can be renewed without uninstalling the SPR prism.

Oil-based references. Oil mixtures were prepared in the sample bottles used for the measurements. Wide-mouth amber glass jars from CarlRoth (AYC8.1) were used to minimize the influence of light on the oils. The GL 55 cap makes it easy to fill and remove samples. To ensure proper mixing of the oils, a magnetic rod with a center ring (CarlRoth, 1500.2) was used to stir the wide-mouth jar on a Heidolph stirring plate (Hei-Mix S, 503-02000-00). To prevent contamination

during the removing, the magnetic rod remained in the glass. The speed of the magnetic plate was set so that the vortex did not suck any air bubbles into the sample. The stirring plate was switched off to remove the samples for the refractometer. To measure the refractive index, a sample was taken from the glass and dripped onto the prism of the refractometer until it was completely covered. Samples were taken using a 5 mL graduated pipettes from CarlRoth (1CC2.1). The measuring chamber was then closed, and the measurement started. The measuring device has an internal protocol that monitors the measured value until it is stable. The measured value is then determined ten times and the average value is calculated.

After measuring the liquid was removed using Kimwipes (Kimtech, 10036000341208). They are composed of low-lint sheets, which means they leave behind minimal residue. This is crucial in the field of optics, where any foreign material can interfere with the path of light. These wipes are known for their durability. They can effectively remove dust, liquids, and tiny particles without tearing or leaving behind fibers. This makes them an excellent choice for maintaining the cleanliness of sensitive optical components. To absorb the liquid, form a small bag with the cloth. Make sure that you do not touch the bottom of the bag with your fingers. Then press the bottom of the bag onto the prism with very little pressure and move it in a circle. Make sure that you do not press so hard on the bag that your fingers rest on the prism. Instead, a soft paper buffer should always remain between the prism and your fingers. This prevents any particles from scratching the measuring prism of the refractometer. The process is repeated using a fresh cloth until the oil has been mostly absorbed. Then, take another cloth, shape it similarly, and saturate the bottom with acetone (CarlRoth, ROTISOLV® ≥99.9%, GC Ultra Grade, KK40.1). Use the acetone-soaked cloth to wipe the measuring chamber, and then repeat the process with ethanol (CarlRoth, ROTISOLV, ≥99.95%, Ultra LC-MS, 1HP8.1).

To increase or decrease the refractive index, the respective oil was dripped into the sample vessel placed on the stirring plate and mixed in. This process was repeated until the desired refractive index was achieved. Between measurements, the measuring chamber was cleaned as described above. Thanks to the numerous different oils with a high refractive index, it is possible to create oils with the same refractive index but a different composition.

Water-based references. The aqueous solutions were mixed in the same way as described for the oils in the previous chapter. However, instead of oil, sodium chloride (CarlRoth, ≥99.5 %, p.a., ACS, ISO, 3957.1) or D(+)-glucose (CarlRoth, p.a., ACS, anhydrous, X997.2) was used to change the refractive index. The substances were added using a scoop (CarlRoth, ROTILABO, 0574.1). If a specific sodium chloride or D(+)-glucose was required instead of a specific refractive index, the substances were weighed using a Kern ADB 100-4 analytical balance.

Refractive index calibration. Prior to commencing the measurement, the system was operated for a period of 45 minutes in order to achieve thermal equilibrium. A solution of 0.5 g, 1 g, 2 g, and 4 g of glucose was prepared in 200 mL of deionized water. The system was operated with DI water at the initial stage of the measurement. After certain times, the solution was switched to that of the lowest concentration of glucose, and afterwards the concentration of glucose was stepwise increased.

2.10 Final SPRi Setups

Three main SPR imaging sensor systems have been developed during this work. The setup of the reference laboratory setup which allows to achieve the best RIU resolution, a laboratory set-up which maintains the excellent RIU resolution, but which is designed to be fully functional to perform routine measurements in a bioanalytical laboratory, and a miniaturized sensor system with the focus on a small form factor and low energy consumption for a mobile use. These set-ups have been used to acquire the results described in Chapter 7.

SPR Reference Setup – Maximum RIU-Resolution. The light source is comprised of a 730 nm LED. The LED is mounted on a metalcore starboard PCB. The PCB is mounted on a brass cylinder, which is in turn attached to a Peltier element (QuickCool QC-17-1.4-8.5AS). The hot side of the Peltier is attached to a heat sink (Fischer Elektronik 10021669 SK585 20SA). The heat sink is cooled by a fan (EBM Papst 252/2 N). To ensure an efficient airflow over the heat sink surface, the fan, and the heat sink are mounted inside a housing that is forcing the air through the fans of the heat sink. After its emission from the LED the light is collimated by a lens (Edmund Optics #64-587). Subsequently the light is filtered by a wavelength filter (custom made as described in Chapter 2.2.3) and polarized by a filter (Edmund optics #85-919). The light source is directed towards a prism (Schott F2), which is coated with a thin chromium layer and a SPR-gold layer. The reflection of the SPR active prism surface is recorded with a camera (PCO Edge 4.2).

SPR Laboratory Setup – Maximum RIU-Resolution. The light source is comprised of a 730 nm LED. The LED is mounted on a metalcore starboard PCB. The PCB is mounted on a brass cylinder, which is in turn attached to a Peltier element (QuickCool QC-17-1.4-8.5AS). The hot side of the Peltier is attached to a heat sink (Fischer Elektronik 10021669 SK585 20SA). The heat sink is cooled by a fan (EBM Papst 252/2 N). To ensure an efficient airflow over the heat sink surface, the fan, and the heat sink are mounted inside a housing that is forcing the air through the fans of the heat sink. After its emission from the LED the light is collimated by a lens (Edmund Optics #64-587). Subsequently the light is filtered by a wavelength filter (Thorlabs FB730-10) and polarized by a filter (Edmund optics #85-919). The light source is directed towards a prism (Schott F2), which is coated with a thin chromium layer and a SPR-gold layer. The reflection of the SPR active prism surface is recorded with a camera (Flir BFS-U3-63S4M-C). A lens (Edmund Optics #67-714) was used to image the SPR-active surface of the prism onto the camera sensor.

Miniaturized SPR-Sensor – Maximum RIU-Resolution. The light source is comprised of a 730 nm LED. The LED is mounted on a metalcore starboard PCB. The PCB is mounted on an aluminum block, which is in turn attached to a heat sink (Fischer Elektronik SK 585 20 SA). The light is filtered by a wavelength filter (Thorlabs FB730-10), diverted by a mirror (Edmund Optics #15-488), polarized by a filter (Edmund optics #85-919), and finally diverted by a mirror (Edmund Optics #15-490). The light source is directed towards a prism (Schott F2), which is coated with a thin chromium layer and a SPR-gold layer. The reflection of the SPR active prism surface is recorded with a camera (Flir BFS-U3-63S4M-C). The housing of the camera was removed to enable the camera sensor to be placed directly on the exit surface of the prism.

2.11 References

[1] Englert M, Hartmann P, Reichel S. Optical glass: refractive index change with wavelength and temperature. In Optical Modelling and Design III 2014 May 1 (Vol. 9131, pp. 125-138). SPIE.

[2] SCHOTT AG. Temperature coefficient of Refractive Index [Internet]. Mainz (Germany): SCHOTT AG; 2016 Jul [cited 2024 Jun 30]. 14 p. (Technical Information; TIE-19). Available from:https://mss-p-009-delivery.stylelabs.cloud/api/public/content/0dcd87a2d36942a3946d033f0a9065e6?v=940fa3fb&download=true

[3] SCHOTT AG. Optisches Glas - Datenblatt-Sammlung [Internet]. Mainz (Germany): SCHOTT AG; [cited 2024 Jun 30]. 2.23 MB. Available from: https://media.schott.com/api/public/content/9a17a153adb1464591ca4c1fc7dae8a6?v=77e0fe49&download=true

[4] Xinhua L, Shengpeng L, Zhou L, Xianhua Z, Xiaohu C, Zhongbin W. An investigation on distortion of PLA thin-plate part in the FDM process. The International Journal of Advanced Manufacturing Technology. 2015 Jul;79:1117-26.

[5] ASTM Committee D-20 on Plastics. Subcommittee D20. 50 on Permanence Properties. Standard Test Method for Water Absorption of Plastics. American Society for Testing and Materials.

[6] Johnson PB, Christy RW. Optical constants of transition metals: Ti, v, cr, mn, fe, co, ni, and pd. Physical review B. 1974 Jun 15;9(12):5056.

[7] Yakubovsky DI, Arsenin AV, Stebunov YV, Fedyanin DY, Volkov VS. Optical constants and structural properties of thin gold films. Optics express. 2017 Oct 16;25(21):25574-87.

[8] Hale GM, Querry MR. Optical constants of water in the 200-nm to 200-µm wavelength region. Applied optics. 1973 Mar 1;12(3):555-63.

[9] Wang CC, Li XC, Tan JY, Liu LH. Experimental measurement of optical constant of biodiesel by double optical pathlength transmission method. Laser Optoelectron. Prog. 2015;52(5):051206.

3. Surface Plasmon Resonance Imaging for Detection of Drug Metabolites in Water

Abstract: The analysis of surface water, groundwater, drinking water as well as sewage is important to get information about the contamination of the water cycle. Currently, these time-consuming investigations require special equipment, like for example hyphenated mass spectrometry. Surface plasmon resonance (SPR) is a faster alternative as it is highly sensitive to changes in the dielectric medium next to a thin metal layer and makes it a quasi-universal detector. Therefore, and due to the label-free nature, SPR is a widely used sensing tool for real-time monitoring of molecular interactions of various analytes. SPR imaging (SPRi) has several advantages to standard surface plasmon resonance, as it allows observing many analytes in parallel as well as the integration of referencing technologies. However, the homogenous illumination of a large area (several millimeters) with a small light source is challenging and demands new approaches. Allopurinol, a drug used to lower the blood concentration of urate and hence decrease the affection of gout, gets metabolized to oxipurinol in the body and dropped out almost entirely by urinary excretion. After wastewater treatment, concentrations of oxipurinol up to 21.7 $\mu g \cdot L^{-1}$ are detected. Further tracking of oxipurinol in the urban water cycle showed its presence in rivers and streams or even in groundwater. Therefore, the high biological stability of oxipurinol allows this molecule to be used as a marker for domestic wastewater in the environment. For the detection of oxipurinol by SPR, graphene was used as receptive layer, as the analyte can bind via π-stacking to this surface. A SPRi technique was developed and compared to conventional SPR system for the detection of oxipurinol.

3.1 Introduction

Drinking water is a, if not the most valuable resource on the planet. That is why huge effort is made for its quality control. At the moment these processes are mostly based on laboratory methods, especially chromatography or spectrometry, which are both laborious, but more important time consuming [1, 2]. This makes on site and rapid observation impossible. In contrast SPR benefits of label-free, real-time, and online monitoring [3, 4]. In a typical SPR measurement setup a laser excites surface plasmons on a metal layer deposited on a prism [5]. These plasmons are sensitive to refractive index changes in a thin layer of about 300 nm next to this metallic surface, which makes this method a powerful technique in fluidic systems. By applying receptive coatings to the gold film highly specific sensors to desired analytes can be designed. To increase the sensor capability, the system can be upgraded from a one spot measurement device to a more advanced imaging setup, detecting several analytes in parallel on one single sensor chip [6]. After the invention of surface plasmon microscopy by Rothenhäusler and Knoll in 1988 [7], SPRi was rapidly growing in the interest of researchers [8, 9]. Beside many other SPR methods, the most prominent application is a Kretschmann configuration with readout based on intensity modulation [4, 10]. The operation principle is explained in Figure 3.1. Monochromatic, polarized, and collimated light is

used as the excitation source, and the angle of incidence is fixed near to the resonance angle. Due to the energy transfer at the resonance condition, the intensity of the reflected light is damped.

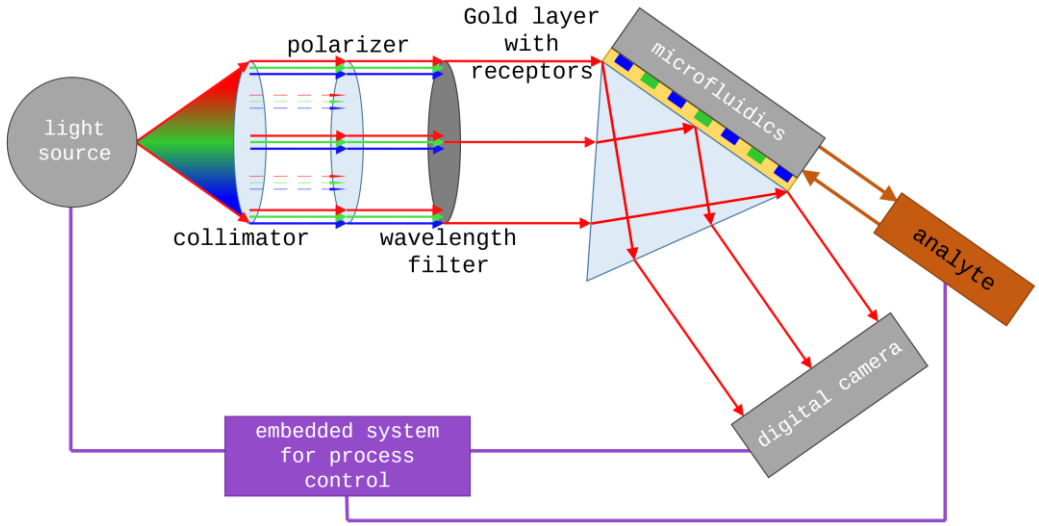

Figure 3.1: Scheme of a surface plasmon imaging setup illustrating its main components.

The resonance angle can be influenced by many parameters [3], which are all fixed in this setup. With one exception, which is the refractive index next to the gold layer opposite to the glass. If the medium, which is flowing over the gold layer, is changing its refractive index due to a change of its composition, the resonance angle will also shift. Since all molecules have a specific refractive index, SPR is capable of measuring everything which leads to a significant change in the refractive index within the evanescent field above the gold layer. This fact makes SPR one of the most powerful, non-destructive methods of analysis. One of the challenges in SPR technique is the detection of small molecules, which demand high sensitivity due to small changes in refractive index. Therefore, the modification of the metallic sensor surface by graphene introduces intrinsic surface plasmons of the 2D material enhancing the sensitivity of the SPR sensor [11]. At the same time graphene can be used as recognition element, utilizing its conjugated π-electron system for π stacking, as already demonstrated for adenine [12]. An analyte with a similar structure is oxipurinol, the metabolite of the anti-gout formulation allopurinol. Oxipurinol occurs in wastewater in relative high concentrations and therefore can be used as marker for leaking drinking water pipes [13]. Miniaturized SPR based oxipurinol sensor could be used to map the water supply infrastructure of possible contaminations. Here we compare the sensitivity of SPRi to a classical SPR system with focus on the challenges in illumination as well as in the receptor design on the gold surface.

3.2 Experimental Part

Glass slides (20 × 20 mm²) with a refractive index of 1.61 (Mivitec GmbH, Sinzing, Germany) and a gold layer (50 nm) on top were used in combination with the BioSuplar SPR device (Mivitec GmbH, Sinzing, Germany) with a F1-65 glass prism installed on a swivel holder. Prior to usage, the slides were cleaned with analytical graded ethanol and dried with nitrogen. In case of the 2D setup a F2

Prism (Schott AG, Mainz, Germany) with a gold layer (50 nm) on top were used and similarly prepared. In both cases the graphene receptor material was deposited on the gold surface.

Reduced graphene oxide (rGO) was prepared by a slightly modified Hummers method [14] with subsequent reduction [15]. Briefly, 1 g of China flake graphite (K. W. Thielmann & Co KG, Grolsheim, Germany) was mixed with 0.75 g $NaNO_3$ in 75 mL conc. H_2SO_4. In small portions, 4.5 g $KMnO_4$ was added, and the mixtures was vigorously stirred under cooling in an ice bath. After 3 hours sonication, the dispersion was stirred for 3 days at room temperature. Next 75 mL of 5% H_2SO_4 was added the mixture and heated to 100 °C for 2 hours, followed by an addition of 15 mL of 30% H_2O_2. The resulting graphene oxide was washed four times with 3% H_2SO_4 containing 0.5% H_2O_2, two times in 3% HCl, and three times in water. At last, the product was dialyzed against 2 L of water by a 14 kDa cut-off dialysis membrane for 10 days. The GO was chemically reduced by suspending GO (0.5 $g \cdot L^{-1}$) in water and mixing it with 31 µL of 32% NH_3. After the addition of 5 µL of hydrazine hydrate (98%) the reaction mixture was refluxed for 1 hour at 100 °C. The resulting black suspension was washed with water and rGO was isolated by centrifugation.

Reduced graphene oxide (rGO) was deposited by a spin coating procedure whereby a spin coater type WS-400BZ-6NPP/LITE (Laurell Technologies Corporation, North Wales, Pennsylvania, USA) was used. 200 µL of rGO with a mass concentration of 0.25 $mg \cdot mL^{-1}$ in a mixture of isopropyl alcohol and double distilled water 1:1 (v/v) were spin-coated for 15 min at 1000 rpm with initial 5 min accumulation time.

The SPR measurements were performed by assembling the functionalized SPR slide or prism in the respective device. The analyte binding to the sensor surfaces was monitored at constant angle which was chosen slightly below the angle of minimum of the SPR resonance curve. A fluid velocity of 400 $mL \cdot min^{-1}$ was chosen. Calibration was performed with NaCl solutions of known refractive index, with concentrations of 100, 200, and 400 mM. The oxipurinol solutions of concentrations ranging from 1 to 50 µM were run over the gold surface for 6 min each with a subsequent washing step of 10 min.

3.3 Results

Standard SPR is using a laser as light source and a photodiode as detector. This is obvious since a laser diode is providing collimated, polarized, and monochromatic light. Photodiodes do have an excellent sensitivity while having a low price. However, this setup is merely capable of doing single or multi-channel sensing. SPRi is way more powerful. While using a camera as detector, the number of channels is extended tremendously. By realizing region of interests (ROI) of 100 × 100 µm while having a sensing area of more than 10 × 10 mm an array of 10,000 different measurement spots on a gold film was obtained. This gives the following important advantages: a) monitor a lot of different analytes in an array format, b) exclude measurement spots on the sensor film which are not so sensitive, or which cause only noise and c) get higher precision by averaging many measurements spots at the same time. The most limiting part for such a system is the light source. So far, this setup was mainly used with a laser light source. However, laser light sources are causing speckles and

diffraction patterns. If coherent light shines on a surface with a roughness in the range of the wavelength, then an interference phenomenon called speckles occurs. Therefore, optical components with a surface roughness of less than 4 nm were used. However, the diffraction patterns are still present as can be seen in the left image in Figure 3.2.

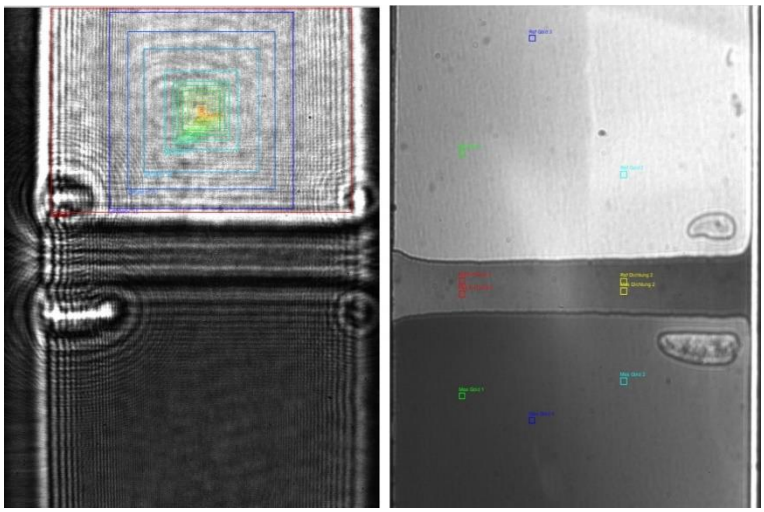

Figure 3.2: A 62° prism made of Shott N-SF6 glass, p4-polished, coated by a 4.2 nm chromium adhesion layer and a 44 nm gold sensing layer. Left side: SPR image when illuminated with a 660 nm laser diode; Right side: SPR image when illuminated with a 660 nm light emitting diode. The light is filtered by wavelength filter with a full width half maximum of 2 nm and a polarizer with an extinction ratio of 1:9,000. Homogenization is done by an opal glass.

Therefore, it was necessary to design a monochromatic and polarized light source, which does not have the spatial coherence of lasers. The light source is based on a light emitting diode, which is homogenized by an opal glass. Its lateral size is limited by a slit and the collimation is done by an aspheric lens. Its divergence is small enough to enable an image without utilizing a lens in front of the detector (Figure 3.2, right side). This light source still suffers from a certain divergence, which is utilized to spread the readout angle in a miniaturized sensor setup. Figure 3.3 shows the SPR curve of the ROI which are shown in Figure 3.2. The sensing area of Figure 3.2 is divided in two areas containing different media of varying refractive indices: for the upper one n = 1.48310 (oil from the type of Nynas Nytro Taurus) and for the lower one n = 1.45241 (oil from the type of Shell Diala S4). The ROIs marked by solid light blue, dark blue and green line are in upper region and the corresponding ROIs marked with dashed lines are in lower part. Despite that always three ROIs are in the same media, their curves are shifted in the angle as displayed inFigure 3.3. This can be explained by the altered angle of incidence. The angle is altered by its horizontal position and the value of the divergence is determining the shifting of the angle.

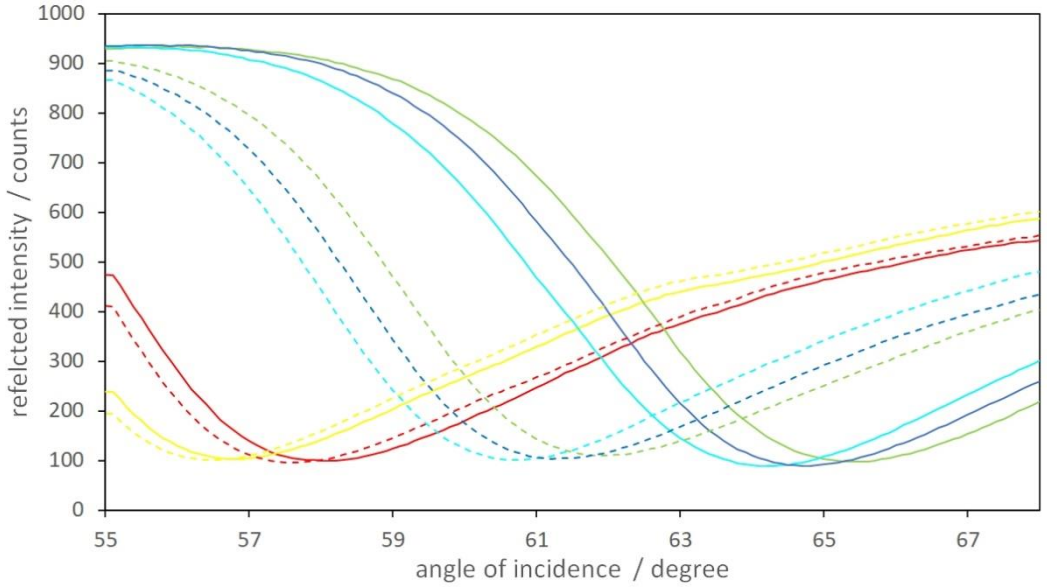

Figure 3.3: SPR curves, recorded with the homemade SPRi system. The curves are recorded according to the ROI depicted at Figure 2.24 (right side) with the corresponding color: the turquoise, blue and green curve are shifted to each other, since the angle of incidence is shifted from the left to the right, this feature of the LED based light source enables an angle scan without moving the prism or the angle of the incidence in the setup. The dashed turquoise, blue and green curve are taken from the lower chamber, while the solid ones are from the upper chamber.[1]

This feature allows an exact positioning of individual receptors with different refractive index at exactly that measuring angle which shows the maximum in sensitivity for this receptor.

This SPRi set-up was used in the following to be compared for its capabilities in detecting oxipurinol in water. The gold was modified by rGO as receptor for aromatic molecules. A characterization of the sensor surface was performed by Raman microscopy (Figure 3.4). One can clearly see from the maps of the typical G and 2D band of the carbon nanomaterial that spin coating leads to an incomplete and inhomogeneous coverage of rGO on the gold surface. This is even more pronounced when looking at the mathematically divided maps as displayed in Figure 3.4. From the color distribution as obtained from the intensity of the 2D peak one can estimate that approx. 16% of the surface is covered.

[1] Updated the formatting of the image to match the format of the rest of the renderings.

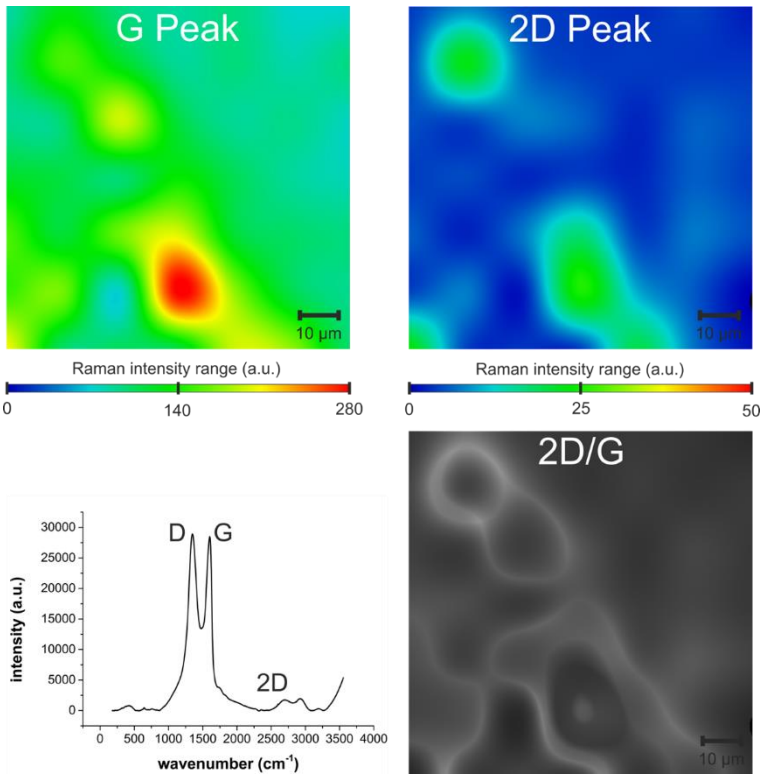

Figure 3.4: On the top: Raman maps from the G-Peak (~1,550 cm 1) and the 2D-Peak (~2,700 cm 1). The respective intensity is displayed by colors, the scale is given for each image. Both peaks are typical Raman characteristics for two-dimensional carbon materials. A single Raman spectra of reduced graphene oxide is shown in the bottom left. Both peak maps show inconsistencies on the surface, but this can be also due to differences in defect density of the graphene. Therefore, an overlay of both peaks was created (bottom right), to normalize over the defect influence, which then reveals the incomplete coverage with nanomaterial.

For retrieving best sensitivity, a monolayer of graphene would be best. Up to now there is no reliable technique available which produced such films in large scale and at a reasonable prize. Inhomogeneity's in receptor layers are often found and in classical SPR technique this leads to low signal-to noise ratio. For example, in the commercial system we are using here to compare classical SPR to the homebuilt SPRi the spot illuminated by the laser beam is approx. 75 mm^2. There is no chance to exclude some parts from the signal. This means if only 16% of such an area is covered by a receptor the binding of an analyte will result only in a small change of the signal. In case of imaging, one can define the ROI with pixel precision and will therefore exclude regions where only noise will be generated. This can be seen when comparing gold films modified by rGO with exactly the same protocol, but one was measured in the SPRi system, the other with the classical SPR device. The binding constant of the oxipurinol, estimated from the signal response as shown in Figure 3. 5, is for both measurement setups identical and can be given as (2.2 ± 0.05) 10^5 M^{-1}. This is expected as the same receptor and analyte was studied. Nevertheless, for the SPRi system a limit of detection (LOD) of 199 ± 9 nM was obtained, whereas in the classical SPR system oxipurinol can only be detected with a LOD of 783 ± 25 nM. The LODs were calculated from the signal-to-noise ratio.

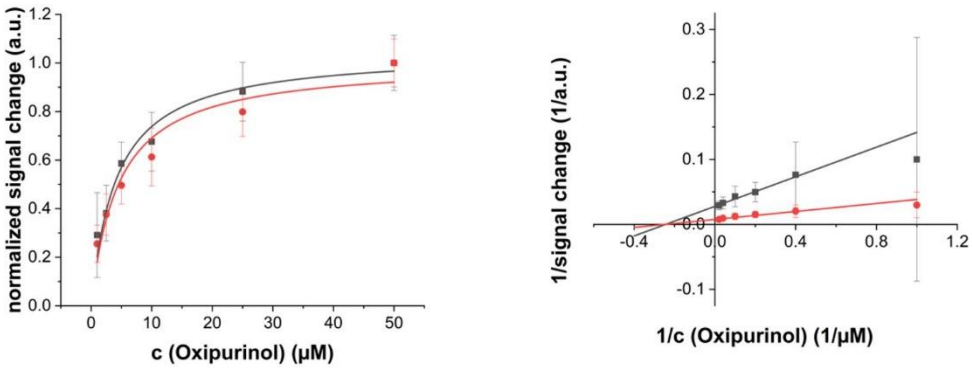

Figure 3. 5: Left: Normalized signal change as a function of the oxipurinol concentration for the classical SPR setup (grey) and for the SPRi setup (red). Both setups show a similar behavior. Right: Lineweaver-Burk plot of the same data for the calculation of the binding constant. Error bars represent signal to noise ratio.

In general, for the SPRi system it was found that the LOD depends on ROI position and ROI size. A ROI with 6,400 pixels increases the LOD by eight times compared to a ROI with 100 pixels. If the ROI is even more enlarged to 102,400 pixels this LOD gets further improved by two times. This effect can be ascribed to the huge number of individual measurement spots which will be averaged, whereas in classical SPR this is not possible. If the ROI gets too large an increase in the response time is encountered due to the fluidics. The choice of the ROI position on the gold film can also drastically enhance the sensitivity as demonstrated by the angular dependency on a horizontal line on the chip. To further reduce the noise and hence the LOD it is necessary to start the measurement under such settings making full use of the dynamic range of the camera. This can be realized by increasing power of the light source or by longer exposure times of the camera, and by the right choice of the ROI, especially for inhomogeneous receptor layer.

3.4 Conclusion

SPRi is promising in the development of online sensors due to its label-free and non-destructive nature, demonstrated by the proof-of-concept determination of oxipurinol in water at low concentrations. This was achieved using two-dimensional carbon materials as receptive layer. The advantage of SPRi is demonstrated by the problem of fabricating a homogeneous sensing layer. In SPRi this can be overcome by choosing the ROI. It can be envisioned that this will be fully automated by a cookie-finder algorithm. At the same time this receptor detects all molecules which can interact with the receptor by π-stacking. To get selectivity another advantage of SPRi becomes important. The sensor surface can be functionalized by various receptors allowing the design of arrays, with different response characteristics. This will also be of high interest when it comes to non-targeted analysis, where machine-learning will be used to assign changes in individual ROIs to a chemical compound or any unknown species which should not be present in the analyzed matrix.

3.5 References

[1] Petrović, M., Gonzalez, S., Barceló, D. 2003 *Analysis and removal of emerging contaminants in wastewater and drinking water.* TrAC Trends in Analytical Chemistry. 1;22(10):685.

[2] Berijani, S., Assadi, Y., Anbia, M., Hosseini, M.R., Aghaee, E. 2006 *Dispersive liquid–liquid microextraction combined with gas chromatography-flame photometric detection: very simple, rapid and sensitive method for the determination of organophosphorus pesticides in water*. Journal of Chromatography A. 1123(1):1.

[3] Schasfoort, R.B., editor. 2017 *Handbook of surface plasmon resonance*. Royal Society of Chemistry.

[4] Homola, J., Yee, S.S., Gauglitz, G. 1999 *Surface plasmon resonance sensors.* Sensors and Actuators B: Chemical. 54(1-2):3.

[5] Liedberg, B., Nylander, C., Lundström, I. 1995 *Biosensing with surface plasmon resonance—how it all started*. Biosensors and Bioelectronics. 10(8):i.

[6] Puiu, M., Bala, C. 2016 *SPR and SPR imaging: Recent trends in developing nanodevices for detection and real-time monitoring of biomolecular events*. Sensors. 16(6):870.

[7] Rothenhäusler, B, Knoll, W. 1988 *Surface–plasmon microscopy*. Nature. 332(6165):615.

[8] Scherbahn, V., Nizamov, S., Mirsky, V.M. 2018 *Toward ultrasensitive surface plasmon resonance sensors. Label-Free Biosensing: Advanced Materials*, Devices and Applications. 409.

[9] Homola, J., Vaisocherová, H., Dostálek, J., Piliarik, M. 2005 *Multi-analyte surface plasmon resonance biosensing. Methods.* 37(1):26.

[10] Kretschmann, E. 1971 *Determination of optical constants of metals by excitation of surface plasmons*. Zeitschrift für Physik. 241(4):313.

[11] Genslein, C., Hausler, P., Kirchner, E.M., Bierl, R., Baeumner, A.J., Hirsch, T. 2017 *Detection of small molecules with surface plasmon resonance by synergistic plasmonic effects of nanostructured surfaces and graphene*. Plasmonics in Biology and Medicine XIV (Vol. 10080, p. 100800F). International Society for Optics and Photonics.

[12] Genslein, C., Hausler, P., Kirchner, E.M., Bierl, R., Baeumner, A.J., Hirsch, T. 2016 *Graphene-enhanced plasmonic nanohole arrays for environmental sensing in aqueous samples*. Beilstein Journal of Nanotechnology 7(1):1564.

[13] Funke, J., Prasse, C., Eversloh, C.L., Ternes, T.A. 2015 *Oxypurinol–a novel marker for wastewater contamination of the aquatic environment*. Water Research. 74:257.

[14] Hummers, W.S., Offeman, R.E. 1958 *Preparation of Graphitic Oxide*. J Am Chem Soc 80:1339.

[15] Li, D., Müller, M.B, Gilje, S., Kaner, R.B., Wallace, G.G. 2008 *Process able aqueous dispersions of graphene nanosheets*. Nat Nanotechnol 3:101.

4. Homogeneous Light Source for Surface Plasmon Resonance Imaging

Abstract: We describe how to build a homogeneous light source for Surface Plasmon Resonance Imaging (SPRi) which mainly finds its applications in pharmaceutical screening and biotechnology so far. SPR spectroscopy is a label-free, non-destructive, and highly sensitive measurement principle for detecting changes in the refractive index in close vicinity of a gold surface. A transfer of this technology to a miniaturized sensor will broaden the range of possible applications. Commercial SPR assays are mainly working with a small number of sensing spots. In contrast, the SPR imaging system shown here will allow the use of an array of many sensing spots. In combination with chemical receptors designed as an artificial nose or an electronic tongue, the simultaneous detection of many analytes is envisioned. So far, lasers or other inhomogeneous light sources were used to illuminate the sensing surface, which is decreasing the systems sensitivity. We show a compact (< 60 mm), low cost, LED based light source which is providing a large area (> 300 mm^2) homogeneous top hat profile. The combination of a high bit-resolution camera with our new light source enables a reflectivity-based surface plasmon resonance imaging system with a high refractive index unit (RIU) resolution.

4.1 Introduction

Surface Plasmon Resonance (SPR) technology is label free, non-destructive, and highly sensitive [1]. Due to these properties, SPR is an attractive measurement principle for chemical sensors. Nevertheless, there are some drawbacks limiting its applications so far: most measurement setups are designed for being used in laboratories and therefore they are very expensive. The high temperature sensitivity and the need of trained personal for its operation impede reliable in-field sensing. Miniaturized and automated systems could overcome these problems. Motivated by these prospects, many miniaturized systems were developed, and reviewed in an overview on miniaturized SPR systems [2]. Most of these systems suffer either from missing transportability or from low sensitivity.

Beside reflectivity based SPR imaging (Figure 4.1) many other SPR technologies have been developed to increase sensitivity, Wang *et al*. provides a review about the state of the art and an overview of the most common technologies [3]. However, these technologies are introducing new components which are complicating miniaturization.

To be able to apply reflectivity based SPR-imaging to miniaturized sensor systems we developed a compact, low-cost light source, which is providing a large area, homogeneous illumination.

4.2 Sensing Principle

While a thin gold film is irradiated by light, typically the entire light will be reflected (Figure 4.1). However, if the light is p-polarized and the angle of incidence is altered, one can see a narrow dip in the intensity of the reflected light. This dip is indicating that at this certain angle of incidence (SPR angle) surface plasmons are excited. The SPR angle mainly depends on the refractive index in close proximity to the gold film that is deposited on a coupler, usually a glass prism. Therefore, the refractive index on one side of the gold is constant, which means that any variations in the chemical composition – and therefore in the refractive index – next to the other side of the gold film is determining the position of the SPR-angle. Selectivity to a special molecule of interest is generated by a chemical functionalization of the gold film by recognition elements. There are many ways on how to utilize surface plasmons [3]. The principle we used is reflectivity based SPR, since it has the simplest setup. Hence, it is the most promising method for miniaturization. Reflectivity based SPR has no moving parts, which makes it more robust. During the design process, one fixed angle at the linear region of the SPR-reflectivity slope is chosen for measurement. If the refractive index of the analyte is changing, the position of the minimum is moving and hence the reflectivity is changing.

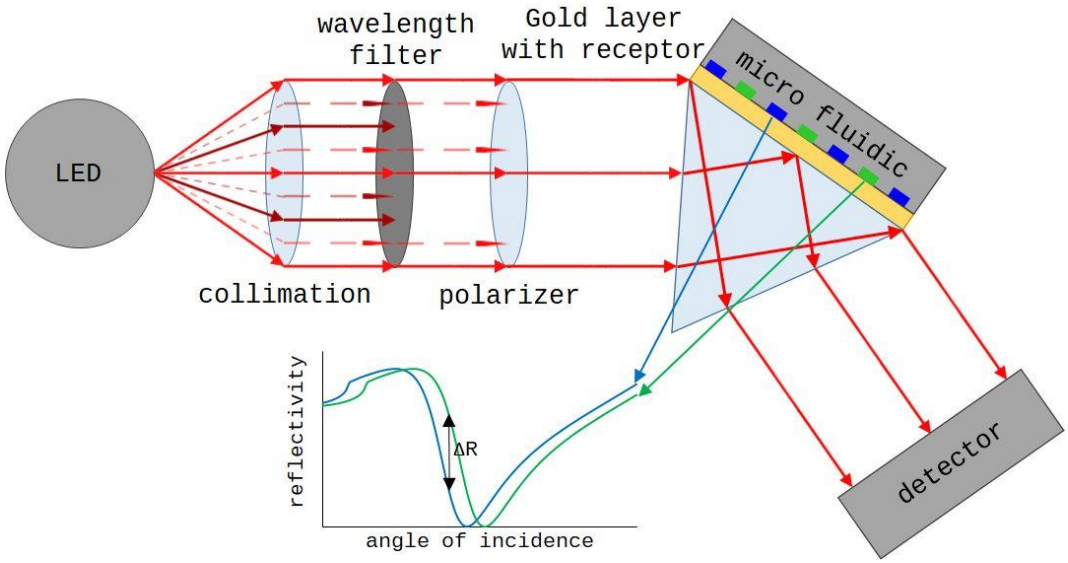

Figure 4.1: System-setup, consisting of a LED based light source, a gold-coated prism with receptors and a detector as well as an 18 × 18 mm microfluidic chip, which is distributing the analyte.

4.3 System Setup

Most single or multi-channel SPR setups are using laser light sources. For SPR-imaging, lasers are not suitable since they are known for generating speckles and diffraction patterns (Figure 4.2). Typical regions of interest (ROI) do have a size between 50 µm and 5 mm. While having small size ROI, the noise which is generated by the diffraction patterns is lowering the resolution of the system dramatically. Most lasers also have a Gaussian beam profile. If the sensing surface is illuminated with a Gaussian beam profile a small movement of the components will cause a movement of the steep flank thorough the ROI and hence a high change of the reflected signal. The replacement of

the laser by our LED based light source overcomes this issue. LED light is very broadband compared to laser light and it is non-polarized. Therefore, a wavelength band pass filter and a polarizer were integrated into the system. Furthermore, the beam is tailored and collimated. The modified beam illuminates a 50 nm gold film that is on top of a Schott F2 glass prism. The reflected light is collected by a 2D-camera system, which records the spatial change of the intensity of the reflected light beam (Figure 4.1).

Superluminescence diodes would provide similar characteristics to lasers but without spatial coherence, but they are excessively expensive. The high price would impede the use of the SPR technology for infield sensors.

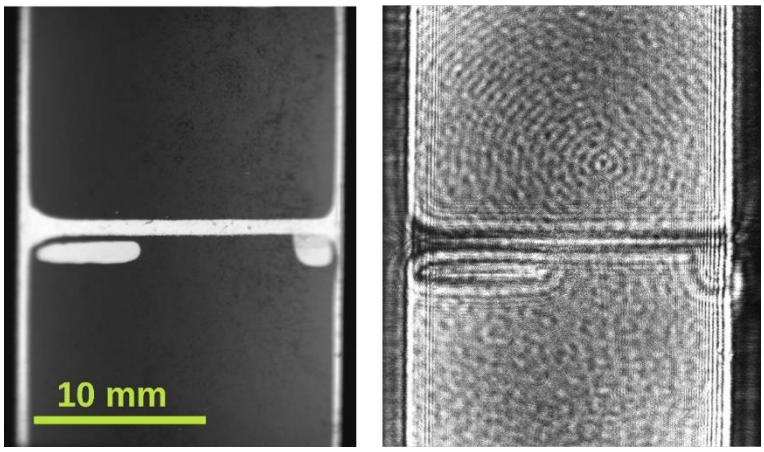

Figure 4.2: Comparison of a LED light source left and a laser light source right; the coherent laser light is generating diffraction patterns due to dust particle, edges, and air bubbles.

The aim was to build a light source which is available at a low price, and which can be miniaturized. Non-stabilized lasers show mode hopping, which would introduce noise and lower the systems resolution. Speckles and other diffraction patterns would also generate some noise. Furthermore, the widening of the laser beam would require a long optical path. Therefore, lasers are not suitable for miniaturized systems.

The SPR effect is very sensitive to wavelength shift and its sensitivity is increasing with an increasing wavelength (Figure 4.3). On the other hand, the sensitivity of CMOS cameras is decreasing rapidly with an increasing wavelength. Moreover, the development of a system is much easier if the wavelength is visible.

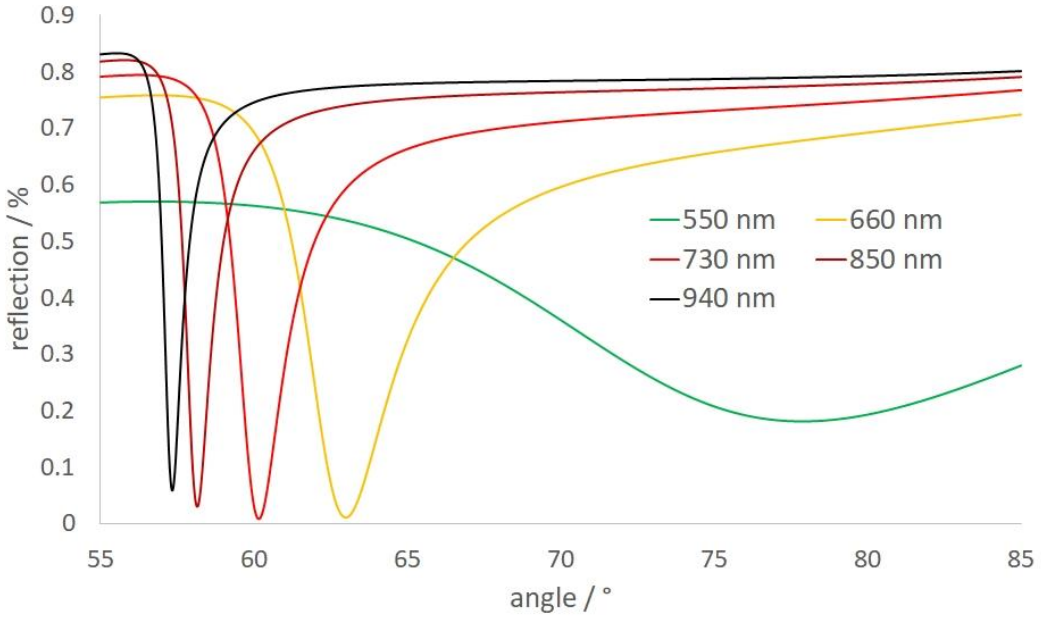

Figure 4.3: Simulated SPR-curve for Schott F2 glass coated with a 1 nm chromium adhesive layer and a 50 nm gold layer. The analyte is water. Simulation was done with Winspall software.

To have the system components available for very low price at good performance we have chosen a 660 nm LED from OSRAM (GH CSSRM2.24). It is an important wavelength for horticulture and is therefore readily available. To be able to alter the driving current and to have low noise at the same time, we used a Keithley source meter as a current source for the laboratory setup.

The beam shaping was done with a single 25 mm diameter plastic aspheric lenses from Edmund Optics. Depending on the desired beam characteristics, the focal length was chosen at a range between 25 mm and 75 mm. To avoid a wavelength shift, a custom-made 2 nm FWHM filter from Chroma was used. The polarization was controlled with a 1:9,000 polarizer from Edmund Optics.

The prism is made of Schott F2 glass and has P4 polished surfaces to provide best performance.

By altering the position and the focal length of the collimation lens, the divergence of the light can be altered. If the SPR system is built with a light source with low or no divergence, a camera can be used even without objective lenses.

The suitable camera should be chosen depending on the demands, concerning refractive index unit (RIU) resolution, system price and volume. The Ximea MU9PM-MH with its APTINA MT9P031 sensor is offering a 12-bit resolution at a low price and very low volume (15 × 15 × 8 mm) while the PCO Edge 4.2 is offering an outstanding resolution of 16-bit. The PCO Edge with its 16-bit is providing a high RIU resolution and the large chip size is enabling an acquisition of a large SPR-image without the use of a lens. Between these two cameras, there are many different cameras, which could be used. Currently, a good compromise between costs, size and bit resolution are cameras with a Sony IMX178 sensor like the ISG Allegro.

4.4 Results

Figure 4.2 shows the comparison of an LED light source (left) and a laser light source (right). Both are providing a “top hat like” beam profile. In case of the laser, a very small area at the center of the Gaussian beam profile was cut out. This process is generating diffraction pattern at the edge of the lenses, which were used to cut out the center part. Furthermore, the edges of the prism and microfluidics as well as air bubbles and dust are generating diffraction patterns. The result is a very noisy illumination, which could be sufficient for single or multi-channel measurement with very large regions of interest (ROI), but it is totally insufficient for high-resolution SPR imaging.

Figure 4.4 shows a SPR image which was recorded with a laser based light source. The cross-section, which was taken along the direction of the black line shows that there is tremendous noise which is lowering the RIU resolution of the SPR imaging system. To avoid this kind of noise a LED based light source was developed. LED’s do not have spatial coherence; therefore, they do not generate diffraction patterns.

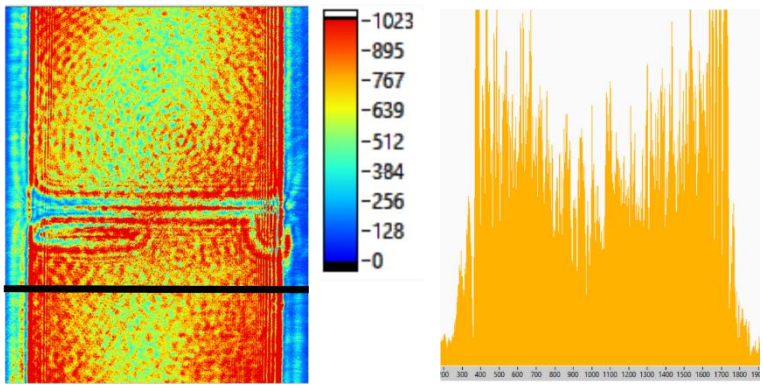

Figure 4.4: False color SPR image made with a laser based light source and a Ximea CMV4000 10-bit camera; left: diffraction patterns originating from edges, dust particles and air bubbles are visible; right: cross-section along the direction of the black line from the left side, the noise which is originating from diffraction is clear to see.

Figure 4.5 shows a SPR image, which was recorded with a LED based light source. The cross-section, which was taken along the direction of the black line shows the SPR curve which is originating from the light source divergence. A LED cannot be collimated like a laser; therefore, a small divergence will always remain. Unlike Figure 4.1, which shows perfectly collimated light from a laser, a LED based light source is generating light rays, which are not perfectly parallel. Therefore, the angle of incidence is shifting slightly from one side to the other side of the sensing area. This divergence can be utilized to monitor every sensing spot at its most sensitive angle. If the SPR system does not monitor only one receptor but many different, *e.g.*, 100 spots, it is very likely that every spot has a different refractive index. This implies that only one spot is monitored at its most sensitive SPR angle if a non-divergent light source is used, all the others are falling behind their possibilities. However, if a divergent light source is used, the angle of incidence is splayed, and every receptor can be placed at its most sensitive angle of incidence.

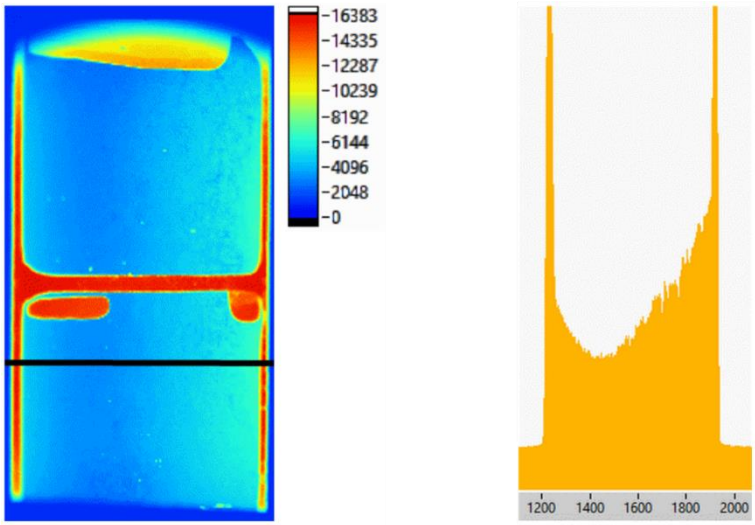

Figure 4.5: False color SPR image, made with a LED light source and an ISG allegro 14-bit camera; left: the SPR active area is illuminated homogeneous, red areas are the sealing and air bubbles; right: cross-section along the direction of the black line, the cross section shows the SPR curve which is originating from the divergent illumination.

While collimating a perfect point source is very simple, homogenizing an LED is very complex. One could use an opal glass, but this option would cause tremendous power losses on the one hand and focusing on infinity would not lead to a homogeneous beam shape on the other hand. Therefore, we developed another technique to create a homogeneous beam area (Figure 4.6). We have found an empirical equation which relates focal length of the lens, distance of the lens to the desired homogeneous surface and lens placement:

$$d_{L-FP} = (m_1 d_{L-HS} + b_1) \cdot \exp\left(f(m_2 d_{L-HS} + b_2)\right)$$

The distance of the lens, relative to the focal plane of the lens is called $d_{L\text{-}FP}$. The distance of the lens to the homogeneous surface is called $d_{L\text{-}HS}$. The focus length is called f and m_1, m_2, b_1, b_2 are dimensionless constants with m_1 = -2.5698 e^{-3}, m_2 = -37.265 e^{-6}, b_1 = 1.9311, b_2 = 0.0383.

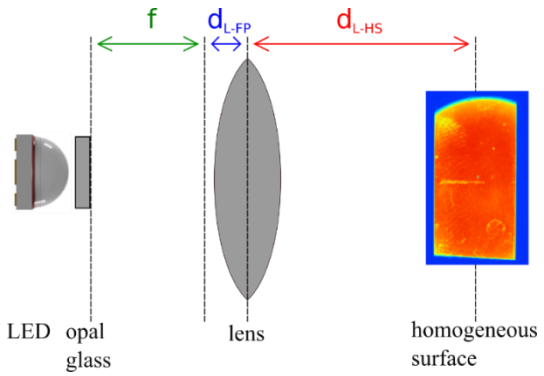

Figure 4.6: Placement of optical components, the 1 mm aperture in front of the opal glass has been omitted in the schematic.

The SPR sensing area is inclined according to the beam direction (Figure 4.1) therefore the beam must be homogeneous in a wider area along the beam direction and not only in one plane. The $d_{L\text{-}HS}$ is the distance between the lens and the center of the homogeneous area.

This equation is valid for focus length in the range of *f*20 to *f*120 and for a lens – homogeneous region distance of 40 mm up to 110 mm. The equation should be understood as an approximation, which is helping to build a homogeneous light source, which is based on a non-homogeneous LED chip. Since most LED's do have a lens on top, we placed an opal glass in front of the LED to determine the equation. However, we did the same procedure without opal glass, and it leads to the same homogeneous results. The equation without opal glass has different parameters because of the added lens on top of the LED.

Placing the SPR prism, the lens, and the light source according to this equation will lead to a homogeneous illumination of the prism surface. If the light is s-polarized, the whole surface is illuminated homogeneously. If the light is p-polarized, a gradient like the one shown in Figure 4.5appears. The reduction of the reflectivity is caused by the generation of surface plasmons, and the gradient of the reduction originates from the remaining divergence of the light beam. Combining this technology with a low noise current source creates a light source, which enables high-resolution SPR imaging.

Figure 4.7 shows the plot of the equation. While utilizing our method one must deal with four parameters, which are divergence, width of the homogeneous area perpendicular to the beam direction, width of the homogeneous region along the beam direction and distance between LED and homogeneous region.

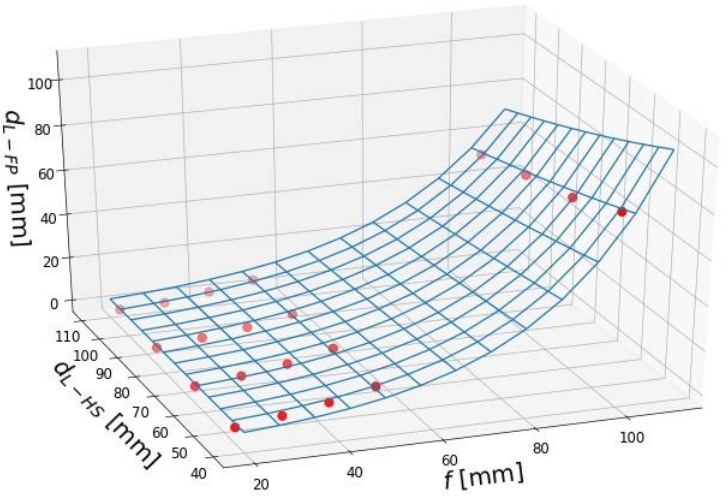

Figure 4.7: Plot of the equation, as a function of focal length and distance between lens and homogeneous surface; red dots are measurements conducted with the described setup.

One could use a lens with low *f*-value to achieve a short distance between H-region and LED, while doing so, the divergence will increase, and the spreading of the SPR-angle will be higher. On the other hand, one could use a high f-value to achieve a low divergence, this would increase the distance between H-region and LED. Therefore, one has to choose the best option for every task.

4.5 Conclusion

SPR-imaging was lacking cheap, large-area illuminating and homogeneous light sources. We described how to build a cheap, LED based light source, which is providing a homogeneous illumination over the entire sensing surface. The beam profile is homogeneous over a wide range along the beam direction and not only in one single plane. An empirical equation shows how to place lens and light source in relation to the sensitive area. We were able to reproduce the experiment many times and it is in use every day. However, the equation is not very exact and should therefore be understood as an approximation. The empirical equation is lacking a theoretical equation, thus more investigation must be done in this field.

However, the concept can already be used, and it enables high-resolution SPR-imaging on large surfaces. The light source was used for high RIU resolution experiments. Combined with a PCO Edge SCMOS camera we achieved resolutions in the 10^{-7} RIU range.

4.6 References

[1] Schasfoort, R., 2017. *Handbook of surface plasmon resonance*, Royal Society of Chemistry, London.

[2] Hausler, P., Roth, C., Vitzthumecker, T., Bierl, R. 2019 Miniaturized Surface Plasmon Resonance Based Sensor Systems—Opportunities and Challenges. In Optics, Photonics and Laser Technology 2018. Springer Series in Optical Sciences, Ribeiro, P., Raposo, M., Eds., Springer: Cham, Switzerland, Volume 223, pp. 169–195.

[3] Wang, D., 2019. *Recent Advances in Surface Plasmon Resonance Imaging Sensors*. Sensors, 19(6), S. 1266.

5. Nanoparticle Determination in Water by LED Excited Surface Plasmon Resonance Imaging

Abstract: The increasing popularity of nanoparticles in many applications has led to the fact that these persistent materials pollute our environment and threaten our health. A need of an online sensor system for monitoring the presence of nanoparticles in fresh water would be highly desired. We propose a label-free sensor based on SPR imaging. The sensitivity was enhanced by improving the detector by using a high-resolution camera. This revealed that also the light source needed to be improved, by using LED excitation instead of a laser light source. As a receptor different self-assembled monolayers have been screened. It can be shown that the nanoparticle receptor interaction is of a complex nature. The best system when taking sensitivity as well as reversibility into account is given by a dodecanethiol monolayer on the gold sensor surface. Lanthanide doped nanoparticles of 29 nm in diameter and with similar refractive index to the most common silica nanoparticles have been detected in water down to 1.5 µg mL^{-1}. This sensing concept is expected to be easily adapted for the detection of nanoparticles of different size, shape, and composition, and upon miniaturization, suitable for long-term applications to monitor the quality of water.

5.1 Introduction

Nanoparticles are coming more and more to an everyday material, as they find applications as catalyst in petroleum refining, as surface coating in displays and optical glasses, in paints, as smart fabrics with antimicrobial properties in textiles, for drug delivery in biomedicine, or in cosmetics. The most prominent nanoparticles are made from gold, silver, iron, lanthanides, TiO_2, and silica. The European Community reports a production of about 1.5 million tons per year for silica particles [1] and a mean concentration of 5.34 µg L^{-1} is predicted to be found in fresh surface water [2]. The potential risk of nanoparticle pollution is known for more than a decade. The sheer number of different nanoparticles [3] in addition to the prevalent use led to the assumption of possible health-related problems [4, 5]. In addition to that, no or only little information is available about the health risks of nanoparticles after their release to nature and potential subsequent degradation [3, 6]. A major problem, beside their complete removal, is the challenging detection of these small particles over a widespread area in complex media to identify the nanoparticle paths over their lifespan [5, 6]. This clearly demonstrates the need to develop sensors being able to detect those particles in the environment.

Surface plasmon resonance (SPR) might be a sufficient tool for this purpose. The excitation of surface plasmons on a gold surface deposited on a prism by a monochromatic light source is highly sensitive to changes in its surrounding environment [7-10]. Nanoparticles, which are large sized analytes, compared to other pollutants like chemicals or pharmaceutics, generate a larger signal change in SPR which allows to detect them at relative low levels [11-14] or use them as labels for signal enhancement [15,16]. The advantage to use an SPR imaging (SPRi) setup compared to a single channel SPR is the ability to easy functionalize the sensor surface by a variation of receptors,

enabling the determination of multiple analytes at once [17,18]. Reflectivity-based SPRi setups have been reported to resolve about 10^{-5} refractive index units (RIU) [19]. There were many tries to overcome this limit by developing advanced SPRi technologies like spectral SPRi or phase contrast SPRi [20]. However, these technologies all had disadvantages like a more complex setup, which impedes a widespread sensor implementation. The sensitivity of reflectivity-based SPRi can be enhanced by the implementation of a more sensitive and temperature stabilized camera of a high-resolution (16-bit and better) [21]. While having a more sensitive detector, the properties of the light source became more important. Point-based SPR is predominantly using lasers as a light source. This is since most semiconductor lasers are polarized and emit at a wavelength with a very narrow FWHM. Beside such an advantage laser light sources in SPR suffer from a spatial coherence that is generating diffraction patterns at every object within the light beam. Hence, every dust particle or every structure at the sensing surface will generate diffraction patterns. Moreover, the quality of the retrieved SPR image in prism coupled sensors is affected by the creation of speckles, which arise from the roughness at the interface of the glass to the metal layer, when it is in the range of the excitation wavelength or higher. Furthermore, semiconductor lasers lack on a temperature-dependent wavelength shift and they can even show mode hopping. To overcome those problems and enable the full potential of a high-resolution camera, the laser was exchanged with a high-power LED, which enables a homogenized intensity over the whole sensor surface and low noise [22]. To enable the required selectivity as well, the SPR prism was functionalized with differently capped alkanethiols, providing different surface charges, as receptor elements. Their low selectivity is ideal for an application in a cross-reactivity sensor system in the future, capable of detecting the huge variety of different nanoparticles. Lanthanide-doped yttrium fluoride particles have been chosen as model particles in this work. First, they belong to non-metallic particles, and therefore those cannot be easily detected by electrochemical stripping methods [5] which make them ideal candidates to demonstrate the power of SPR-based sensing. Second, those particles can be tailored very reproducibly regarding their size, with extremely narrow size distribution. Their refractive index of ~1.475 [23] is nearly identical to the widely applied silica nanoparticle (n_D = 1.475, [24]), which in contrast to the yttrium fluoride particles tend to form aggregates and therefore are not as ideal as model analyte particles. With this study we demonstrate the feasibility of reversible detection of the presence of nanoparticles in water by using an improved SPRi setup.

5.2 Materials and Methods

6-Amino-1-hexanethiol hydrochloride, 16-mercaptohexadecanoic acid (90%, w/w), 1 dodecanthiol (98%, w/w) and ethanol (absolute, >99.8%, w/w) were purchased from Sigma-Aldrich (Taufkirchen, Germany). NaCl salt (>99.5%, w/w), glucose (p.a.) and ethanol (p.a., ≥99.8%, w/w) were obtained from Carl Roth (Karlsruhe, Germany). The poly(dimethylsiloxane) (PDMS) stamp was fabricated using Sylgard 184 silicone elastomer base and curing agent by Dow Corning (Wiesbaden, Germany) in a ratio of 10:1 (v/v). All reagents were used without further purification. Double distilled water was used in all experiments.

Oleate coated core-shell nanoparticles $NaYF_4$(Yb,Er)@$NaYF_4$ were prepared by a protocol published recently [25] in a two-step approach. Firstly, core particles were synthesized from the rare earth trichlorides in high boiling solvents with 78% YCl_3, 20% $YbCl_3$ and 2% $ErCl_3$. Cubic $NaYF_4$ particles were used to grow shell around the core particles by a stepwise injection of the cubic particles to a boiling dispersion of the hexagonal particles. The oleate coating of the core-shell nanoparticles $NaYF_4$(Yb,Er)@$NaYF_4$ was exchanged by BF_4^- [26] and the BF_4^- coated nanoparticles were dispersed in H_2O. The concentration was determined by inductively coupled plasma optical emission spectrometry with a Spectro Flame-EOP (Kleve, Germany).

A commercially available BioSuplar SPR 521i instrument (Mivitec GmbH, Sinzing, Germany) was used, equipped with an F1-65 glass prism installed on a swivel carriage. F1 Gold coated glass slides (20 × 20 mm) were obtained from Mivitec GmbH (Sinzing, Germany).

The homemade SPRi setup was built with a V-shaped light path with fixed arms and a movable middle edge on a linear stage, to adjust the measurement angle (step size 0.001°). An OSLON SQUARE 660 nm LED was purchased from Osram GmbH (Berlin, Germany). The LED was driven by a 2636B SourceMeter by Keithley (Cologne, Germany) at a current of 10 mA. Further implemented optical components were an *f*40 aspheric plastic lens and a 1:9,000 ratio polarizer, from Edmund Optics (York, United Kingdom) and a 2 nm bandwidth filter. The laser reference measurements were performed using a 660 nm, 75 mW MiniLas from RGB Lasersystems (Kelheim, Germany), which was run at a power of 10 mW. The image is acquired by a 16-bit sCMOS Camera Edge 4.2 from PCO AG (Kelheim, Germany).

Schott F2 glass prisms were installed to this setup. Before usage, the prism surface was polished to grade P4, an approximately 1 nm chromium adhesive layer and an approximately 50 nm gold layer was deposited on top by electron beam deposition.

The microfluidics consisted of a micro pump, purchased from Bartels Mikrotechnik GmbH (Dortmund, Germany) and a custom-made microfluidic chip, made of stainless steel.

The refractive index of the solutions was determined with a DR6300-T refractometer from Krüss (Hamburg, Germany). Dynamic light scattering and zeta potential measurements have been performed with a Nano ZS from Malvern (Worcestershire, UK) at 20 °C. Transmission electron microscopy (TEM) was used to estimate the nanoparticle size. Samples on carbon coated copper grids (400 mesh) have been investigated by a 120 kV Philips CM12 microscope (FEI, Munich, Germany).

The gold-coated glass slide or prism was functionalized with the respective alkanethiol monolayer by self-assembly, using 200 µM alkanethiol solution in ethanol. A structured self-assembled monolayer was obtained by micro contact printing with a PDMS-stamp of a squared structure.

Before measurement, the SPR prism or slide was cleaned with ethanol and dried under nitrogen flow. A stable SPR signal was obtained after flowing degassed water for about one hour. Each nanoparticle solution was cycled over the surface for six minutes. Next, degassed water was applied to the surface to remove excess of nanoparticles from the slide. All steps were performed at a

constant flow rate of 0.2 mL min^{-1}. After the highest nanoparticle concentration was applied, the slide was extensively washed, at a flow rate of 0.4 mL min-1, until the signal intensity was back to its original level. At last, the SPR signal was calibrated to RIU with NaCl solutions of known refractive index.

5.3 Results

In SPR imaging the sensitivity mostly is influenced by the choice of a proper light source and by a camera system with a high resolution. The wavelength sensitivity of the SPR signal demands a nearly monochromatic, wavelength-stabilized light source. Typical monochromatic, polarized light sources are lasers. However, lasers do have spatial coherence, which is causing speckles at rough surfaces and interference patterns at every dust particle and edges of optical components in its light path [11]. Hence, an LED-based light source was implemented to overcome those limitations. The optimized setup uses a 16-bit camera which yields a relative signal change of 1,545 counts by measuring two aqueous reference solutions with a refractive index change of $1.2 \cdot 10^{-4}$ RIU, which equals a resolution of $7.8 \cdot 10^{-8}$ RIU per count. When considering the signal's standard deviation (3σ) of 2.36 during 3 min measurement time, a sensitivity of $5.5 \cdot 10^{-7}$ RIU can be achieved.

Such a low limit of detection enables SPRi as a sensing tool for the label-free detection of nanoparticles in water samples. To prove this lanthanide-doped yttrium fluoride particles have been studied in this work. The reason to choose those is due to the possibility to synthesize them in controlled size with high uniformity demonstrated by a low polydispersity, which allows one in a more comfortable way to calculate concentrations. These particles have a surface that is known to be highly attractive to negatively charged ligands, which saturate vacancies at the nanoparticle interface. As surface ligand BF_4^- was chosen which increases their dispersibility in water. The nanoparticles have a size of 29 ± 2 nm, estimated by averaging the diameter of 3,603 particles from transmission electron micrographs. This size was chosen as a perfect average size as most nanoparticles in practical applications currently are in a range from 10 to 50 nm in diameter. The zeta-potential of those particles, measured at a concentration of 12.1 ± 0.2 mg mL^{-1} in water is 3.63 ± 0.09 mV, which is close to neutral, expecting that electrostatic interaction will not be the main force for binding to any surface.

To enable controllable interaction of the nanoparticles with the sensor surface a suitable surface modification must be found. Besides the surface coating, but according to the zeta-potential, their affinity was highest to the bare gold surface and a dodecanethiol modified gold surface, with a neutral surface charge (Figure 5.1).

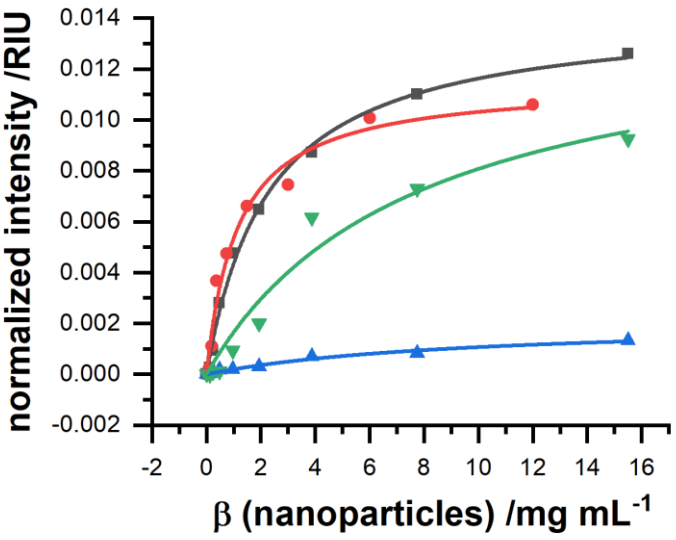

Figure 5.1: Dose-response curves of nanoparticles measured by a point-based SPR setup (N = 1). The gold slides were functionalized by a self-assembled monolayer of dodecanethiol (red), 16 mercapto¬hexadecanoic acid (green) or aminohexanethiol (blue). The signal response to a non-modified, blank gold slide (black) is shown as a reference. The data have been fit by a Langmuir isotherm.

Thereby, the overall binding capacity was higher for blank gold, but the affinity was superior towards the self-assembled monolayer. The binding constants for all surface modifications are summarized in Table 5.1. In comparison, if surface charges are applied, negative via a coating of 16 mercaptohexadecanoic acid and positive via a coating of 6 aminohexanethiol, the binding performance was severely decreased. A negative surface charge decreases binding affinity but still enables a relatively high binding capacity, whereas a positive surface charge decreases both to a minimum.

Table 5.1: Binding constants of the different self-assembled monolayer modified SPR surfaces and a blank gold surface to nanoparticles from the NaYF4 type. A Langmuir isotherm was applied for fitting.

Surface	K_d [mg mL^{-1}]	K_a [mg^{-1} mL]	S_{max} [10^{-3} RIU]
blank	2.2 ± 0.2	0.44 ± 0.04	14.3 ± 0.4
dodecanethiol	1.1 ± 0.2	0.9 ± 0.2	11.5 ± 0.7
16-mercaptohexadec-anoic acid	7.7 ± 3	0.13 ± 0.05	14 ± 3
6-aminohexanethiol	9.6 ± 3	0.10 ± 0.03	2.1 ± 0.3

The order of the different binding affinities cannot be explained by electrostatic interactions between the sensor surface and the nanoparticle only. Here one would expect that amino-functionalized surface would lead to a good binding. Indeed, binding can be found but the other surfaces are superior. For surfaces with carboxy functionality at the surface, the particles show a better adsorption behavior as their surface consists of lanthanide ions which do form a stable coordinative binding to carboxy groups, which has been reviewed by Wolfbeis *et al.* [27]. Surprisingly also dodecanethiol was able to bind the nanoparticles. This finding is interesting as it suggests that the surface modification of those particles performed by ligand exchange, where oleate molecules at the particle surface get stripped off does result in a complete loss of the original

surface capping. The reason for the binding might be that still some oleate is present at the particle surface which interacts by intercalation of the long hydrophobic tail of the oleate with the long hydrophobic chain of the dodecanethiol. To get better insight in nanoparticle surface interaction is currently under investigation and out of scope of this work. It seems reasonable to continue with the dodecanthiol coating in further measurements. Figure 5.2 shows a typical measurement sequence. After each binding step, a short washing step was applied to exclude the unbound particles from the SPR signal. The particles show a high overall signal change, which is due to their high mass and size.

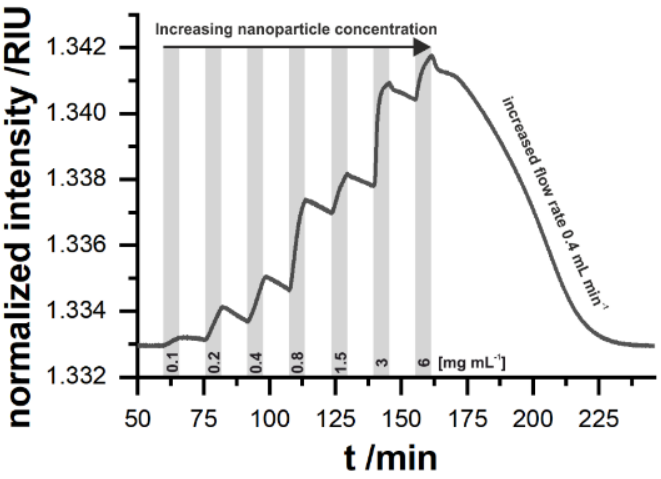

Figure 5.2: Time course of a SPR measurement sequence. The grey areas indicate the presence of nanoparticles in the measurement solution, whereas in the white areas the system was rinsed with water. In the first part until t = 160 min, a flow rate of 0.2 mL min 1 was applied, which was then increased to 0.4 mL min 1. The gold surface was modified by a dodecanethiol monolayer.

For an online sensing system of environmental samples like freshwater reversibility is one of the key requirements. Gold slides modified with a dodecanethiol monolayer can achieve this. SPR measurements at a flow rate of 0.2 mL min^{-1} allow to easily discriminate the presence of 0.1 mg mL^{-1} nanoparticles in water. In contrast to changes in the bulk refractive index, the slope in the change of the signal change is concentration dependent, which also indicates that the particles adsorb to the surface by a weak interaction. The desorption at the same low rate is somehow slower compared to the absorption of the particles to the surface. When doubling the flow rate, the sensor surface can be regenerated within about one hour. This would be attractive for stop flow sensing systems, which would be able to get one data point in less than 1.5 hours. Such a behavior is beneficial for a long-term continuous sensor since a high signal response can be obtained and the adsorption is faster than the desorption which makes a regeneration step expendable. An optimization of the microfluidic flow cell together with the flow rate is expected to improve the sample rate, but this is out of scope of this study. The discrimination of the signal change caused by fluctuations in the refractive index of the media itself and the presence of nanoparticles can be achieved by exploiting the binding behavior of different surface modifications together with pattern analysis. This demands to use sensor arrays and SPR imaging.

SPR imaging relying on an LED and a camera shows the characteristic of an angle shift over the image in x-direction, which was observable during this measurement (Figure 5.3). This behavior

would exclude certain regions to be used for signal generation if the whole imaging surface area should be used for only one receptor. But this would contravene the potential of SPRi. If multiple receptors are used in SPRi, this circumstance can be even useful. Each recognition element has a different SPR angle as seen for dodecanethiol and aminohexanethiol in Figure 5.3 c. The angle shift can be exploited to place both receptors in a region where the complete linear intensity range from minimum to total internal reflection can be used.

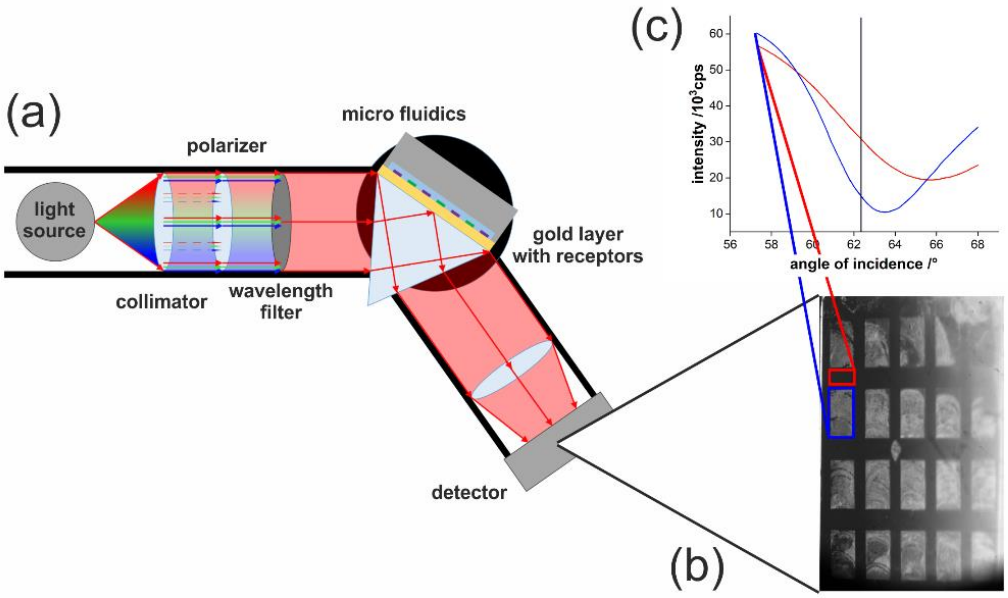

Figure 5.3: a) Scheme of the SPRi setup. b) SPR image obtained coated with dodecanethiol squares (blue) surrounded by aminohexanethiole (red). The irregular coating is caused by the stamping procedure to form a patterned surface. c) SPR curves from the two respective thiols.

SPR imaging is needed to further minimize the detection limit as well. The association curves measured by a commercially available SPR device, shown in Figure 5.4, feature a limit of detection of 29 ± 9 µg mL^{-1}, which still is too high for a practical application. In contrast to this, the optimized home built SPRi system with an LED light source was able to improve the limit of detection under identical measurement conditions already by a factor of 20 (Figure 5.4). It should be said, that due to measurement there was a loss of the nanoparticles of around 50% after multiple measurement cycles, due to experimental limitations, which were both identical for both measurements systems. For a fair comparison, the limit of detection was calculated based on the initially by ICP measurements estimated concentration of the nanoparticle applied to each system without prior application.

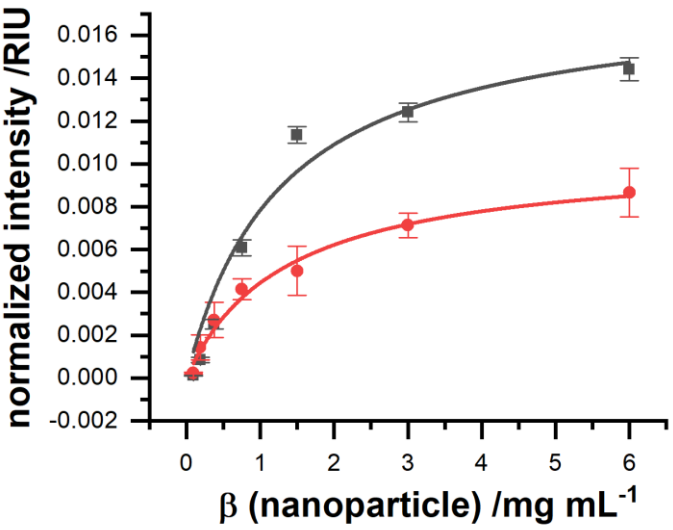

Figure 5.4: Dose-response curve of NaYF4-based nanoparticles measured by a point-based SPR setup (red) and an SPR imaging setup with LED illumination (black) (N = 4).

Detailed analysis retrieved that the dissociation constant stayed the same, but aside from that, the binding capacity was increased, (Table 5. 2), leading to limit of detection (LOD) of 1.5 µg mL^{-1}. In contrast to a point based SPR, where the signal is averaged from the whole illuminated area on the gold, the imaging setup allows to select only those pixels on the camera image which are best suited in terms of sensitivity and noise due to irregularities and artifacts such as small air bubbles which get stuck over time when analyzing real samples.

*Table 5. 2 LODs and binding constants of the point based SPR and the optimized SPRi setup of NaYF4 nanoparticle on a 1-dodecanethiol coated surface. A Langmuir isotherm was applied for fitting. *Values differs from that in Table 5.1, due to another batch of similar produced nanoparticles was used.*

Setup	LOD [µg mL^{-1}]	K_d [mg mL^{-1}]	S_{max} [10^{-3} RIU]
Point based SPR	29 ± 9	1.3 ± 0.2*	10.4 ± 0.6*
SPR imaging	1.5 ± 0.7	1.3 ± 0.4	17.9 ± 0.6

5.4 Discussion

In this work we demonstrated that the major drawback of reflectivity based SPRi – its insufficient sensitivity – can be overcome by improving the camera system for detection as well as the light source. For further development such a system is capable for miniaturization and therefore for a wide range of sensing applications. The spreading of the angle of incidence in one direction of the image collected by LED-based SPRi is not necessarily a drawback as it enables the simultaneous use of different angles of incidence (in a range of up to 3° in our setup) within one sensor chip, without the utilization of any moving component. This allows to place every receptor with its individual refractive index to be placed at its most sensitive angle position. Temperature drift and fluctuations in the light source can be overcome by using internal reference spots placed on the gold slide. This work is currently under investigation.

By the modification of the sensor surface with different self-assembled monolayers it became apparent that the interaction of nanoparticles with a sensor surface is of complex nature as nanoparticles will be coated by additional surface ligands. Therefore, sensor arrays with cross-reactivity receptors are suggested to tackle this challenge by pattern recognition. Surface plasmon resonance imaging might be capable of handling this mix of different particles since it can measure multiple analytes simultaneously. This is possible by the combination of suitable receptors. Thereby, the key will not be to find the most selective receptor for each particle, but to find a smart combination of low selective receptors, which can detect particles by their specific signal pattern. Using LED-based SPRi for this approach, each receptor can be positioned at the angle of highest sensitivity, due to the tunable angle shift. The limit of detection still needs to be improved when applications in quality control of environmental samples are envisioned.

5.5 References

[1] European Commision. 2012 *Types and Uses of Nanomaterials, Including Safety Aspects*; European Commission: Brussels, Belgium.

[2] Giese, B., Klaessig, F., Park, B., Kaegi, R., Steinfeldt, M., Wigger, H., von Gleich, A., Gottschalk, F. 2018 Risks, Release and Concentrations of Engineered Nanomaterial in the Environment. Sci. Rep., 8, 1565.

[3] Botta, C., Labille, J., Auffan, M., Borschneck, D., Miche, H., Cabié, M., Masion, A., Rose, J., Bottero, J.Y. 2011 *TiO2-based nanoparticles released in water from commercialized sunscreens in a life-cycle perspective: Structures and quantities*. Environ. Pollut., 159, 1543–1550.

[4] Blinova, I., Ivask, A., Heinlaan, M., Mortimer, M., Kahru, A. 2010 *Ecotoxicity of nanoparticles of CuO and ZnO in natural water*. Environ. Pollut., 158, 41.

[5] Gao, Y., Yang, T., Jin, J. 2015 *Nanoparticle pollution and associated increasing potential risks on environment and human health: A case study of China*. Environ. Sci. Pollut. Res., 22, 19297.

[6] Troester, M., Brauch, H.-J., Hofmann, T. 2016 *Vulnerability of drinking water supplies to engineered nanoparticles*. Water Res., 96, 25.

[7] Zhang, M., Yang, J., Cai, Z., Feng, Y., Wang, Y., Zhang, D., Pan, X. 2019 *Detection of engineered nanoparticles in aquatic environments: Current status and challenges in enrichment, separation, and analysis*. Environ. Sci. Nano, 6, 709.

[8] Pollard, M.R., Sparnacci, K., Wacker, L.J., Kerdoncuff, H. 2020 *Polymer nanoparticle identification and concentration measurement using fiber-enhanced Raman spectroscopy*. Chemosensors, 8, 21.

[9] Neves, M.M., Nouws, H.P., Delerue-Matos, C., Martín-Yerga, D. 2020 *Electrochemical detection and characterization of nanoparticles: A potential tool for environmental purposes*. Curr. Opin. Electrochem., 22, 58.

[10] Homola, J., Yee, S.S., Gauglitz, G. 1999 *Surface plasmon resonance sensors*. Sens. Actuator B Chem., 54, 3.

[11] Nguyen, H.H., Park, J., Kang, S., Kim, M. 2015 *Surface plasmon resonance: A versatile technique for biosensor applications*. Sensors, 15, 10481–10510.

[12] Amirjani, A., Rahbarimehr, E. 2021 *Recent advances in functionalization of plasmonic nanostructures for optical sensing.* Microchim. Acta, 188, 1.

[13] Masson, J.F. 2020 *Portable and field-deployed surface plasmon resonance and plasmonic sensors*. Analyst, 145, 3776.

[14] Nizamov, S., Scherbahn, V., Mirsky, V.M. 2016 *Detection and quantification of single engineered nanoparticles in complex samples using template matching in wide-field surface plasmon microscopy*. Anal. Chem., 88, 10206–10214.

[15] Scherbahn, V., Nizamov, S., Mirsky, V.M. 2016 *Plasmonic detection and visualization of directed adsorption of charged single nanoparticles to patterned surfaces*. Microchim. Acta, 183, 2837.

[16] Jiang, D., Chen, H.B., Qian, C., Zhou, X.L., Liu, X.W. 2021 *Determining the Aggregation Kinetics of Nanoparticles by Single Nanoparticle Counting*. ACS EST Water, 1, 672.

[17] Kuzmichev, A., Skolnik, J., Zybin, A., Hergenröder, R. 2018 *Absolute analysis of nanoparticle suspension with surface plasmon microscopy*. Anal. Chem., 90, 10732.

[18] Grzéskowiak, B.F., Túsnio, K., Wózniak, A., Szalata, M., Lipínski, D., Jurga, S., Słomski, R. 2019 *Transgenic Plant Detection Using an AuNPs Based SPR Biosensor*. Biosensors, 9, 116.

[19] Fenzl, C., Hirsch, T., Baeumner, A.J. 2015 *Liposomes with high refractive index encapsulants as tunable signal amplification tools in surface plasmon resonance spectroscopy*. Anal. Chem., 87, 11157.

[20] Fournel, A., Mantel, M., Pinger, M., Manesse, C., Dubreuil, R., Herrier, C., Rousselle, T., Livache, T., Bensafi, M. 2020 *An experimental investigation comparing a surface plasmon resonance imaging-based artificial nose with natural olfaction*. Sens. Actuator B Chem., 320, 128342.

[21] Maho, P., Herrier, C., Livache, T., Rolland, G., Comon, P., Barthelme, S. 2020 *Reliable chiral recognition with an optoelectronic nose*. Biosens. Bioelectron., 159, 112183.

[22] Wang, D., Loo, J.F.C., Chen, J., Yam, Y., Chen, S.-C., He, H., Kong, S.K., Ho, H.P. 2019 *Recent Advances in Surface Plasmon Resonance Imaging Sensors*. Sensors, 19, 1266.

[23] Wong, C.L., Olivo, M. 2014 *Surface Plasmon Resonance Imaging Sensors: A Review*. Plasmonics, 9, 809–824.

[24] Hausler, P., Roth, C., Vitzthumecker, T., Bierl, R. 2019 *Miniaturized Surface Plasmon Resonance Based Sensor Systems—Opportunities and Challenges.* In Optics, Photonics and Laser Technology 2018. Springer Series in Optical Sciences, Ribeiro, P., Raposo, M., Eds., Springer: Cham, Switzerland, Volume 223, pp. 169–195.

[25] Hausler, P., Jobst, S., Fischer, J., Roth, C., Bierl, R. 2021 *Homogeneous Light Source for Surface Plasmon Resonance Imaging*. In Proceedings of the 8th International Conference on Photonics, Optics and Laser Technology (PHOTOPTICS 2020), 1st ed., Albella, P., Raposo, M., Andrews, D., Ribeiro, P., Eds., Scitepress: Sebútal, Portugal, pp. 163–167.

[26] Sokolova, V.I., Zvyagina, A.V., Igumnovb, S.M., Molchanovaa, S.I., Nazarova, M.M., Nechaevc, A.V., Savelyeva, A.G., Tyutyunovb, A.A., Khaydukova, E.V., Panchenko, V.Y. 2014 *Determination of the Refractive Index of β-$NaYF_4/Yb^{3+}/Er^{3+}/Tm^{3+}$ Nanocrystals Using Spectroscopic Refractometry*. Opt. Spectrosc., 118, 609.

[27] Khlebtsov, B.N., Khanadeev, V.A., Khlebtsov, N.G. 2008 *Determination of the Size, Concentration, and Refractive Index of Silica Nanoparticles from Turbidity Spectra*. Langmuir, 24, 8964.

[28] Märkl, S., Schroter, A., Hirsch, T. 2020 *Small and Bright Water-Protected Upconversion Nanoparticles with Long-Time Stability in Complex, Aqueous Media by Phospholipid Membrane Coating*. Nano Lett., 20, 8620.

[29] Himmelstoß, S.F., Hirsch, T. 2019 *Long-term Colloidal and Chemical Stability in Aqueous Media of $NaYF_4$–Type Upconversion Nanoparticles Modified by Ligand-Exchange*. Part. Part. Syst. Charact., 36, 1900235.

[30] Muhr, V., Wilhelm, S., Hirsch, T., Wolfbeis, O.S. 2014 *Upconversion nanoparticles: From hydrophobic to hydrophilic surfaces*. Acc. Chem. Res., 47, 3481–3493.

[31] Genslein, C., Hausler, P., Kirchner, E.M., Bierl, R., Baeumner, A.J., Hirsch, T. 2016 *Graphene-enhanced plasmonic nanohole arrays for environmental sensing in aqueous samples*. Beilstein J. Nanotechnol., 7, 1564.

[32] Couture, M., Live, L.S., Dhawan, A., Masson, J.F. 2012 *EOT or Kretschmann configuration? Comparative study of the plasmonic modes in gold nanohole arrays*. Analyst, 137, 4162.

6. Drift correction of SPR signals by improved sensor surfaces

6.1 Introduction

The temperature strongly influences the refractive index of the majority of chemical compounds. Therefore, to compensate for temperature fluctuations, SPR sensors must maintain the analyte matrix and SPR prism at a constant temperature. This becomes increasingly difficult with greater sensor sensitivity. Therefore, large laboratory equipment typically stabilizes the temperature of both the analyte matrix and the SPR prism. This is very complicated, takes up a lot of space, and is costly. Therefore, this method is not suitable for stabilizing signals in low-cost, miniaturized sensors. Consequently, a new technology must be developed to compensate for temperature changes and stabilize a miniaturized SPR sensor.

Semiconductor devices like LEDs and cameras are impacted by temperature which affects their performance [1,2]. Furthermore, these devices undergo aging. These effects lead to undesired SPR measurement drift. Various established solutions exist to address the issues caused by these well-known effects in numerous settings. One example is integrating photodiodes into laser diode housings to compensate for changes in intensity. Another common method is incorporating a bypass into the system to separate a portion of the light and measure any resulting fluctuations. These approaches have the limitations that they only monitor a portion of the system, leaving the detector mostly unmonitored. Implementing a bypass would require additional design effort and introduce another source of error and cost into the system, as well as potentially increase its size. Consequently, the development of new technology is necessary to stabilize a miniaturized system against ageing and environmental influences.

6.2 Methods

Experiments in this chapter utilized sweet almond oil as the base oil. The alteration in refractive index was achieved by adding oil with a different refractive index, as seen in Table 6.1. The analyte was transported using an Ismatec peristaltic pump (ISM935C), while a B. Braun valve bank (Discofix C, PZN:02733592) was employed to switch between different analytes. B. Braun Luer-Lock adapters (Combifix Adapter, PZN:6866999) were used to convert the male connectors of the valve bank into female connectors. The Luer-Lock connectors were connected to the tubing using Vieweg full metal dispensing tips (Art. No.: 501543), which were made of stainless steel and had an inner diameter of 2 mm. To connect the fluidic components, a transparent polyurethane hose (Sang-A PD2110400002) having an inner diameter of 2 mm was employed. The use of a transparent tube is advantageous for air bubble detection. Silicone hoses were found to be unsuitable as they allow diffusion of oil and air. Tygon hoses are not recommended for use, as they harden when exposed to mineral oil. In order to ensure the protection of the oil during storage, samples were placed in a wide-mouth amber glass jar of GL55 designation. The jar's lid has a hole corresponding to the tube's outer diameter, creating a secure seal. Throughout the experiments, the lid was slightly opened to prevent negative pressure.

Table 6.1: Refractive index of natural oils. The refractive index was determined with a Krüss DR6300T at a temperature of 23°C.

Oil grade	Refractive index	Manufacturer
Cinnamon	1,5337	Naissance
Tung	1,5185	Bindulin-Werk
Basil	1,5051	Naissance
Cedarwood oil	1,5050	Wesentlich.
Flaxseed	1,4801	Naissance
Sweet Almond	1,4725	Naissance
Baobab	1,4684	Naissance
Coconut Fractionated	1,4480	Naissance

A Schott N-SF6 glass prism with an angle of 62 degrees, a base of 18 × 18 mm, and a height of 8 mm was utilized. The glass has the highest stain and climate resistance classification as per the Schott glass catalog [3]. A Filmetrics F2T was used to measure the thickness of the applied metal coating.

In addition, a Veeco (Bruker) Dimension Icon AFM with TESPA-V2 tips was used to evaluate the surface of the uncoated prisms. The device was provided by Professor Weiss's working group in the Physics department at the University of Regensburg. Surface roughness in the single-digit nanometer range was quantified. Before coating, the prisms underwent a cleaning process. using Thorlabs MC-50E lens cleaning paper. To strip the materials, we used acetone (Carl Roth, ROTISOLV), isopropanol (Carl Roth, ROTISOLV), deionized water (from cleanroom infrastructure), and ethanol (Carl Roth, ROTISOLV) in the listed sequence.

The wavelength 660 nm is extensively utilized in SPR technology due to the convenient availability of semiconductor lasers in this range. However, for the present devices, the wavelength 730 nm was employed. Since LEDs of this wavelength are frequently utilized in horticultural technology, they are cost-effective, powerful, and come in a variety of radiation angles. The construction of the light source followed the instructions given in Chapter 3, using an Osram OSLON LED that emits light at 730 nm. To minimize temperature-dependent changes in the refractive index of the glass (Figure 6.1), the glass and wavelength were carefully matched.

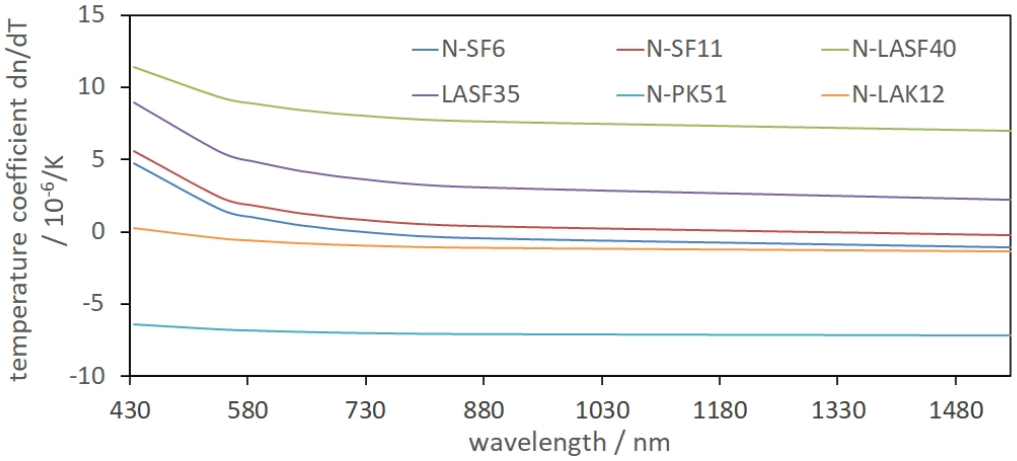

Figure 6.1: Comparison of different types of optical glass by the wavelength dependent temperature coefficient. The graphs are calculated according to [4] with the data from the individual Schott glass datasheet.

The gold mirrors were fabricated through electron beam evaporation with the use of a shadow mask for structuring. Due to the fragility of the thin gold layer, a metal mask was not feasible as it could cause damage. Additionally, a plastic foil mask was not suitable as it tends to curl, resulting in a gap between the mask and the surface, which is not acceptable for precise structures. Protective films, which are familiar from smartphones, can adhere to the display without the need for adhesives and can be removed without leaving any residue behind. These films have proven to produce satisfactory results. In this study, protective films, similar to those used in smartphones, were structured and used as a shadow mask to create mirror references. Ecultor produced the foils based on the provided drawings. The specific film type selected for this study was "Crystalclear". It has a thickness of 100 µm with a 20 µm thick silicone adhesion layer.

The capsules used for liquid refractive index references underwent the same manufacturing process as the seals for the flow cells. Wacker Semicosil 986/1k silicone was applied using a Musashi Shot mini 200SX dispenser and a 0.64 mm needle. To enhance the aspect ratio between extruded width and layer height, the seals and capsules were applied in multiple layers. Once the silicone cured, the reference liquid was dropped into the capsule, and the flow cell was pressed against the prism and installed in the measurement device.

The flow cell consists of a brass block and the SPR prism separated by a silicone seal. In order to evenly distribute the analyte over the sensor surface, the brass block features a row of 1 mm holes located at the top and bottom. The holes are supplied via a 2 mm inner diameter hole. To ensure good thermal conductivity, the body of the flow cell (No. 5) in Figure 6.2 is made of metal. A Peltier element (No. 6) is situated at the rear of the flow cell for regulating its temperature during experiments.

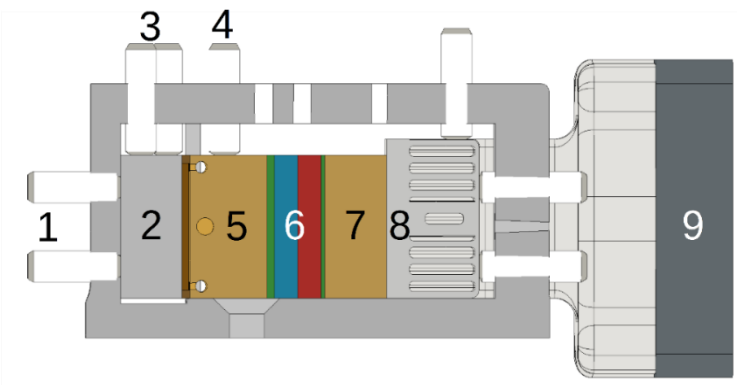

Figure 6.2: A cross section of a SPRi-prism mount. Here the prism mount is equipped with one possible configuration, to show its options. The screws at the left side (1) can be used to adjust the tilt of the prism (2) along the light path and to place the gold surface at the center of the hinge. The three screws at the left side of the top (3) can be used to adjust the tilt of the prism and to fix the prism in its place. The screws at the middle of the top (4) are to fix the fluid cell (5). There are some more threads which can be used to fix optional components. The screws at the right side are used to couple components like a Peltier Element (6), a spacer (7) and a heat sink (8), which is equipped with a fan (9).

Simulation in this study employed WINSPALL 3.02. The refractive index of the analyte (Table 6.1) was determined using a Krüss DR6300T. The glass refractive index was calculated using the Sellmeier equation and Schott data sheet. The refractive index of the gold layer was obtained from literature.

6.3 Results

6.3.1 Fabrication of References

Despite the implemented cleaning procedure, the prisms that previously looked clean displayed various small imperfections in the SPR image. Upon thermal treatment, bubbles emerged beneath the gold layer (Figure 6.3), with their appearance starting at around 100°C and becoming more pronounced at 400°C.

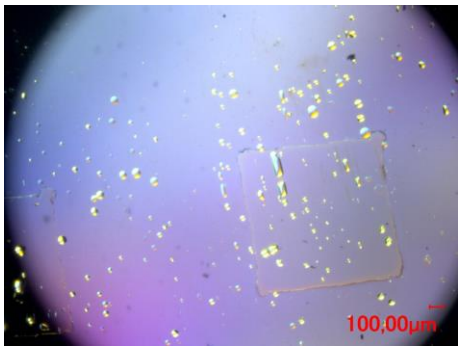

Figure 6.3: Gold film with bubbles, after baking. There are also elongated structures that run parallel. This indicates defects from the polishing process. The squared structure is a mirror reference made of gold.

Cleaning prisms in an ultrasonic bath with acetone prior to coating and cleaning processes can prevent bubbles from appearing when heated. It is possible that the smallest defects caused by polishing were filled with polishing paste, making them undetectable by the AFM. The presence of elongated bubbles in a parallel formation indicates that they are defects created during the polishing process. No further investigation was conducted on the defects since none were found after completing the entire cleaning process.

The surface of the prism designated for gold coating has been polished to grade 4 as stated in DIN ISO 10110-8. This resulted in a surface roughness of less than 1 nm. Specific details can be found in the standard document. AFM analysis was performed to measure the roughness of the prisms prior to cleaning. Figure 6.4 illustrates a 10 µm x 10 µm area of the polished glass Prism surface.

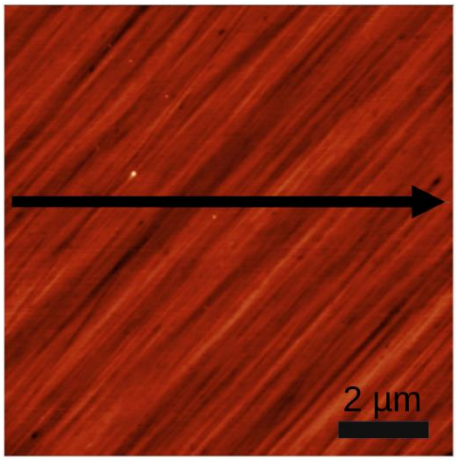

Figure 6.4: AFM image of the uncleaned and uncoated prism surface. The roughness of the surface is less than 1 nm. The grinding marks from the polishing process are clearly visible. The image was recorded with a Veeco (Bruker) Dimension Icon AFM and a TESPA-V2 tip. The image area is 10 µm x 10µm.

The grinding marks observed in Figure 6.4 support the hypothesis that residual small amounts of polishing paste are still present in slightly deeper polishing trenches. Although much deeper trenches were not detected on the AFM images, as shown by Figure 6.5, there are several plausible reasons for this. One possibility is that these trenches are concealed to the AFM by residues of the polishing paste. Alternatively, since the defect separation ranges from several hundred micrometers to millimeters, while the AFM images' field of view is only 10 µm wide, it can be difficult to locate the defects with the AFM.

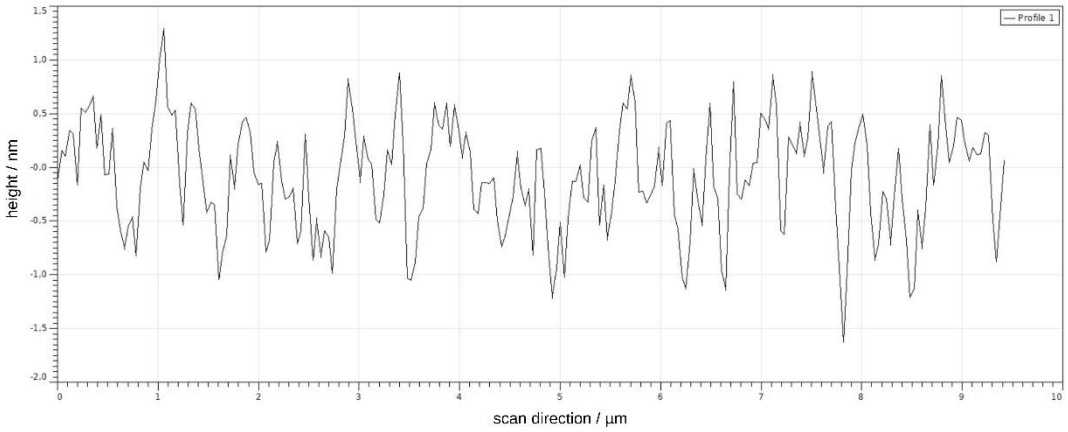

Figure 6.5: The figure shows the cross section of Figure 5.4 along the black arrow. The RMS roughness is below 1 nm. Since the thickness of the chromium adhesion layer is only 2 nm and the SPR effect is already very sensitive to small changes in thickness in the metal layer, it is important to ensure that the prism surface has a low roughness.

The refractive index of most materials is temperature dependent. However, in some cases, this dependence can be avoided. Schott's TIE-19 explains the extent of the refractive index dependence on temperature as a function of wavelength. Figure 6.1 depicts the change in refractive index per Kelvin as a function of wavelength.

For the Schott N-SF6 glass, the refractive index at a wavelength of 730 nm remains constant regardless of temperature. Consequently, it is feasible to minimize the temperature dependence of the system. The temperature of the ambient or system presently solely affects the analyte and not the SPR prism.

Figure 6.6 displays a foil mask under a transmitted light microscope subsequent to its use in creating a mirrored reference. The edges of the structures appear somewhat uneven, displaying slight waves. Stitching is visible in the corners akin to that seen on CNC workpieces. Overall, these irregularities are insignificant when considering the total reference area and have no impact on the function.

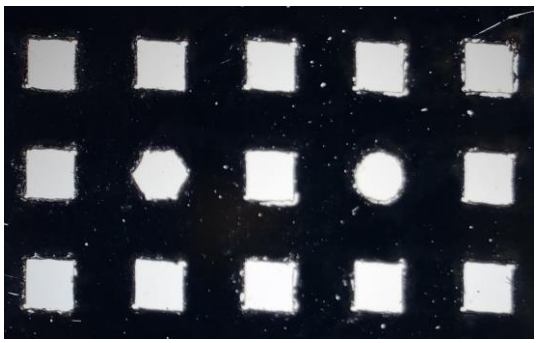

Figure 6.6: Microscope image of a shadow mask. The squares are 1 mm x 1 mm. To facilitate the orientation of an AI during a later evaluation, a hexagon and a circle were also integrated into the mask.

The implementation of orientation markers is essential for performing Artificial Intelligence (AI) assisted position corrections on image data or for recording receptor positions during coating. As illustrated in Figure 6.6, the mask enables the production of hexagons, squares, and circles that can serve as orientation markers.

The refractive index of a gold layer is influenced by several factors, including purity, density, and the method of manufacture. Consequently, obtaining data that accurately reflects reality can be challenging. Numerous values for the refractive index of gold have been measured and published in literature. A graphical representation of the refractive index of gold as a function of film thickness is shown in Figure 6.7.

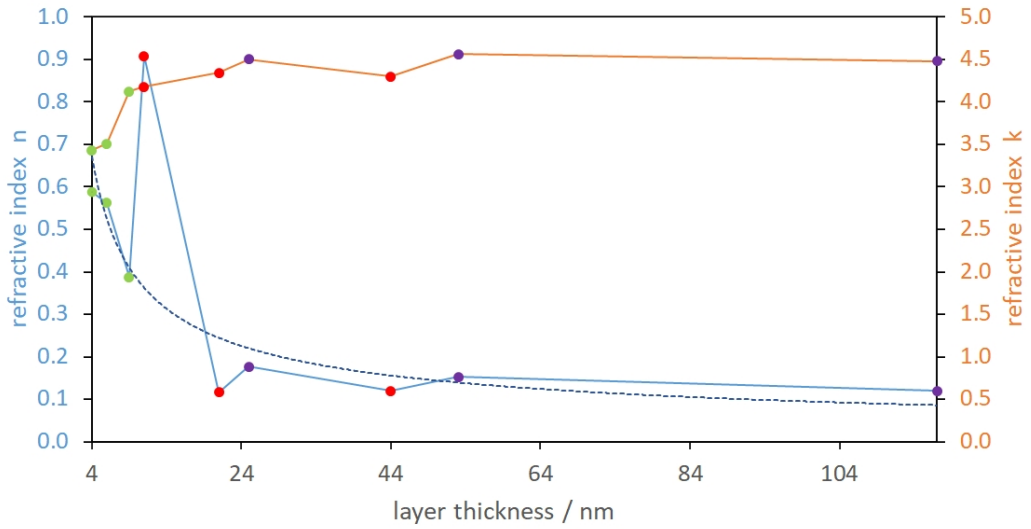

Figure 6.7: Refractive index of gold at 730 nm vs. the thickness of the gold layer. The refractive index of a thin gold layers is also depending on the method of fabrication and the underlying substrate. Therefore, thin gold layers have a quasi-refractive-index, which is changing with its thickness. The blue line shows the refractive real part of the refractive index, while the orange line shows the imaginary part of the refractive index. Yakubovsky [5] measured in 2019 the green dots, the gold was e-beam evaporated on top of a MoS2 layer on a SiO2 substrate. The red dots were published by Rosenblatt in 2020 [6], the gold was thermal evaporated on top of a fused silica prism with a mono layer coating of (3 mercaptopropyl)trimethoxysilan. Yakubovsky [7] measured the purple dots, the gold was e-beam evaporated on top of a silicon wafer with a native oxide layer of 1.5 nm. The results of the publications are listed at [https://refractiveindex.info/], the website provides a transformation of measurements to other wavelength, and it is also listing other materials.

6.3.2 Referencing Mirrors

To monitor the entire system, it is necessary to guide the reference beam with the measuring beam from the light source to the detector. This can be achieved by applying a fully reflective area on the SPR-sensitive gold layer that does not exhibit a significant SPR effect. By adding fully reflective mirrors to the sensor surface, camera and light source drift can be compensated. This new method does not require any additional discrete components.

Gold layers with a thickness of 150 nm or greater are commonly utilized in many semiconductor processes. If a layer of gold at least 150 nm thick can block the SPR effect, mirror references could be fabricated as attachments in other processes at no additional cost. Consequently, a simulation was conducted to determine whether a layer of at least 150 nm thick gold can hinder the SPR effect.

Figure 6.8 presents the simulated SPR curve of a Schott N-SF6 prism coated with 2 nm chromium and 50 nm gold, represented by the blue curve. Assuming the refractive index of the analyte to be

n = 1.47, the orange curve illustrates the prism with an additional layer of 10 nm chromium and 150 nm of gold. On the other hand, the gray curve, which overlaps the orange one, portrays this layer with an analyte that has a refractive index of n = 1.471. No SPR effect is visible here, and there is no discrepancy between the two curves. In the inset, the area surrounding the curve's minimum has been magnified. Displayed is a scale located within the range detectable by a 16-bit camera. There is no significant discrepancy between the two curves.

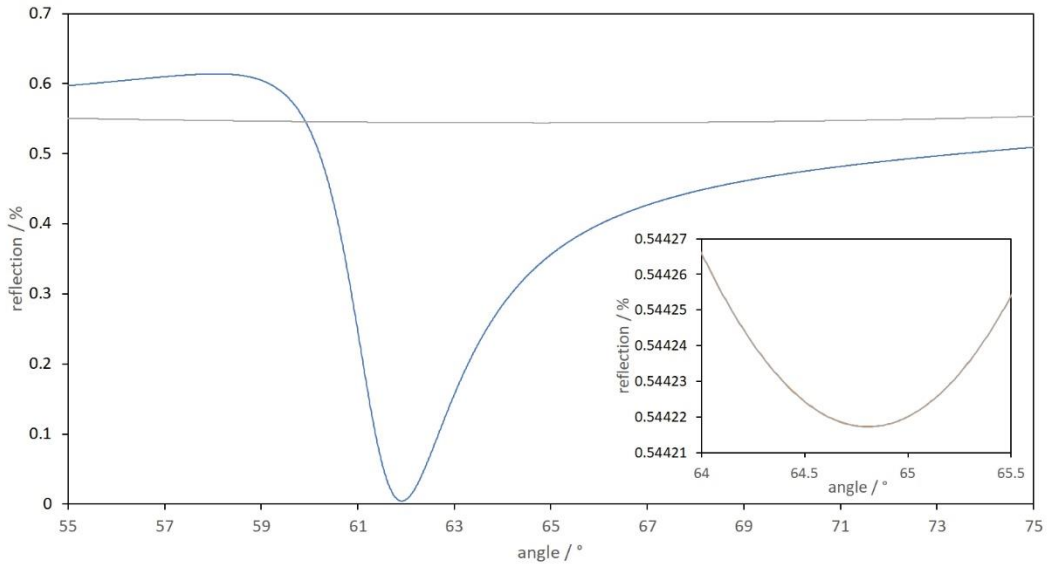

Figure 6.8: Simulated SPR curve of a Schott N-SF6 prism coated with 2 nm chromium and 50 nm gold (blue curve). The refractive index of the analyte is set to n = 1.47. The orange curve shows the same prism, but with an additional Layer of 10 nm chromium and 150 nm of gold. The gray curve (which is covering the orange one) shows this layer stack with an analyte that has a refractive index of n = 1.471. Here no SPR effect is visible and there is no difference between the two curves. In the inset, the area around the minimum of the curve has been enlarged. The simulated curves with 1.47 and 1.471 are still identical to each other.

A mirror array allows for monitoring of the entire sensor surface rather than just one point. Figure 6.9 shows such an array positioned on a SPR-sensitive gold layer.

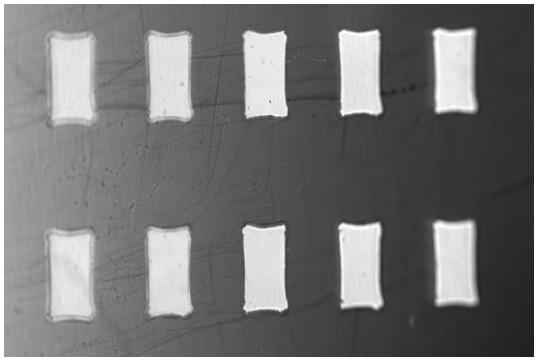

Figure 6.9: Section of an SPR prism equipped with mirror references. The square references are distorted due to the oblique viewing angle. The prism is illuminated slightly divergently. This changes the angle of incidence of the light from left to right. Consequently, a change in reflected intensity can be seen from left to right due to the SPR effect. No intensity gradient can be seen on the completely mirrored areas, since no SPR effect occurs here.

An experiment demonstrated the function of mirror references by depicting how the mirrors react to various events. The first step involved lowering the temperature of the flow cell from 22°C to 21.7°C by 0.3°C. This change affected the SPR signal while leaving the mirrors unaffected. In the following step, the drive current of the light source was reduced by 0.1 mA from 10 mA to 9.9 mA.

This adjustment affected both the SPR sensitive area and the mirrors. The change in refractive index of the analyte is expected to impact the SPR sensitive area, but not the mirrors. Figure 6.10 (brown line) shows that the mirror reflection signal is not affected by changes in the flow cell temperature or the analyte's refractive index.

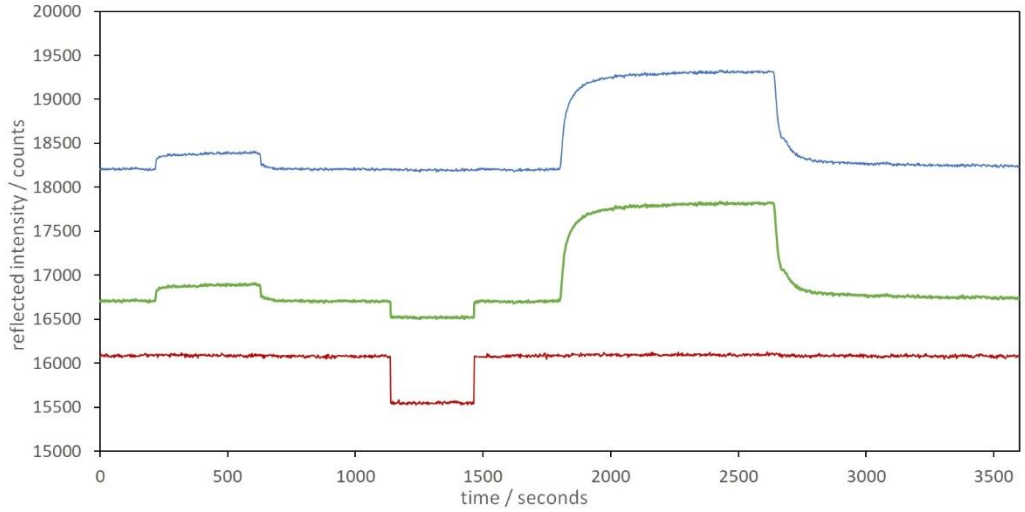

Figure 6.10: An exemplary experiment involves altering the intensity of the light source, adjusting the temperature of the flow cell, and modifying the refractive index. The signal shown in brown originates from a mirror, it is reproducing only changes which are originating from the light source. The signal shown in green originates from the SPR sensitive gold surface, it is reproducing changes which are originating from a temperature change of the flow cell, from a change of the light source and the refractive index of the matrix. The signal shown in blue, is the signal from the gold surface after it is referenced to the signal from the mirror. It does not react to a change of the light source intensity anymore. To be able to display the graphs in one image and so that they do not overlap, the values were normalized to each other and offset against each other.

The green depiction of the SPR signal originates from the prism's SPR-sensitive region. The signal varies with the temperature of the flow chamber, the intensity of the light source, and the refractive index of the analyte. Prior to measurement, calibration is required to account for possible light source fluctuations. Small variations in drive current of the light source are recorded and plotted against changes at the SPR-sensitive surface. The resulting calibration line is utilized for signal calibration. The SPR signal displayed in blue is attained via signal compensation. The SPR signal in blue is still affected by temperature changes in the flow cell and changes in the refractive index of the analyte. But it is now insensitive to variations in the intensity of the light source. Therefore, this demonstrates that drifts originating from the light source can be counteracted by mirror references.

The setup used in the experiment was not optimized for minimizing noise, but rather to demonstrate the feasibility of mirror referencing. The aim of this study was to demonstrate the feasibility of referencing with mirrors. If the signal from SPR is averaged over ten measurements, the standard deviation for a period of 30 seconds is 0.64 digits. Sensitivity was determined to be 188 nA/digit, and by multiplying three times the standard deviation, the resolution was calculated to be 361 nA.

The experiment conclusively demonstrated that it is feasible to stabilize the light source using mirror references. The resolution could be enhanced by minimizing noise and optimizing the illumination of the reference mirrors. The system's resolution of 361 nA is already below the RMS noise of most common current sources.

6.3.3 Refractive Index References

6.3.3.1 Liquid References

A refractive index reference that has a similar refractive index as the analyte could be used for signal stabilization. For stabilization to work, the reference must not be affected by the analyte and must change its refractive index with temperature. If one encloses a small amount of the analyte in a capsule so that it cannot interact with the environment or the analyte being monitored, this volume can be used as a reference.

To prove this assumption, small annular chambers were applied to the flow cell. These capsules were then filled with the reference liquid. The capsules were sealed by installing the flow cell, which is pressed against the prism. Figure 6.11 shows the SPR image of the SPR sensitive area of a prism equipped with encapsulated references.

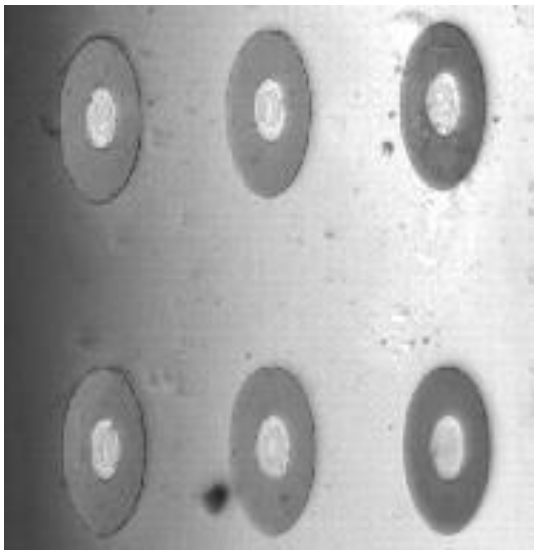

Figure 6.11: Annular chambers filled with liquid refractive index references. The chambers are separating the reference from the analyte and the environment.

An experiment was made in which the intensity of the light source, the temperature of the flow cell, and the refractive index were varied. The signal in brown originates from a liquid refractive index reference and only tracks changes that resulted from alterations made to the light source and temperature. (Figure 6.12). The data shown in green originates from the SPR sensitive gold surface. It is reproducing changes which are originating from a change of the light source, the temperature of the flow cell and the refractive index of the matrix. The data shown in blue originates of the gold surface after it has been temperature compensated with the signal of the refractive index reference. It no longer responds to a change in temperature.

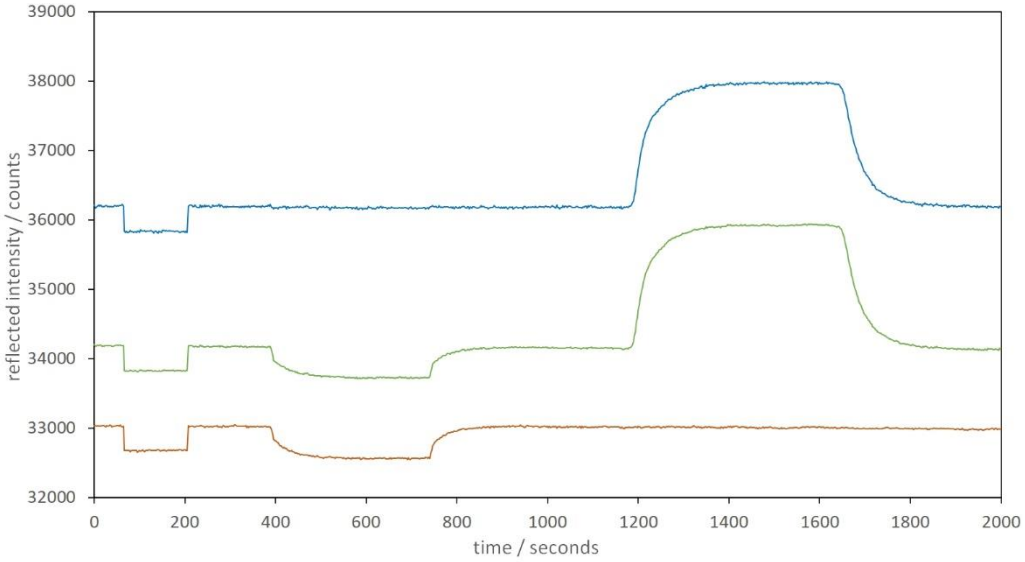

Figure 6.12: An exemplary measurement in which the intensity of the light source, the temperature of the flow cell and the refractive index are changed. The signal shown in brown originates from a refractive index reference. It is reproducing changes which are originating from a temperature change and a light source change. The signal shown in green originates from the SPR sensitive gold surface, it is reproducing changes which are originating from a temperature change of the flow cell, from a change of the light source and the refractive index of the matrix. The signal shown in blue, is the signal from the gold surface after it is referenced to the signal from the reference. It does not react to a change of the temperature anymore. To be able to display the graphs in one image and so that they do not overlap, the values were normalized to each other and offset against each other.

As shown in Figure 6.12, the temperature change introduced by the flow cell was successfully compensated. It was also shown that the encapsulated reference does not respond to a change of the analyte. The experimental setup used here was not optimized with respect to noise. The aim was principally to show whether referencing with liquid refractive index references is possible. If one averages over ten measured values, the standard deviation within 30 seconds is 0.34 digits. A temperature change of 0,3 K leads to a signal change of 429 digits. This results in a sensitivity of 0.7 mK / digit. Multiplying this by three times the standard deviation results in a resolution of 0.72 mK.

The experiment successfully demonstrated that stabilization of the light source via liquid refractive index references is possible. The resolution could be further improved by reducing the noise or optimizing the illumination of the references. However, with a resolution of 0.72 mK, the system is already far below most thermometer which usually have a resolution of 100 mK. Even most precision thermometers do not have a resolution smaller than 1 mK.

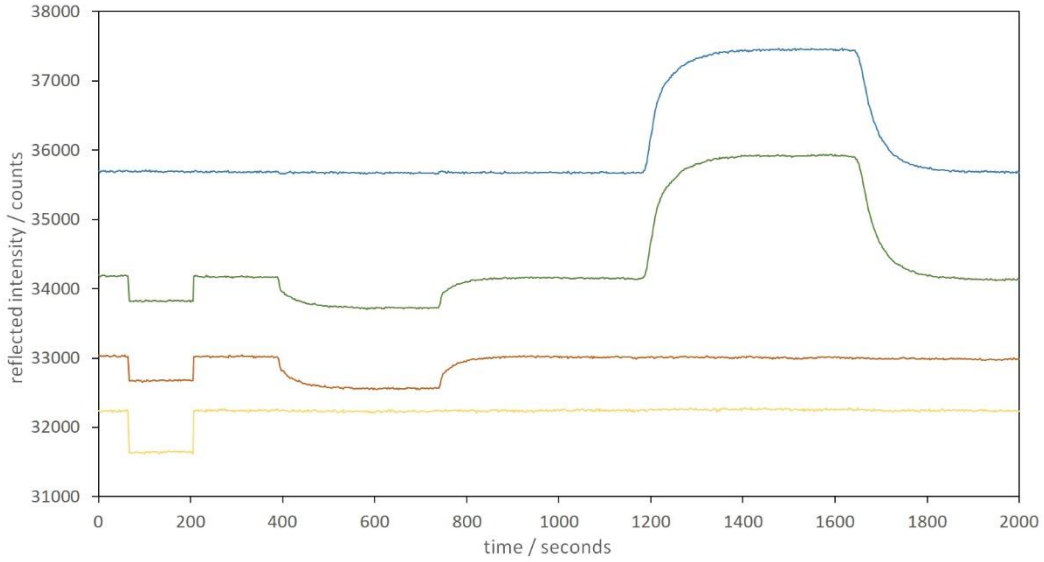

Figure 6.13: Combined referencing with mirror references and refractive index references. Neither a change in temperature nor a change in the light source leads to a change in the measurement signal. The signal drawn in green shows the sensor signal of the SPR-sensitive gold surface. The signal shown in blue was stabilized via the shown referencing methods. The signal shown in brown originates from a refractive index reference, it is reproducing changes which are originating from a temperature change and a light source change. The signal shown in yellow originates from a mirror reference, it is reproducing only changes which are originating from a light source change. To be able to display the graphs in one image and so that they do not overlap, the values were normalized to each other and offset against each other.

To show comprehensive stabilization of an SPR sensor, the measurement from Figure 6.12 was additionally compensated using mirror references. In Figure 6.13 the signal drawn in green shows the sensor signal of the SPR-sensitive gold surface. The signal shown in blue was stabilized via the shown referencing methods. Any fluctuation or drift of the semiconductor devices was compensated via the mirror references. A fluctuation of the analyte temperature was compensated via the refractive index references. The signal shown in blue reacts only to a change of the refractive index of the analyte.

6.3.3.2 Solid References

The use of liquid encapsulated references may not always be possible. The application of the reference is somewhat complicated and may be too time-consuming and prone to faults if prisms are changed frequently or by untrained personal. In addition, the technology is relatively space-intensive compared to the rest of the structures due to the need for the capsule. Furthermore, it could be that the entrapped liquid shows undesirable aging or fouling behavior despite the encapsulation. A refractive index reference made of a solid could overcome these drawbacks and stabilize the SPR sensor similar to a liquid reference.

To show that stabilization of an SPR sensor is also possible with a refractive index reference that consumes less sensor area, an experiment was performed. An adhesive with a refractive index similar to the analyte was determined and applied to the SPR-sensitive area of the prism in a small area.

The brown line of Figure 6. 14 shows the behavior of the refractive index reference. The green line shows the behavior of the SPR sensitive gold surface. The blue line is the temperature compensated measurement signal.

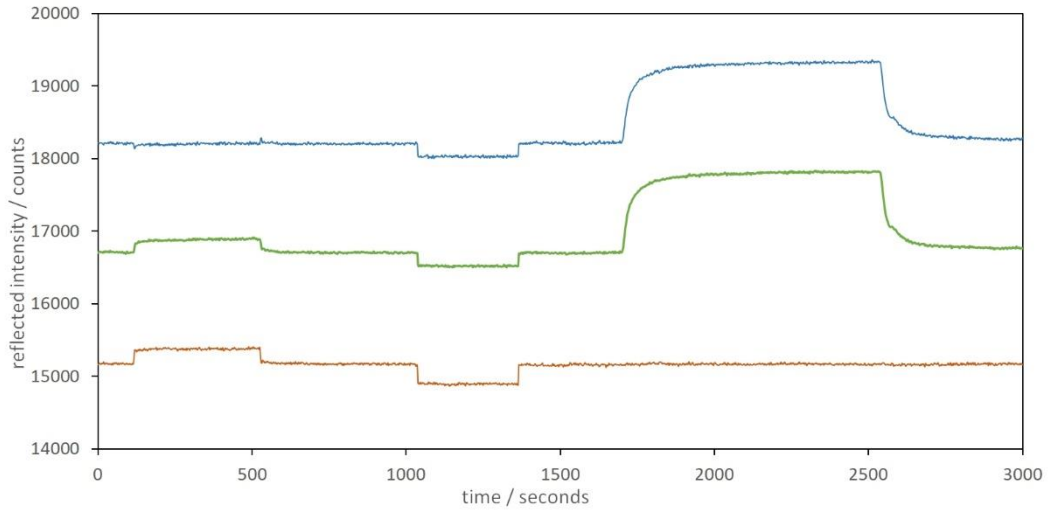

Figure 6. 14: An exemplary measurement in which the temperature of the flow cell, the intensity of the light source and the refractive index are changed. The signal shown in brown originates from a refractive index reference, it is reproducing changes which are originating from a temperature change and a light source change. The signal shown in green originates from the SPR sensitive gold surface, it is reproducing changes which are originating from a temperature change of the flow cell, from a change of the light source and the refractive index of the matrix. The signal shown in blue, is the signal from the gold surface after it is referenced to the signal from the reference. It does not react to a change of the temperature anymore. To be able to display the graphs in one image and so that they do not overlap, the values were normalized to each other and offset against each other.

The first peak shows a change in the temperature of the analyte. The following dip shows a change in light intensity. The following large peak shows a change in the refractive index of the analyte. The experiment shows that the fixed refractive index reference is able to compensate for a temperature variation. Furthermore, it shows that the refractive index reference does not react to changes in the analyte.

Within this experiment, the temperature resolution of the solid refractive index reference is inferior to the liquid reference. The temperature resolution of the reference is only 1.88 mK. The reason for this is an unfavorable placement of the reference. Due to the refractive index difference between analyte and reference, the two substances had to be placed at an angle above and below the SPR minimum. This leads to a deterioration of the sensitivity, for the substance placed on the less steep branch. To overcome this disadvantage, a reference can be developed whose refractive index is closer to the analyte.

The experiment successfully demonstrated that stabilization of the light source via solid refractive index references is possible. Although the resolution was worse than liquid references, it is still in the range of precision thermometers.

6.4 Conclusion

By using the referencing methods shown here, it is possible to construct an SPR sensor system that is insensitive to light source or camera aging phenomena and environmental influences. Conveying the referencing signal within the measuring beam enables a comprehensive monitoring of the optical system. The monitoring of the system and the compensation of temperature variations is realized by applying references to the sensors surface, which is a minimal change on the sensor surface.

Until now, large and energy-intensive temperature stabilizations have blocked miniaturization. This obstacle has been overcome by this work. The resolutions of the stabilization systems shown here are already very good and at the limit of the systems available on the market. The resolution of the light source stabilization in this system is 361 nA. The resolution of the temperature stabilization is 0.72 mK in the system shown. The methods are far from being exhausted and can be further improved.

6.5 References

[1] Schubert, E. 2006. LED basics: Electrical properties. In Light-Emitting Diodes (pp. 59-85). Cambridge: Cambridge University Press. doi:10.1017/CBO9780511790546.005

[2] Naumann, H., Schröder, G., Löffler-Mang, M., 2020. Handbuch Bauelemente der Optik: Grundlagen, Werkstoffe, Geräte, Messtechnik. Carl Hanser Verlag GmbH Co KG. ISBN: 978-3-446-42625-2

[3] Schott AG, 2022, Optisches Glas, Version 0122, Advanced Optics Schott AG, https://www.schott.com/de-de/products/optical-glass-p1000267/downloads

[4] Schott AG, 2016, Technical Information, TIE-19 Temperature Coefficient of the Refractive Index, https://www.schott.com/de-de/products/optical-glass-p1000267/downloads

[5] Yakubovsky, D.I, Stebunov Y.V., Kirtaev, R.V., Ermolaev, G.A., Mironov, M.S., Novikov, S.M., Arsenin, A.V., Volkov, V.S.2019 Ultrathin and Ultrasmooth Gold Films on Monolayer MoS2. Adv. Mater. Interfaces, 6, 1900196

[6] Rosenblatt, G., Simkhovich, B., Bartal, G., Orenstein, M. 2020 Nonmodal Plasmonics: Controlling the Forced Optical Response of Nanostructures. Phys. Rev. X 10, 011071

[7] Yakubovsky, D.I., Arsenin, A.V., Stebunov, Y.V., Fedyanin, D.Y., Volkov, V.S. 2017 Optical constants and structural properties of thin gold films. Opt. Express 25, 25574-25587

7. The Pathway to a Miniaturized SPR Sensor

7.1 Introduction

In today's digital age, inline, online, rapid, and accurate analysis is required. Surface plasmon resonance technology is capable of measuring interactions in real time with high sensitivity and without the need for markers. Thanks to these features, SPR technology has gained great popularity in recent years and is a viable choice for many applications. These range from life sciences, pharmaceuticals, agribusiness, and food industries to environmental monitoring of pollutants [1-3]. Recent advances in the development of SPR technology have been reviewed, an excurse on the different types of instruments available on the market, as well as their advantages and limitations is given at [4]. Laboratory instruments provide the best resolution, however, they are limited in their ability to meet the demands of online and inline sensing. The choice of an appropriate SPR system depends on many factors. For some applications, mostly laboratory-based tasks, the instruments mentioned by Capelli et al. are well suited [4]. However, as the instrument overview in Chapter 1 shows, there is also a great need for miniaturized SPR instruments. Low-cost and miniaturized instruments would open up a universe for SPR technology far beyond its existing applications.

The primary limitation of SPR is its increased susceptibility to fluctuations in instrumental or external factors such as temperature. This sensitivity typically leads to signal drifts that are difficult to compensate for [5,6]. Additionally, the utilization of large optical components continues to impede the development of compact systems necessary for environmental analysis.

In [7] Bolognesi et al. present a miniaturized optical biosensor prototype that combines organic optoelectronic devices with a nanostructured plasmonic grating for sensitive and specific detection of protein and antibiotic analytes in milk. The core part, where the SPR sensing takes place, is already highly integrated and miniaturized. However, the auxiliary components still fill a table and the RIU resolution is poor ($\approx 10^{-4}$ RIU). This system already consists of multiple measurement channels, but it still cannot comprise with the advantages of an SPR imaging system.

SPR-imaging allows a significantly higher number of measurement spots compared to classical SPR. Outliers due to small air bubbles or unwanted binding effects can occur on any SPR sensor surface. With classical single or multi-spot SPR, it is difficult to determine the source of the interference. With SPR imaging, these spots can be identified and then excluded from the analysis. Thanks to the image-based method, the origin of disturbance can be identified more easily in order to avoid it in future measurements. Unlike classical SPR, the regions of interest (ROI) in SPR-Imaging are not segregated by individual channels, resulting in a closer proximity that facilitates more effective temperature compensation. When using inexpensive industrial cameras, regions with only a few thousand or even hundreds of pixels are sufficient to obtain a low-noise signal. Considering that these cameras have millions of pixels, it is obvious how many individual spots can be analyzed in parallel. Ideally the sensor surface will be chemically modified by regions with different binding affinities to different components, allowing to classify certain analytes in a complex matrix [8]. The ability to use many small, but closely located measuring regions allows the use of the references shown in Chapter 5. These references will allow future miniaturized systems to eliminate the need for high-precision temperature control, thus enabling miniaturization.

7.2 Feasibility in Principle of a Miniaturized SPR System

For the development of a cost-effective, durable, and compact SPR system, it is preferable for the system to be free of moving parts. In order to initiate the miniaturization of the system, it is necessary to verify the feasibility of SPR imaging without the use of moving components by ensuring a high RIU resolution. A reference measuring device that allows for individual system components to be evaluated is essential to demonstrate this capability.

Laboratory SPR imaging systems such as the Bruker Sierra don't use cameras with a lens to image the entire SPR sensor surface at once. Instead, they scan the surface point by point and generate an image later. This technology requires a scanning mirror, which is a moving component. Therefore, this technology is less suitable for miniaturization. To find the ideal technology for miniaturization, a platform that can test different technologies is inevitable. For this purpose, a highly flexible reference measurement system has been developed. The reflectivity based SPR technology has turned out as most powerful for miniaturization. Therefore, the reference system has been developed to work best with this technology. While the reference system naturally boasts higher resolution than the eventual miniaturized sensor, it was crucial to implement that highest resolution to thoroughly examine all potential influences during development and the limitations of each individual component. Figure 7.1 shows the SPR reference system built on a passive stabilized optical bench and operated in a windowless optical laboratory equipped with air condition to avoid as much external stress on the system as possible but to be able to handle an open configuration.

The reference system has a resolution in measuring changes in the refractive index in the 10^{-7} range and can be operated without moving components when the measurement is performed with intensity-based read-out at a fixed angle of incidence. Thanks to its highly flexible design, it can also record SPR curves or perform a wavelength scan.

The Peltier elements in the light source and flow cell are regulated with an accuracy of 0.1K. To achieve a lower temperature ripple, a metal block is placed between the temperature-sensitive area and the Peltier element. This mitigates the temperature variations resulting from the regulation. The 730 nm LED in the light source emits a maximum radiation flux of 270 mW. Typically, however, it is operated at much lower power to prevent overexposure of the detector. In the commonly utilized range of up to 10 mA, the Keithley source meter exhibits a peak-to-peak noise of 200 nA. The sCMOS camera has an active area of 2048 x 2048 pixels, with a pixel size of 6.5 µm. The lateral resolution on the SPR chip depends on the lens and other accessories used. The camera typically produces a dark noise of 0.8 electrons per second and pixel. The quantum efficiency at 730 nm is approximately 60%. If the reference measuring station is to be operated using angle scanning instead of intensity-based measuring mode, the repeatability of the linear stage, which is 15 µm, becomes a crucial factor that determines the resolution. To perform a wavelength scan, the filter head of the Kurios wavelength filter shown in Figure 6.1 must be installed. The filter has a range from 420 nm to 730 nm and a full width at half maximum of 10 nm. Instead of a manually rotatable polarization filter, one may install a Thorlabs K10CR1 Rotation Mount, which enables automatic polarization variation during measurement. This feature can be employed for referencing strategies.

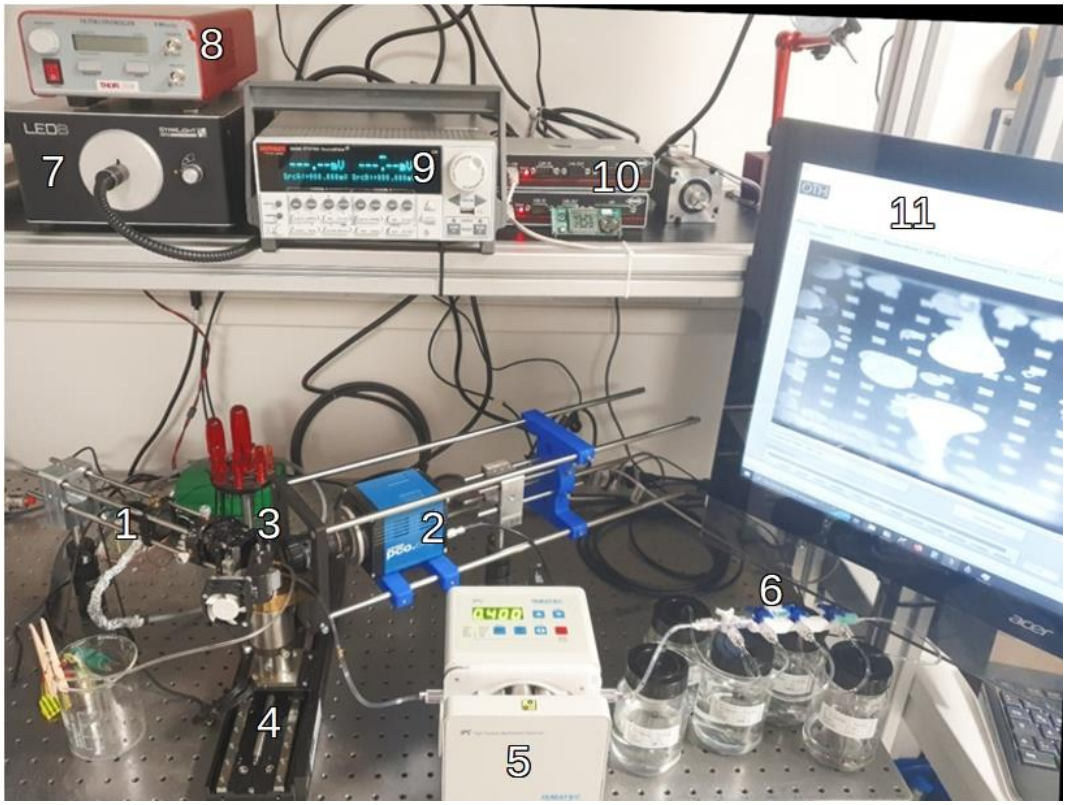

Figure 7.1: SPR-reference system, is the v-shaped basic module of the SPR-system, at the left side of the V is the LED-light source (1), at the right side is a sCMOS camera (2), at the center of the V is the SPR-prism (3). To alter the SPR angle, the center of the V can be moved forward and backward by a motorized translational stage (4). All the components of the system can be exchanged. (5) is a peristaltic pump which is supplied from 5-way valve bank (6). It enables to switch between different analytes by minimizing the introduction of air bubbles into the system. (7) is a white light source, (8) is a tunable filter, which can be used to perform wavelength scanning SPR. (9) is a source-meter which is used as a low noise current driver for the LED-light source. (10) is the linear table controller. (11) shows the SPR-image of the prism surface acquired by a homemade software to control the measurement and to record the data.

7.3 Feasibility of Cost Reduction

Miniaturized and widely used sensor systems should be affordable. Therefore, it must be demonstrated that the cost can be reduced while maintaining essential functions. To achieve cost savings, any non-essential features should be eliminated. For this reason, research must be conducted to determine how much functionality can be sacrificed.

The SPR reference system is a costly option as the components in Figure 7.1 alone amount to around €50,000. Therefore, this system is impractical for sensing applications due to its high cost. It is necessary to determine if adequate resolution can be achieved with less expensive and compact system components. To investigate whether the required RIU resolution can be achieved with less expensive components, and to perform long-term experiments in parallel with shorter-term measurements, an intermediate step towards a miniaturized system was developed. Figure 7.2 shows the laboratory prototype of a potentially miniaturized SPR Sensor-System.

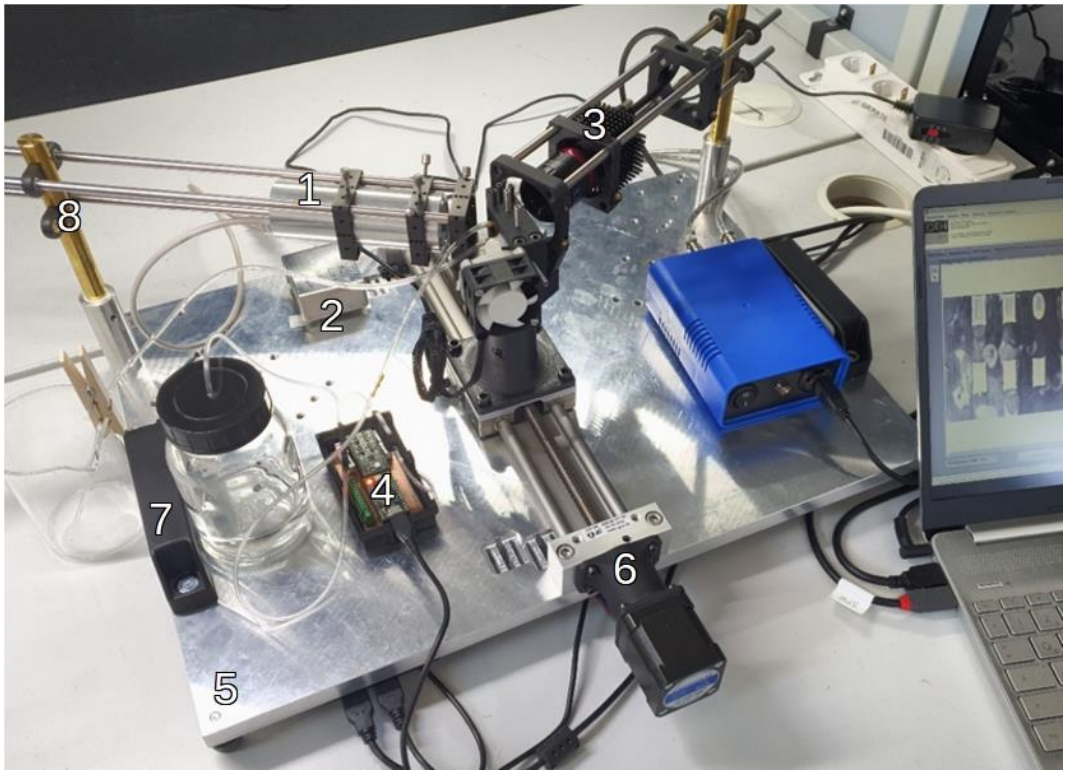

Figure 7.2: SPR-laboratory prototype. The device is designed as a flexible v-shaped instrument like the reference system. The light source (1) is now within a tube, this enables a faster exchange of light sources, and it protects the light source parts from dust. The source is driven by a small low noise current driver (2). The 16-bit sCMOS camera is exchanged against a much smaller 14-bit industrial camera (3). The large peristaltic pump is replaced against a micro valve pump (4). The USB controlled pump driver can handle up to four pumps. The components of the SPR-system are mounted on an aluminum plate. The plate has circular arranged M6 threads on each of the two arms connected to the prism holder (5). Compared to an optical table, the prefabricated plate offers an advantage in terms of reducing the likelihood of component misalignment due to the presence of arranged holes. It also enables a fast and secure-symmetric change of the position of the edge posts. The high-precision linear table has been replaced by a simpler industrial linear table (6). To ensure portability, handles (7) were affixed to each side of the device, and the individual components were connected through a USB hub located on the underside of the panel. When inexperienced users had to readjust the device after replacing its components, they often failed to remember the adjustment. To mitigate the detrimental impacts of misalignment, a bearing with increased degrees of freedom (8) was installed at the corners of the V-arrangement.

The costs for assembling the laboratory prototype are only about 10% of the costs of the reference measuring system. The space requirement and the size of the individual components are also reduced. Due to the lower camera resolution (16-bit vs. 14-bit) and the lack of cooling of the camera, the RIU resolution of the system is slightly lower. By using the reference system, all other components have been optimized and reduced in their range of functions so that the performance of the system is not impaired.

The camera utilized in this study provides a resolution of 3072 x 2048 pixels with a pixel size of 2.4 micrometers. The pixels are read out with a 14-bit resolution and have a dark noise of 2.42 electrons per second and pixel. The LED utilized is of the same type as the reference device. The costly source measurement unit (SMU) was substituted with a small, low-noise diode driver. The new driver delivers up to 40 mA and has a maximum RMS noise of 60 nA.

7.4 Miniaturization Through the Development of New System Concepts

The costs of the laboratory prototype are still too high to use such a system in sensor applications. Additionally, the components are still oversized for a miniaturized system and cannot be scaled down accordingly. Therefore, new concepts must be developed for the individual functional units.

The lab prototype is a significant improvement over the reference system. However, it remains much larger than a handheld device. The use of new technologies is necessary to reduce the system to a handheld size. These technologies were developed using both the reference system and lab prototypes and were elaborated in the previous chapters (Chapter 3 light source and lensless imaging, Chapter 5 reference technologies). As a result of this research, an SPR sensor of handheld size was achieved (Figure 7.3).

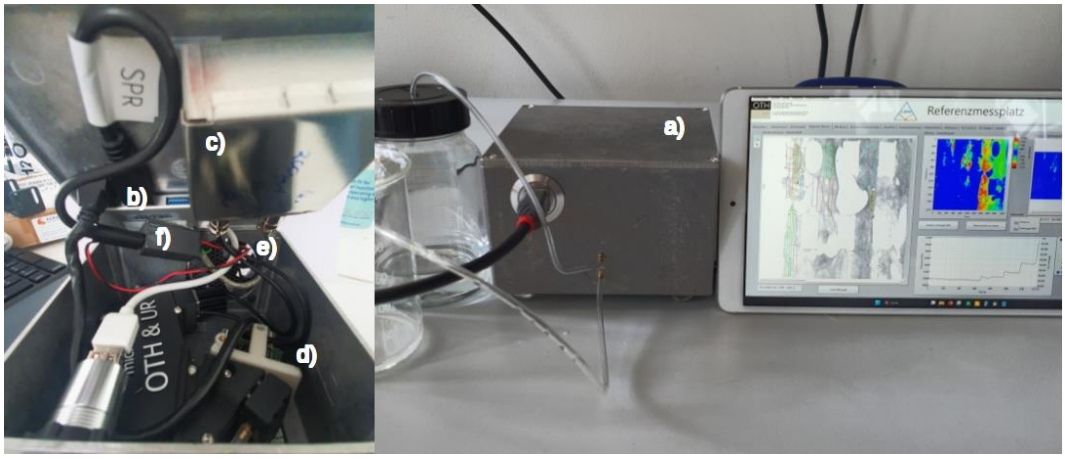

Figure 7.3: SPR-Sensor Prototype. The SPR Sensor Prototype is housed in a 125 x 125 x 80 mm box (a). The box contains a USB hub (b), which supports a USB-powered micro pump, a LED driver for the light source (c), a camera (d) and a system cooling fan (e). The power supply is done by a USB3 Power delivery module (f). Infront of the box is a USB-3 Port, which delivers the power supply and transfers the cameras data to a Tablet-PC where the sensor software is running.

In contrast to the previous technology levels, the angle of incidence can no longer be adjusted here. All lenses and objectives have been removed. The system is optimized for one particular application and, unlike the previous systems, can therefore only be used in a narrower, predefined refractive index range. The system is extremely compact and contains all the components necessary for operation. Only a computer must be connected via USB. This connection is used for both power supply and data transfer.

By developing new concepts for the individual functional units, the size of the system was once again significantly reduced. In addition, costs were again significantly reduced. The result is a cost-effective, miniaturized SPR system. The Hardware Components, excluding the Tablet-Computer are less than 1400 €. This system can also be used outside laboratories for SPR imaging.

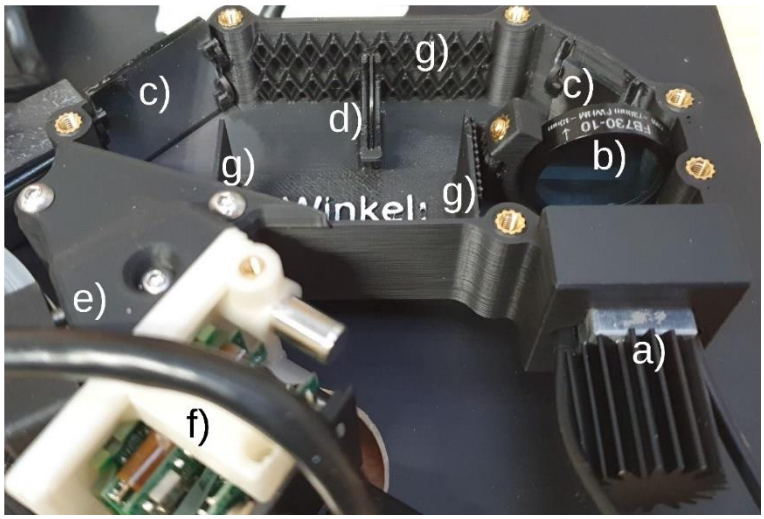

Figure 7.4: Inside view of sensor core. a) 730 nm LED, b) mounted standard filter for 730 nm, c) mirrors, d) polarization filter, e) SPR prism, f) camera, g) beam traps.

The miniaturized sensor (Figure 7.4) employs the same LED and current driver as the laboratory device. Its new, more integrated design works without lenses, so the distance between the LED and the prism determines the divergence of the light. The beam path is folded and redirected by two mirrors so as not to increase the space requirement too much. Additionally, the distance between the LED and the prism guarantees that only the inner, more uniform portion of the beam is utilized. The outer and inner walls, designed specifically for this purpose, serve as apertures. To reduce reflections, the walls are equipped with beam traps. The camera utilized is identical to the model used for laboratory measurements. To be able to position the CMOS chip directly at the prism, the housing was removed. Due to the absence of housing, the camera requires additional cooling. This is achieved by directing the flow of air, which cools the sensor, through the camera electronics.

7.5 System Performance

After establishing a state-of-the-art laboratory reference setup for SPR imaging and implementing multiple steps of miniaturization and system integration, it is of great interest to compare the performance of the created systems with a commercially available SPR device. However, it is important to note that obtaining absolute performance comparisons is difficult due to various factors, including the SPR-sensitive layer. The precise layer structure of commercial SPR chips is typically undisclosed and rarely reported in publications. It is typically only mentioned in publications that explicitly address the composition and/or structure of the SPR-sensitive layer. Several factors hugely impact the performance of an SPR system:

a) Gold-glass interface (substrate roughness, layer structure, deposition method, layer materials, material purity and pre-aging)
b) Quality of functionalization (receptor layer stability, receptor density, receptor orientation)
c) Stability of the functionalization (pH changes, temperature, regeneration, unspecific binding)

It would therefore be disproportionate to make a precise comparison of system performance. In order to be able to classify the system performance, the systems developed are compared with the

SPR devices of the leading manufacturers. The data of the commercially available devices have been obtained from the literature [4].

The data of the homebuilt instruments were all determined with the same prism (Schott F2 glass), the same custom-made flow cell (brass block with silicon seal) and the same liquids (water, the refractive index of which was adjusted with glucose content). Measurements were made first in the reference set-up, then in the laboratory prototype, and finally in the miniaturized sensor. The parts were removed from the first instrument and installed in the next. The prism was used before the measurement. Prior to conducting a comparative analysis, the three systems were initially evaluated using a solution with the minimum refractive index, followed by a solution with the maximum refractive index. A false-color image generated by the SPR software reveals the areas with the greatest change in reflectivity, indicating the highest sensitivity. Based on this, the ROIs for the subsequent measurements were situated accordingly. This procedure can be performed easily and quickly even by untrained users. The resolution could be further increased by further subclassifying the regions with the highest resolution and adapting the size and shape of the ROI to the respective conditions. This method was used to provide a procedure that can be easily and quickly reproduced by any user. The results are shown in Table 7.1.

Table 7.1 The RMS baseline noise and baseline drift is given in RU, according to communication with Bruker, 1 RU equals approximately 10-6 RIU. The baseline RMS noise of the developed set-ups was derived with the following method: The baseline drift was removed, following the noise was reduced by generating the sliding average over 10 values. A timespan of 30 seconds was chosen, and the drift was removed. Finally, the standard deviation within these 30 seconds was calculated and compared to the commercial instruments.

Manufacturer	**Device**	**Baseline Noise RMS, RIU**	**Baseline drift, RIU/min**
Biacore	Biacore S200	$1.5 \cdot 10^{-8}$	$3 \cdot 10^{-7}$
Bruker	SPR-24/32 Pro	$2 \cdot 10^{-8}$	$1.5 \cdot 10^{-7}$
Sartorius	Octet SF3	$3 \cdot 10^{-7}$	$3 \cdot 10^{-7}$
Home made	Reference system	$6.5 \cdot 10^{-8}$	$1.9 \cdot 10^{-7}$
Home made	Laboratory prototype	$1.4 \cdot 10^{-7}$	$1.7 \cdot 10^{-6}$
Home made	Miniaturized sensor	$7.4 \cdot 10^{-7}$	$8.3 \cdot 10^{-6}$

As anticipated, the RMS noise and drift of the miniaturized SPR sensor are greater than those of the reference system. Nonetheless, the RMS noise level is sufficiently low to enable application of this technique in a real sensor. If compensated by the method discussed in the preceding Chapter 5, sensor drift should not pose an issue.

Unfortunately, it was not possible to find out the exact RIU resolution of the commercial devices, as both Bruker and Biacore claim not to know the RIU resolution of their devices. According to Bruker, RU resolution can be converted to RIU with approximately 1 RU being 10^{-6} RIU.

The Limit of Detection (LOD) was determined to better characterize the performance of the homebuilt systems. Figure 7.5 shows the refractive index change of a solution that can be resolved by each instrument. To obtain this graph, the baseline of the signal was normalized. The refractive index of the analyte solutions was determined using a Krüss DR6300T. The accuracy of the instrument is ± 0.02 mRIU. The values used are the average of ten measurements. Due to the large measuring range of the SPR instruments and the small standard deviation, the error bars cannot be identified on this graph.

The highest resolution of $1.0 \cdot 10^{-7}$ RIU/digit was obtained for the reference system, which is due to the temperature stabilized 16bit camera and the homogeneous, low noise light source. The light source and the flow cell are also temperature stabilized. The temperature stabilization of the components contributes significantly to the low drift. The measurement range is just under $1 \cdot 10^{-2}$ RIU. The LOD is $2 \cdot 10^{-7}$ RIU, which is five orders of magnitude lower than the measurement range.

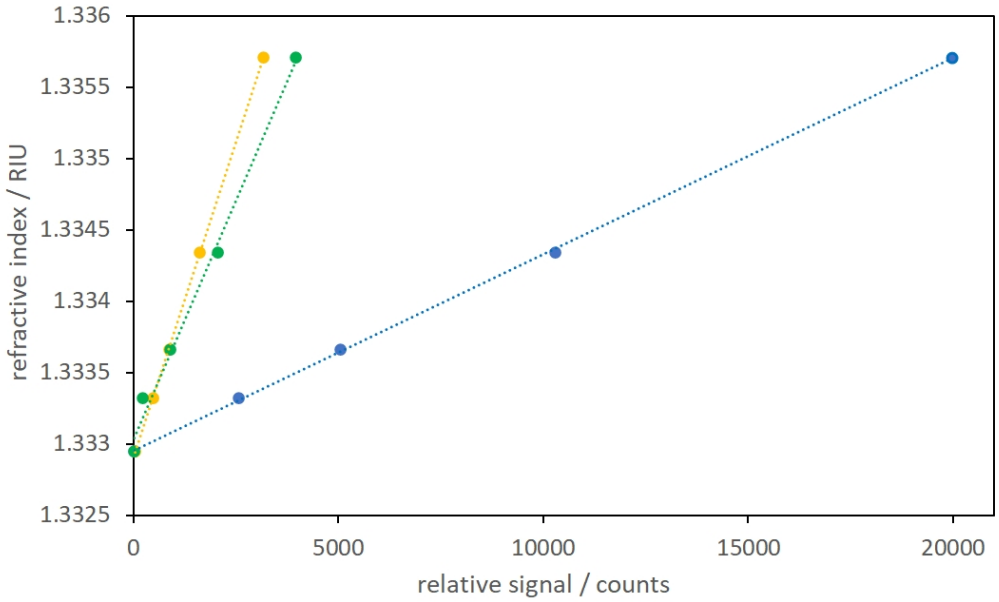

Figure 7.5: The systems developed in this work were compared with respect to their refractive index resolution. The diagram displays the resolution of each device. The measured values of the reference system appear in blue, those of the laboratory prototype in orange, and those of the miniaturized sensor in green.

For the laboratory prototype, the light source and flow cell are also temperature stabilized. The 14-bit camera is not temperature stabilized. It is also difficult to bring the camera into absolute thermal equilibrium with the environment because it varies its heat dissipation depending on its operating state. In addition, the camera temperature follows the ambient temperature. The LOD is $4.2 \cdot 10^{-7}$ RIU. The light source and the possibility to change the SPR angle are similar to the reference set-up.

In the miniaturized sensor system, none of the components is temperature stabilized. The LOD is $2.2 \cdot 10^{-6}$ RIU. As expected, the drift of the not stabilized system is significantly higher than that of the reference system.

The miniaturized SPR sensor and laboratory prototype exhibit a comparable resolution of RIU per digit, indicating miniaturization doesn't impede high RIU resolution. The 16-bit reference system has significantly higher RIU resolution, emphasizing that bit resolution plays the main role in achieving such high RIU resolution. Currently, only 14-bit cameras are cost-effective and accessible in a compact form factor. Nonetheless, it is likely that 16-bit cameras will become more affordable and compact in the near future.

7.6 Utilization of the SPR Instruments as a Biosensor

The practical applicability of the laboratory prototype and miniaturized sensor system was investigated by examining the binding of bovine serum albumin (BSA) protein to a modified sensor surface and the binding of immunoglobulin G (IgG) antigen to the BSA-modified surface. Additionally, the same experiments were performed identically utilizing a commercially available SPR instrument (Biosuplar 521) from Mivitec.

For each system, the gold surface was cleaned by rinsing with water and ethanol. The gold surface was covered with a monolayer of 16-mercaptohexadecanoic acid (C16-SH, Sigma-Aldrich) by a self-assembly process. The gold surface was immersed in a solution of 200 $\mu mol \cdot L^{-1}$ C16-SH in ethanol. After 48 h at room temperature, the gold surface was again carefully rinsed with ethanol and dried in a nitrogen stream. This self-assembled monolayer serves two functions. First, it provides carboxyl groups at the top of the surface to which a protein can be chemically attached, and second, it protects the gold surface from non-specific binding of biomolecules [9]. Since proteins are composed of the amino acid cysteine, they also have thiol groups, which are known to bind strongly to gold. It would be better to use thiols with polyethylene glycol groups for blocking, but then one needs a mixed monolayer of at least two thiols, one for blocking, one for binding. Since this is difficult to achieve in a reproducible, homogeneous quality, only one thiol was used in this comparative study. BSA binding was monitored online with all three SPR systems and the time course of the refractive index change is shown in Figure 7.9 (a-c). The three systems' signals were calibrated using two refractive index known solutions, indicating a linear response to refractive index change. However, this linearity is only valid within a limited range, as the SPR curve's shape is not linear. Furthermore, it should be emphasized that large refractive index changes can also change the SPR reflectivity curve's shape when plotted across different angles. This did not occur here, as verified by an angular scan taken with the Biosuplar device. Additionally, minor changes in refractive index, which are applicable in sensing applications, do not significantly alter the shape of the SPR curve. This technique is widely recognized in academic literature [10]. In experiments where the refractive index is shifted to higher values, it is recommended to choose a measurement angle slightly lower than the SPR angle (angle at which the reflected intensity is minimal [11]). This was not done here. The angle was selected on the flatter side of the curve instead of the steeper and more advantageous flank. This choice was made due to the use of a refractive index reference with a slightly different refractive index than the matrix. To avoid the need to constantly adjust the angle, the measurement angle was set to 62,5° so that both ROIs show an SPR effect. It should be noted that the structural components of the miniaturized sensor are mainly 3D printed components. The optical components are only inserted into the housing and are not adjusted. This results in a lower precision than in the laboratory setup. The laboratory prototype was operated with the slightly divergent light source described in the previous chapters. The miniaturized sensor was illuminated only by a LED with filters. This causes the angle to spread over the sensor area. Thanks to this method, the angle can be slightly varied both before and after the measurement.

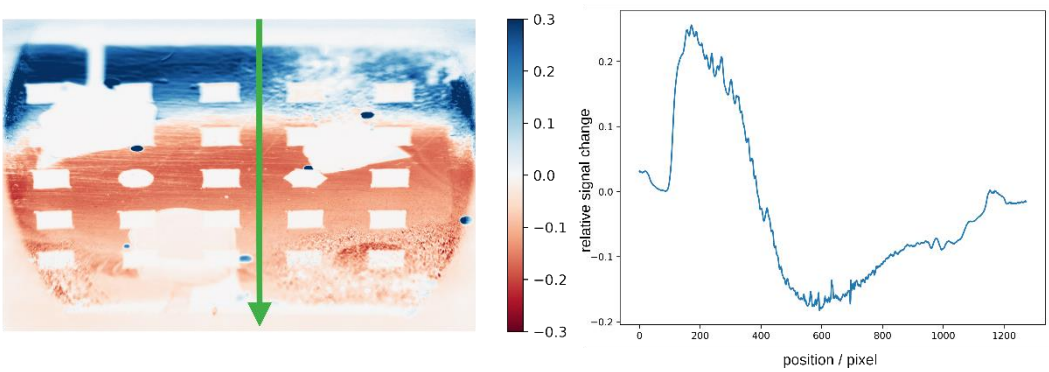

Figure 7.6: The image is a false color depiction of the SPR sensor chip employed in the experiments. The mirror references, represented by squares, a hexagon, and a circle are utilized to compensate for changes that arise from alterations in the light source or the camera. The three large, bright, round areas serve as refractive index references, which are used to compensate the effect of temperature variation. The white line, running from right to left, represents the SPR minimum.

Figure 7.6 shows a picture of the SPR-prism used within these experiments. The red region indicates the area in which the SPR curve's flatter branch lies. The blue area shows the other side of the SPR-minimum, where the SPR curve has a steeper inclination. Normally, this area is preferred for placing the ROI. However, here refractive index references were placed at the prism and these references had a refractive index, which is slightly different to the refractive index of the matrix. Therefore, the angle had to be adjusted to ensure that both areas exhibit a SPR effect. In the experiment, both the SPR laboratory instrument and the miniaturized sensor exhibited remarkable sensitivity despite of this disadvantageous setup. The red area shows the area in which a negative change occurs due to the addition of the antibody. The blue area shows the area where a positive change occurs due to the addition of the antibody. The white areas show a very low change in intensity.

At the beginning there was a flow of NaCl (100 µmol·L$^{-1)}$, then the solution was changed to phosphate buffer (10 mmol·L^{-1}, pH 7.4) with physiological NaCl content (140 mmol·L^{-1}). The buffer composition was chosen to maintain the structure of the protein in solution. A strong increase in the refractive index can be observed. This can be attributed to changes in the bulk refractive index (Figure 7.7). When the change of fluids was performed on the miniaturize sensor (Figure 7.7 green graph), a larger air bubble was released within the system. This led to the extremely high signal change. Since this is a common and frequently occurring problem, the measurement was not restarted. With a single-channel device, the measurement would have had to be repeated, since it is not possible to ensure whether there is still air in the measurement region. With the imaging device, the camera image can be analyzed to determine the regions where air is entrapped on the surface. Those pixels can be excluded in data analysis afterwards if necessary.

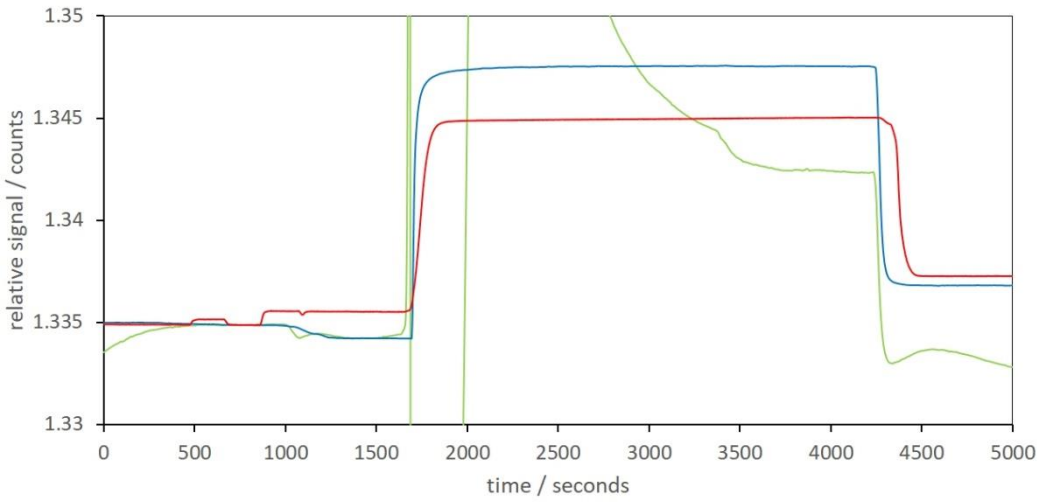

Figure 7.7: The graph shows the change from buffer solution to the protein solution containing the carbodiimide coupling reagent. In the process, the gold surface of the SPR sensor was functionalized with BSA. The signal for Biosuplar is drawn in red, for the laboratory set-up in blue and for the miniaturized sensor in green.

At 4250 s the immobilization was stopped and the solution in the measurement cells was changed again to the same buffer solution which was applied from the beginning. The difference in signals at the end can now compared to the ones in the beginning. The increase for the Biosuplar and the laboratory prototype indicate a binding of BSA. The same is expected for the miniaturized sensor, but here a large air bubble got entrapped upon the change to the BSA containing solution. Since air bubbles always leave smaller deposits and this air bubble filled the entire measurement area, no definitive statement about the success of BSA immobilization is possible here.

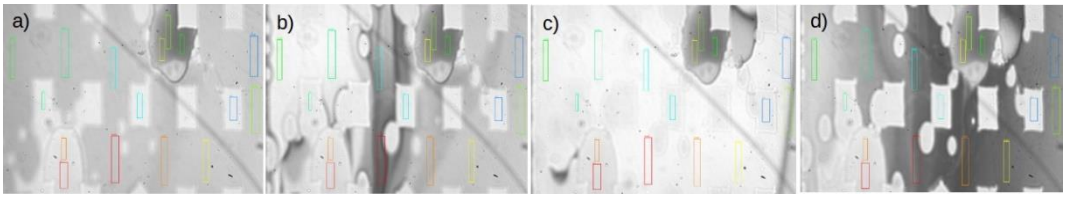

Figure 7.8: The images show the sensor area of the miniaturized sensor during the change of the solution from buffer to the protein-containing solution. The prism used is 18x18 mm. However, since direct imaging without lenses is used here, the sensor area recorded by the system corresponds to the area of the camera sensor. Figure a) shows the sensor after it has been filled with buffer. During the filling process, some smaller air bubbles have settled in the sensor. b) A larger volume of air was drawn into the system when changing from the buffer solution to the functionalizing solution. The provided graphic illustrates the process of the air bubble gradually filling the measurement region. c) The air bubble fills the entire measuring range. d) The air bubble has been flushed out of the measuring area again.

The small bubbles shown in Figure 7.8 a) can be identified as small, round, and bright spots. These, if they remain stable, do not contribute to a signal change during the measurement. However, if they begin to migrate, they will interfere with the signal. Classic SPR sensors, which only generate their signal from a range of several millimeters in size, are severely affected by such air bubbles. If no image is available to the scientist or Software, it is often hard to unambiguously recognize the influence of an air bubble. In Figure 7.8 b) a very large bubble is entering the flow cell. The appearance of the bubble is due to the need to stir the protein solution with the coupling reagent (1-ethyl-3-(3-dimethylaminopropyl)carbodiimide, EDC), which generally generates foam. Swift immobilization is crucial as the EDC can react rapidly. Consequently, degassing is impossible before implementing the functionalizing solution onto the SPR sensor. In Figure 7.8 c), the air bubble has filled the entire measuring range. Compared to Figure 7.8 a), it can be seen that the number, position and size of the original air bubbles have changed in Figure 7.8 d). In classical SPR, the presence of air in the measurement area could greatly impact the measurement or even render it invalid. However, with the

utilization of imaging techniques, the sensor surface can be observed in real time and with precision. As the entire image data was recorded along with the measured values of the selected ROI, it is feasible to relocate the ROI to a location not influenced by the migration of air bubbles.

Discussion of the Binding and the Sensitivity

The signal to noise ratio (S/N) (estimated over 100 s between 4700 s and 4800 s) of the Biosuplar is 79,333 relative counts and that of the lab setup is 146,823 relative counts. Therefore, the S/N of the laboratory setup is about 1.9 times better than that of the commercial system. The S/N of the sensor, estimated between 1400 s and 1500 s, is 59,692, which is 0.8 times that of the commercial device. The commercial device has an average sensor area of about 0.5 mm^2. The laboratory system's virtual region of interest (ROI) measures 100 by 1000 pixel. It consists of pieces with a size of 10 x 20 pixel. The whole area of the virtual ROI would correspond to an area of 0.24 by 2.,4 mm on the camera. This area is 1.6% of the CMOS sensor area. By using a VIS-NIR lens (Edmund Optics #67715) and an additional C-Mount spacer, the corresponding area on the SPR chip is 0.72 x 7.2 mm and occupies about 2% of the active SPR-sensor area. The virtual region of interest (ROI) in the miniaturized sensor system has a size of 200 by 500 pixels and consists of areas with a size of 80 x 40 pixel. This equals an area of 0.48 x1.2 mm on the camera. This area is 1.6% of the area of the CMOS sensor. Since the miniaturized system does not use a lens to image the SPR sensor, the area on the CMOS sensor is equivalent to the area on the SPR sensor. However, due to the significantly smaller size of the CMOS sensor, only a fraction of the SPR sensor can be used for measurements. The CMOS sensor has a size of 7.37 x 4.92 mm, the SPR prism has a size of 18 x 18 mm, where 16 x 16 mm are useable. It should be noted that the sizes of the areas are given without considering the angular distortion, since it varies with the angle.

The binding of IgG to BSA is of great interest in immunology and diagnostics. IgG is an important antibody type with widespread roles in the immune response. BSA is often used in assays where IgG molecules are either captured or detected. SPR is one of the best techniques to study this affinity, mainly because it allows real-time monitoring. This is critical for understanding the kinetics of the BSA-IgG interaction, providing not only the equilibrium constants, but also the rates of association and dissociation. Many other techniques for studying protein interactions require the use of fluorescent or radioactive labels, which can alter the properties of the proteins and potentially affect the interaction. Sensitivity is critical when studying interactions in biological fluids, where the concentrations of interacting partners can vary. Determining very low levels of immunoglobulin G (IgG) in biological fluids is important for several reasons, ranging from clinical diagnosis to understanding disease mechanisms and monitoring treatment. Low levels of specific IgG antibodies can serve as early markers for several diseases, including infections and autoimmune disorders. Early detection can significantly improve patient outcomes. Levels of specific IgG could be used to monitor the efficacy of treatments such as vaccines, immunotherapies, or antimicrobial treatments. Low levels of IgG can provide insight into the state of the immune system, which could be particularly important in immunocompromised patients or those undergoing immunosuppressive treatment. Understanding the longevity of low-level IgG responses can provide insight into the duration of immunity following infection or vaccination. For this reason, all three sensor systems with BSA as the capture protein were used to study the binding of IgG. The antigen was dissolved in buffer (phosphate, 10 mM, pH 7.4, 140 mM NaCl) and applied to the sensor surface at increasing concentrations (0.25, 0.5, 1, 2.5, 5 µg mL^{-1}). The sensorgram is shown in Figure 7.9.

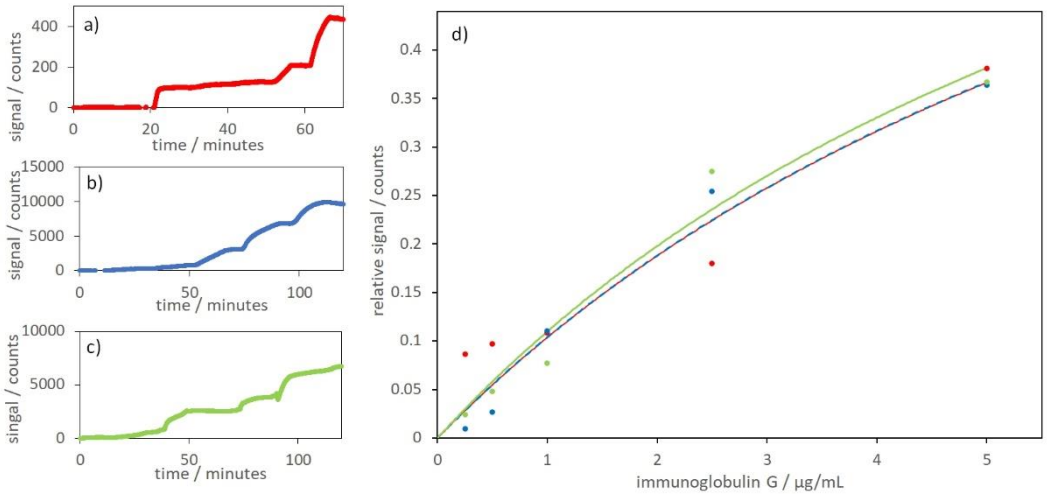

Figure 7.9: Time course of the sensor signal when increasing the concentration of antigen in the solution for Biosuplar (a, red), laboratory set-up (b, blue) and miniaturized sensor (c, green). At 6340 seconds, a change from buffer to a solution containing 0.25 µg/mL IgG was made. Subsequently, the concentration was increased in the following steps. At 7640 seconds to 0.5 µg/mL IgG, at 8940 seconds to 1 µg/mL IgG, at 1240 seconds to 2.5 µg/mL IgG, at 11540 seconds to 5 µg/mL IgG.

The results demonstrate that all three set-ups show similar behavior in the detection of the binding of IgG to BSA. Table 7. 2 lists the binding constant when analyzing the data by a Langmuir isotherm. The differences are due to experimental conditions, even when it was tried to perform all experiments with the same solutions and the same protocol, every device was equipped with an individual prism and the ambient temperature and therefore the temperature of the solutions was not controlled. This is in accordance to the practical situation when SPR should be used for a sensor application.

Table 7. 2: comparison of the binding constants of the three devices, that were used for the experiments.

device	binding constant in µg/mL
Biosuplar	8,64
Laboratory prototype	8.10
miniaturized sensor	8.62

7.7 Conclusion

The research process outlined in this chapter has yielded three categories of devices. In some aspects the devices display stark differences. In part, nonetheless, the devices share many similarities. Consequently, their fields of application differ or overlap.

The reference setup is a research instrument that provides the highest resolution for a reflectivity based SPR imaging instrument with a camera detector. This is made possible by its low-noise, homogeneous, monochromatic light source and cooled 16-bit SCMOS camera. The bidirectional repeatability error of the angle-adjusting linear stage is less than 15 microns, allowing SPR curves to be generated with high precision. The temperature stabilization of the light source, camera and flow cell also ensures excellent measurement stability over long periods of time. The homogeneous illumination of the sensor area with a monochromatic, coherence-free light source ensures high lateral resolution as well as low signal noise and disturbance-free operation. The measurement setup is designed to give researchers maximum flexibility in their work. This applies to SPR instrumentation research as well as receptor and application technology research. The angle-adjustable arms of the SPR reference instrument are based on commercially available optical cage systems as offered by all major vendors. The commercially available sizes of 30 mm, 40 mm and 60 mm as well as the in-house developed systems of 80 mm and 100 mm can be mounted. Within these cage systems, all components desired by the researcher can be freely mounted. The USB3 Vision standard, which includes the GenICam interface, has been implemented in the software to make camera replacement as easy as possible. Since all the components used have software interfaces provided by their respective manufacturers, researchers can also operate the measurement setup with their own software. The SPR prism is mounted in a holder in the central joint of the setup. Depending on the application, different prism or fluidics can be placed there. The holder itself is also easy to replace, as the center joint has an interface with either two M4 or one M6 thread. Since there is a height difference in the center of the beam path when using SPR branches of different sizes, each of the three mounting points can be adjusted in height. The powerful light source with a full width at half maximum of about 2 nm and a center wavelength of 730 nm illuminates the SPR sensor chip with a top hat-like profile. The columns, which are perpendicular to the angular plane, provide homogeneous measurement conditions. Due to the residual divergence that always remains with a surface light source, the angle of incidence spreads out slightly in the plane of the SPR angle. The angle varies by about 4 degrees across the width of the SPR chip, depending on the light source setting. This inherent angular spread can be exploited in a number of ways. One application is a permanent "quasi-angular scan". Here, a line of the receptor is applied along the axis where the angle varies. If the measurement angle is set so that the minimum of the SPR curve is visible on the SPR prism, the movement of the minimum can be followed with the lateral resolution of the camera and lens. If the steep flank of the SPR curve is placed on the SPR prism, a measurement can be made in the first step and then the most sensitive area of the curve can be selected in the second step. Another possibility is to place several receptors with different refractive indices. This is done by placing different receptors in different columns that are perpendicular to the SPR angle plane. If the receptors have different refractive indices, only one of the receptors could be placed at the optimum with a perfectly collimated light source. Thanks to the angular spread, several different receptors can now be optimally placed. The relatively expensive reference measuring station is therefore primarily suitable for the development of new technologies in the field of SPR or for measurements where the highest precision is required.

The laboratory demonstrator has the same basic functionality as the reference instrument. However, a much cheaper and more compact camera has been installed. This reduces the intensity resolution by a factor of about 4. This is acceptable since the instrument still provides a very high resolution in the 10^{-6} range, which is sufficient for the vast majority of applications. In intensity-based SPR, the viewing angle adjustment is only necessary to select the most appropriate measurement angle. A low repeatability error as in the reference station is therefore not required for this type of measurement. To reduce costs, a less expensive linear stage has been developed. Depending on the duration of the measurement, it is also possible to avoid temperature stabilization of the light source and measurement cell, e.g., for very short measurements. This leads to a further cost reduction without affecting the suitability for e.g., binding constant measurements. The strength of the laboratory demonstrator is its significantly reduced price with the same functionality and only slightly reduced resolution. Compared to the reference instrument, this instrument is built on a custom-made aluminum plate. It is much smaller and lighter than the solid optical bench and can therefore be easily transported. In addition, the plate does not contain the standard 25 mm pitch grid, but rather circularly arranged threads that allow the angle range of the SPR to be adjusted more easily and accurately.

The miniaturized SPR sensor is a much smaller and less expensive instrument than the two laboratory instruments. It is not designed to detect constantly changing matrices, so the measurement angle cannot be changed by the hardware. It is designed to measure in a specific application over an extended period of time. An example of this would be monitoring the operating condition of a transformer. By eliminating the linear stage in the sensor version of the SPR tool, a significant reduction in the size of the setup has already been achieved. A further reduction in size by simply removing functions was no longer possible. Consequently, a completely new concept for the miniaturized sensor was required. By eliminating the need for any discrete imaging optics, a much more compact, less expensive and easier to manufacture sensor setup is now possible. The divergence of the light source is controlled by its distance from the prism. In order not to increase the required space, the beam path of the light source was folded. The homogeneity of the light source section is now determined by the radiation characteristics of the LED. Thanks to the high power of the LED, an emitter with a wider or smaller cone can be selected, resulting in a relatively homogeneous illumination in the center. In contrast to previous versions, the camera is used without a lens and without a housing. This allowed the CMOS sensor to be placed directly on the SPR prism. The extreme proximity of the CMOS sensor to the SPR sensitive surface allows imaging without optics despite the slightly divergent illumination. In this way, any discrete imaging optics could be avoided. The comparative measurements show that the sensitivity, of the miniaturized sensor is in a similar range to the laboratory instrument. The disadvantages of this device are its poor reconfigurability. The advantages are the extremely compact and low-cost design.

Table 7.3: A comparison of the application characteristics of the developed devices.

	Reference System	Laboratory SPR Device	Miniaturized SPR Sensor
Temperature stabilization	++	+	0
flexibility	++	++	0
sensor area	++	++	0
RIU resolution	++	+	+
Curve precision	++	0	N/A
price	0	+	++
size	0	+	++
mobility	0	+	++
stabilization with references	++	++	++
Image / ROI post processing	++	++	++

Table 7.3 provides an overview of the application properties of the three device classes developed. From the table, it is evident that the reference system is more appropriate for laboratory use, preferably for very demanding applications. The laboratory device, as suggested by the name, is mainly designed for laboratory use but can also be transported. Due to the significantly reduced costs, multiple devices can be purchased in parallel for routine measurements. The miniaturized sensor, with its compact size and enclosed housing, is ideal for mobile application. When equipped with the references presented here, it should also be well suited as a permanently installed long-term sensor.

7.8 References

[1] Yesudasu, V., Pradhan, H. S., & Pandya, R. J. (2021). Recent progress in surface plasmon resonance based sensors: A comprehensive review. Heliyon, 7(3).

[2] Nguyen, H. H., Park, J., Kang, S., & Kim, M. (2015). Surface plasmon resonance: a versatile technique for biosensor applications. Sensors, 15(5), 10481-10510.

[3] Moran, K. L. M., Lemass, D., & O'Kennedy, R. (2018). Surface Plasmon resonance–based immunoassays: approaches, performance, and applications. In Handbook of Immunoassay Technologies (pp. 129-156). Academic Press.

[4] Capelli, D., Scognamiglio, V., & Montanari, R. (2023). Surface plasmon resonance technology: Recent advances, applications and experimental cases. TrAC Trends in Analytical Chemistry, 117079.

[5] Steinegger, A., Wolfbeis, O. S., & Borisov, S. M. (2020). Optical sensing and imaging of pH values: Spectroscopies, materials, and applications. Chemical reviews, 120(22), 12357-12489.

[6] Zekriti, M. (2019). Temperature effects on the resolution of surface-plasmon-resonance-based sensor. Plasmonics, 14(3), 763-768.

[7] Bolognesi, M., Prosa, M., Toerker, M., Lopez Sanchez, L., Wieczorek, M., Giacomelli, C., ... & Toffanin, S. (2023). A Fully Integrated Miniaturized Optical Biosensor for Fast and Multiplexing Plasmonic Detection of High-and Low-Molecular-Weight Analytes. Advanced Materials, 2208719.

[8] Jobst, S., Recum, P., Écija-Arenas, Á., Moser, E., Bierl, R., & Hirsch, T. (2023). Semi-Selective Array for the Classification of Purines with Surface Plasmon Resonance Imaging and Deep Learning Data Analysis. ACS sensors.

[9] Silin, V., Weetall, H., & Vanderah, D. J. (1997). SPR studies of the nonspecific adsorption kinetics of human IgG and BSA on gold surfaces modified by self-assembled monolayers (SAMs). Journal of colloid and interface science, 185(1), 94-103.

[10] Homola, J. (2008). Surface plasmon resonance sensors for detection of chemical and biological species. Chemical reviews, 108(2), 462-493.

[11] Zybin, A., Shpacovitch, V., Skolnik, J., & Hergenröder, R. (2017). Optimal conditions for SPR-imaging of nano-objects. Sensors and Actuators B: Chemical, 239, 338-342.

8. Conclusion and Outlook

Sensors serve as the senses for digital systems, enabling the translation of the physical world into numerical data for detailed measurements. With the continued advancements in digitalization and automation, the accuracy of sensor technology is increasingly vital in capturing the world around us. Since all materials possess a refractive index, measuring this index is an ideal method for precisely quantifying the physical world. Surface plasmon resonance spectroscopy is a highly precise method for measuring the refractive index of substances, making it an ideal choice for this task. However, SPR technology has faced several challenges that have prevented it from being used for environmental sensing. SPR measurement devices in more compact designs were hindered by their large size, high cost, susceptibility to environmental disturbances, and low resolution. This research demonstrates the feasibility of downsizing SPR sensors, increasing their resilience to environmental interference, and producing them economically.

The refractive index of water and many other materials depends heavily on temperature. Consequently, SPR laboratory instruments have traditionally required costly and complex tempering techniques. Chapter 5 demonstrates how reference structures can be used to avoid the need for high precision temperature control. Additionally, Chapter 2 illustrates the advantages of selecting specific measuring regions using an imaging process instead of measuring a sum parameter across a partially unknown area.

When utilizing certain Regions of Interest (ROIs) and referencing techniques that are directly integrated into the sensor element, the ideal approach is to employ SPR imaging instead of the single or multichannel SPR technology which has been commonly utilized thus far. This is due to the fact that it enables measurement as well as referencing structures to be operated in close proximity and under identical conditions.

In order to accomplish high-resolution SPR imaging, it is essential to uniformly illuminate the surface. The homogeneous light source developed here is a key technology for the miniaturization of intensity-based SPR imaging sensors. The absence of this technology has severely hindered the advancement of high resolution and large area SPR imaging. The benefits of the new light source are clearly demonstrated through a direct comparison with an expanded laser.

This work is a significant contribution to SPR imaging advancement. The advances achieved in this research facilitate reflectivity-based SPR-Imaging laboratory systems to improve their resolution to the 10^{-7} RIU range. Furthermore, high-resolution SPR imaging within the 10^{-6} RIU range has been made possible for miniaturized sensors, and the size of SPR sensors has been significantly reduced.

8.1 Stabilization

Signal stabilization is a key aspect of intelligent sensor systems. The presented technologies can counterbalance interference that affect the SPR measurement signal. Nevertheless, their appropriateness might be limited based on the type of application. The polymer-based reference materials may be susceptible to change against certain analytes, and the encapsulation takes up space. Sometimes it is not always feasible to use mirrors on the sensing surface to distinguish between temperature changes and fluctuations in light source. This means that the demonstrated strategies might not be appropriate under certain circumstances. In order to maintain a stable signal, a stabilization technique through excitation wavelength shifting should be investigated for future sensor applications.

As previously demonstrated in Figure 2.11, the SPR effect is dependent on wavelength. Thus, one may incorporate wavelength as a parameter in designing the system. The range between 600 nm and 1100 nm displays a steep reflectivity gradient, while 395 nm demonstrates minimal change in the same setup (Figure 8.1). This characteristic can be utilized for referencing purposes. The reflection at 395 nanometers should not experience any significant intensity changes if the analyte's refractive index alters. While a modification in either the detector or light path will cause a significant alteration in the reflection of the 395nm light. Using this method as a referencing strategy eliminates the need for additional components, such as a second detector, beam splitter, or polarization rotator. One drawback is the requiring of an additional light source without the ability to observe the sensing light source without extra equipment. Alternatively, variable filters or a hyperspectral camera could be employed if a white light source is utilized.

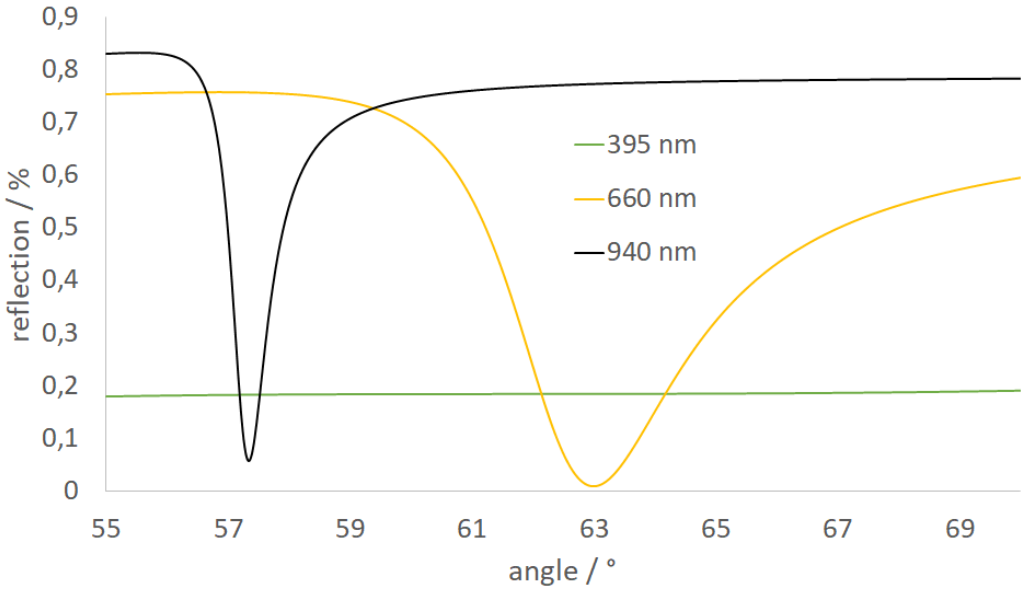

Figure 8.1: Wavelength Based Signal Stabilization, a wavelength that does not exhibit a SPR effect within the utilized angle range is used as a reference. Simulation was done with WinSpall, the prism material is Schott F2, the thickness of Cr is one nm, the thickness of Gold is 50 nm, and the analyte is water. The wavelengths were chosen according to the available LED wavelength.

Due to its broad wavelength spectrum, this technology needs very well concerted components. A setup in which wavelengths from UV to NIR are guided over one and the same light path will most likely lead to problems in a frequently modified system. It will also drastically reduce the number of standard components available. Hence, it is predestinated to be used in high-integrated MOEMS sensors.

8.2 Miniaturization

The miniaturization of SPRi devices is of great importance for improving system durability and reducing costs. When a small sensor is used, its integration into an existing system becomes simpler. This research achieved remarkable progress by eliminating temperature conditioning and the objective lens, significantly reducing the build volume and cutting costs. Further development is needed to integrate individual components into a single device. Reducing the number of components leads to lower volume and cost. This section offers suggestions on how to move in this direction.

8.2.1 Gradient Index Optics Based Monolithic SPR Sensor Device

Regardless of the type of light source utilized, such as LED, LASER diode, SLED, or VCSEL, optics must be added to collimate and shape the light beam. The presence of free space between the components is necessary. Common lenses are typically made of high refractive index materials such as glass. The shaping of the beam relies on both surface contour and the refractive index difference between the lens and the surrounding environment. It is necessary to have an air gap between the light source, the lens, and the SPR sensing element, which makes the system vulnerable to environmental disturbances such as dirt or vibration. To address these issues, it is important to directly bond the light source, beam shaping element, SPR sensing element, and 2D sensor. As previously stated, using a well-collimated light source enables the use of a CMOS chip without an objective lens. To eliminate the remaining air gap, the aspheric lens that was utilized for collimating the light source could be substituted with a gradient index optic (GRIN). This will allow for direct bonding of the LED to the beam shaping optic, as well as direct bonding to the SPR sensing element. Until recently, the availability of GRIN optics has been limited, with small sizes for standard optics. However, a new 3D-printing technology for GRIN optics has become available [1]. Nanoscribe enables a direct laser writing technology for GRIN optics, which introduces a new level of design and use for these kind of optical elements. A possible GRIN setup is illustrated in Figure 8.2.

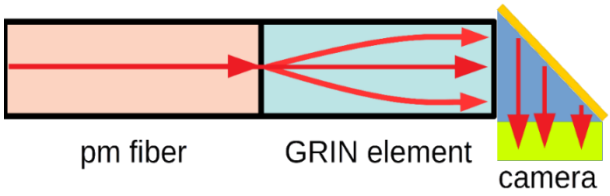

Figure 8.2: A SPR sensor setup with fiber based light source and a GRIN based beam-shaping element. The light source (e.g. a LED or a Laser) is coupled to a polarization maintaining fiber (pm) which is adhered to a beam-shaping element, which contains a GRIN lens. The beam-shaping element is adhered to the prism, which is adhered to the camera chip. The setup exhibits no air gaps and is therefore resistant to dust and vibrations.

Replacing the discrete optical elements of the light source could represent the following stage towards achieving a completely integrated MOEMS sensor. This procedure significantly minimizes the size and fortifies the device against disturbing environmental impacts.

8.2.2 Mirror Based Monolithic SPR Sensor Device

As previously discussed, eliminating the air gap between components can enhance system resilience. One potential solution involves implementing mirrors. Unlike traditional mirrors in which light approaches the metal surface from air, here the light passes through the glass body upon which the mirror is deposited. This approach allows for complete routing of light through the glass body. The creation of a monolithic SPR sensor prototype can be achieved through traditional milling or 3D printing options, which are offered by companies such as Femtoprint. In Figure 8.3, a design sketch of such a monolithic SPR sensor is presented. The beam is expanded by a lens at the entrance surface and subsequently collimated by a mirror, which directs the beam towards the SPR sensing surface. The reflected light is then directed to the camera. To eliminate potential sources of error, the light source and camera can be fused to the optical block.

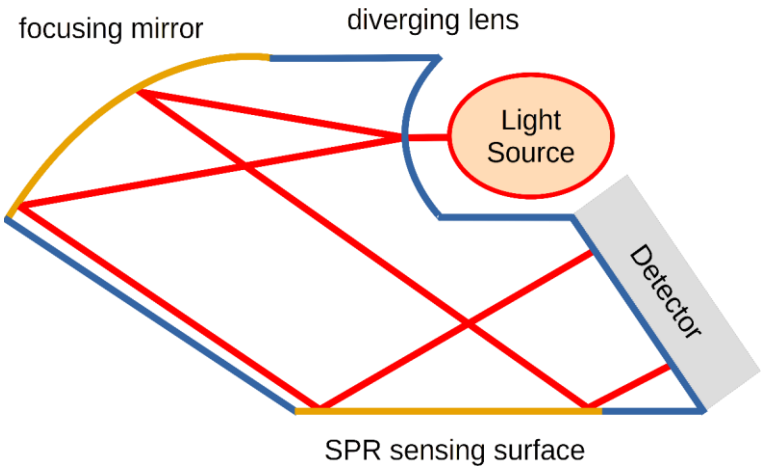

Figure 8.3: A possible design for a monolithic SPR sensor. The beam from a collimated light source is expanded by the entrance lens. It is collimated again at an internal mirror and directed onto the SPR-active surface. From there, the beam is reflected directly onto a camera. It is only one of many possible options for fully integrated SPR sensors.

8.3 Enhanced Technologies

8.3.1 Depth Scanning / 3D Scanning

If a SPR sensor is equipped to work with different wavelengths, it becomes possible to conduct depth scanning. This method allows differentiation between a refractive index change that occurs in the bulk material and one that occurs at the surface of the SPR sensor. If the SPR effect is recorded sequentially for several wavelengths, the changes occurring there can be related to each other. The ratio of change between a 600 nm and a 1064 nm record will differ for surface-only changes versus changes throughout the whole sensing volume. This enables a deep scan to discriminate various states. Figure 8.4 illustrates the depth scanning process and the interaction of different wavelengths with surface attachments. If a small molecule docks on the surface, it may occupy most of the sensitive field for a short wavelength. In contrast, for a long wavelength, this molecule may only occupy a minor portion of the sensitive field. As a result, the relative change induced by this molecule for the corresponding wavelengths will differ.

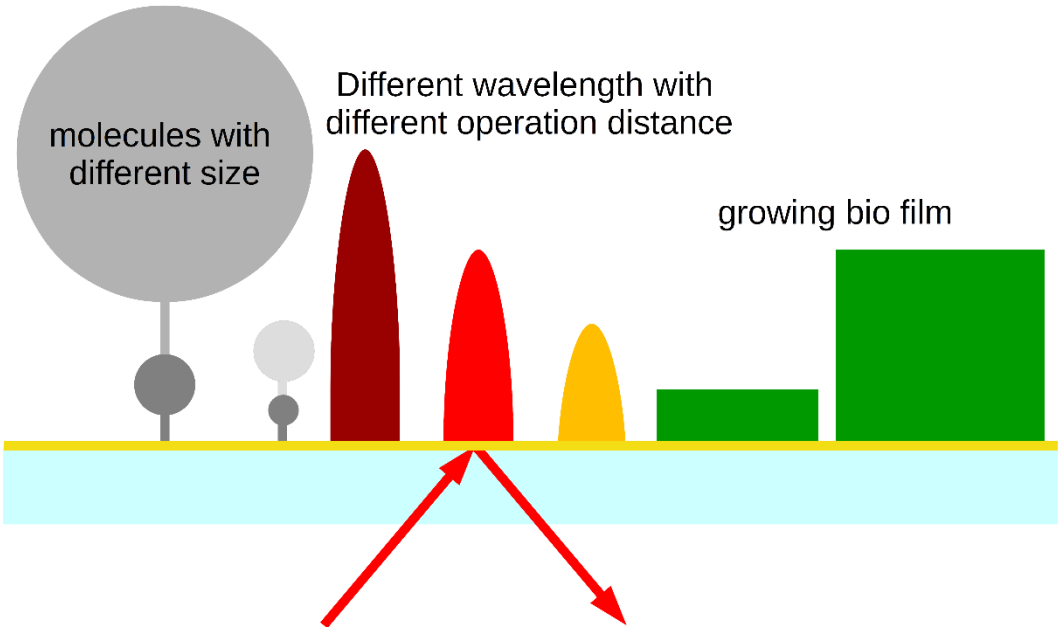

Figure 8.4: Depth scanning SPR. The drawing is not true to scale, it is illustrating how the different operation distances of the different wavelength can be utilized to do a deep scan. If a biofilm starts to growth, the relative change at shorter wavelength (orange) will be higher than at longer wavelength (deep red). If the biofilm gets larger, it will exceed the measuring range of the short wavelength, while there is still a change at longer wavelength. A similar effect is expected to occur for small and large molecules.

Various potential applications exist for this technique. A laminar flow passing over the sensing area can result in a slower exchange of the matrix near the surface, which can be detected through deep scanning. Additionally, the deep scan may detect any growth or accumulation occurring at the sensing surface. If an "amorphous" receptor that permits slow analyte diffusion is present, the 3D scan can capture the analyte's diffusion into the receptor. For instance, silicone facilitates the diffusion of multiple oils. Therefore, if there is a modification in the oil's composition, one can observe a gradual variation in the gradient on silicone-covered surfaces.

In addition to detecting undesired growth or fouling on a sensor surface, SPRI can also detect intended growth on a surface. It's often challenging to measure the growth of biological samples without removing their nutrient fluid when they're cultured in a petri dish. However, removing the fluid can disrupt or halt their growth. Depth scanning SPR provides a solution to this problem because growth can be monitored in real-time and inline on the top of the SPRi sensor.

8.3.2 Remote SPR with 0° Angle

SPR typically operates within a range of 45 to 80 degrees due to the possibility of collision between the light path and instrumentation at angles less than 45 degrees. Additionally, distortion becomes increasingly pronounced above 80 degrees. Ideally, the entrance and exit surfaces of the light beam should be perpendicular to its direction. However, for SPRi, this is only achievable at angles as low as 45 degrees. Otherwise, the light cannot exit the prism through the exit face, or the sensing area shrinks significantly, an effective solution to this problem would be utilizing 0° SPR or SPRi. To enable the technology, a very high refractive index of the carrier material for the gold layer is required. For instance, TeO2 offers a refractive index of 2.26 at 630 nm. This exceptionally high refractive index would enable a steep flank of the water (n=1.33) SPR curve at a 0° angle of incidence. Figure 8.5 illustrates the operational principle of a 0° SPRi setup.

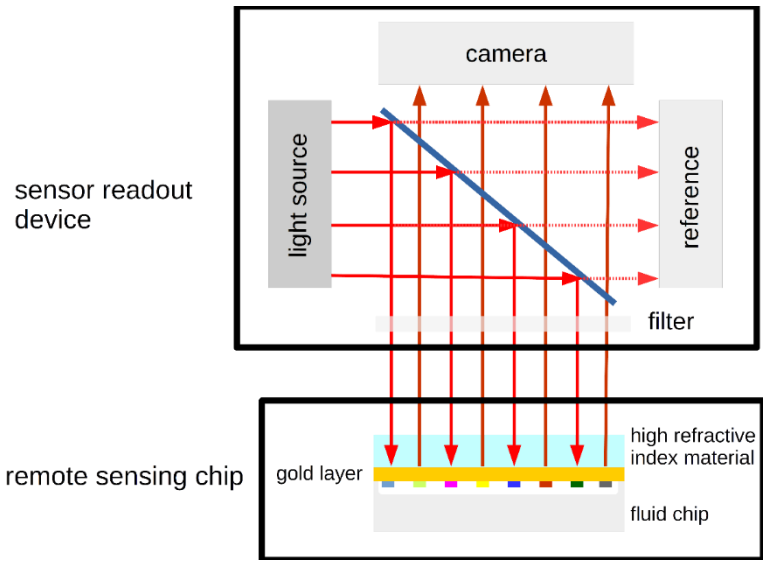

Figure 8.5: Remote SPR; the remote SPRi system consist of two parts, a readout device, and a sensing chip. The sensing chip can be placed at any environment that is optically accessible. It can be operated with a microfluidic chip, as it is depicted or simply placed at a volume, which should be monitored. The readout device consists of a light source, which is routed over a beam splitter to the sensing chip. After passing the beam splitter, the light is filtered by a wavelength filter. At the leaving direction, the filter is acting as a wavelength stabilization element. Furthermore, the beam splitter is transmitting a certain part of the light, which is utilized for referencing the light source. After the SPR chip is reflecting the light, it is passing the filter again. At the entering direction of the light, the filter is acting as an environmental noise blocker. The environmental intensity of deep red and NIR spectra is usually low, which implies that there is a very high ratio between the measurement signal and the remaining environmental light.

The light beam is projected onto the gold-coated plate through a beam splitter and a filter. The resulting reflection from the gold layer partly passes through the beam splitter and enters the SPRi camera. The filter, which all incoming and outgoing light must pass through, stabilizes the output wavelength, and filters out ambient noise at the input. A portion of the light which is emitted from

the light source is passing through the beam splitter. There a detector for monitoring the light source can be installed. The 0° SPRi has an advantage in that there will be no distortion of the image, which increases the lateral resolution in one direction. A general benefit of 0° SPR is that the light source, beam splitter, and camera can be far from the sensing element, enabling remote sensing.

It also enables the SPR sensing element to be placed in a sealed space, such as a flask or petri dish, and thereby sense without disrupting the surroundings. When analyzing biological samples, removing the sample from its optimal environment to analyze it in a measuring instrument can often have significant consequences for the sample. However, with 0°SPR, it might be possible to place the SPR sensor chip directly in the growth vessel and thus analyze the sample in its "natural environment".

8.4 References

[1] Ocier, C.R., Richards, C.A., Bacon-Brown, D.A. et al. 2020 *Direct laser writing of volumetric gradient index lenses and waveguides*. Light Sci Appl 9, 196.

[redacted]

[redacted]

[redacted]

[redacted]

[redacted]

[redacted]

[redacted]

[redacted]

[redacted]

[redacted]

Eidesstattliche Erklärung

Ich erkläre hiermit an Eides statt, dass ich die vorliegende Arbeit ohne unzulässige Hilfe Dritter und ohne Benutzung anderer als der angegebenen Hilfsmittel angefertigt habe; die aus anderen Quellen direkt oder indirekt übernommenen Daten und Konzepte sind unter Angabe des Literaturzitats gekennzeichnet.

Weitere Personen waren an der inhaltlich-materiellen Herstellung der vorliegenden Arbeit nicht beteiligt. Insbesondere habe ich hierfür nicht die entgeltliche Hilfe eines Promotionsberaters oder anderer Personen in Anspruch genommen. Niemand hat von mir weder unmittelbar noch mittelbar geldwerte Leistungen für Arbeiten erhalten, die im Zusammenhang mit dem Inhalt der vorgelegten Dissertation stehen.

Die Arbeit wurde bisher weder im In- noch im Ausland in gleicher oder ähnlicher Form einer anderen Prüfungsbehörde vorgelegt.

Ort, Datum Unterschrift